

# Interannual Variability in Antarctic Sea Ice Motion

Interannuelle Variabilität antarktischer Meereis-Drift

Zur Erlangung des akademischen Grades eines  
DOKTORS DER NATURWISSENSCHAFTEN  
von der Fakultät für Physik der  
Universität Karlsruhe (TH)  
genehmigte

DISSERTATION

von

Dipl. Met. Carolin Schmitt  
aus  
Baden-Baden

Tag der mündlichen Prüfung:

16. Dezember 2005

Referent:

Prof. Dr. C. Kottmeier

Korreferentin:

Prof. Dr. S. Jones



# Zusammenfassung

Das Meereis der antarktischen Ozeane spielt für das Klima der Polargebiete eine entscheidende Rolle und beeinflusst die Kopplung zwischen Atmosphäre und Ozean. Dichte Eisbedeckung verringert den Wärmeaustausch zwischen den oberen Ozean- und den bodennahen Atmosphärenschichten. Die auf das Meereis ausgeübten Schubspannungen durch den Wind und durch Ozeanströmungen sowie die internen Spannungen innerhalb und am Rand der Eisschollen beeinflussen die Meereisbewegung. Dies führt unter anderem zur Bildung von offenen Wasserflächen, wo im Winter Eisbildung stattfindet und in den Sommermonaten Schmelzprozesse initiiert werden. Der beim Gefrieren stattfindende Salzausstoß in den Ozean verändert die Dichte und Temperatur des Wassers an der Meeresoberfläche, so dass Änderungen in der Meereisbedeckung auch die thermohaline Zirkulation im Ozean beeinflussen können. Selbst globale Klimaänderungen sind mit den Polargebieten gekoppelt. Zwischen der Eisausdehnung in der Arktis und dem globalen Klima wurde im letzten Bericht des International Panel for Climatic Change (IPCC, Climate Change 2001) ein enger Zusammenhang dokumentiert.

Innerhalb dieser Arbeit wird untersucht, inwieweit Variabilitäten auf verschiedenen Zeitskalen auch im Meereis der Antarktis, insbesondere in der Eisdrift, vorhanden sind und mit Variationen in der allgemeinen Zirkulation der Südhemisphäre einhergehen. Insbesondere die Weiterentwicklung von Satellitentechnologien und Fernerkundungsmethoden in den letzten Jahrzehnten brachte große Fortschritte bei Messungen in entlegenen Gebieten wie der Antarktis. Zur Untersuchung der Eisbewegung stehen Daten zweier komplementärer Messprinzipien zur Verfügung. Eisdriftvektoren aus identifizierbaren Verlagerungen in aufeinanderfolgenden Satellitenbildern bieten eine homogene Abdeckung des Untersuchungsgebietes und eine zeitliche Auflösung von einem bis zu mehreren Tagen. In-situ Messungen von Bojen erlauben zeitlich und räumlich höher aufgelöste Driftdaten, sind aber lokal eingeschränkt. Um einen optimalen Nutzen aus beiden Datensätzen zu ziehen, wurde eine aufwendige Validierung von Satellitenmessungen anhand von Bojendaten durchgeführt. Es wurde gezeigt, dass die Satellitendaten die Eisdrift

im Mittel leicht unterschätzen. Eine Ausnahme bilden dabei die küstennahen Meereisgebiete, wo die bojengemessene Drift überschätzt wird. Zur Untersuchung von langjährigen Trends und Schwankungen wurden neben der Meereisdrift auch die Eisbedeckung untersucht. Desweiteren wurden atmosphärische Parameter wie Luftdruck, Temperatur und der bodennahe Windvektor in die Untersuchungen mit eingebunden. Bisherige Arbeiten ergaben, dass die Eiskonzentration und -ausdehnung in der Antarktis im Gegensatz zur Arktis keinen ausgeprägten Trend zeigen. Die Analyse langjähriger Zeitreihen der Eisgeschwindigkeit und ihrer Varianz in dieser Arbeit dokumentieren allerdings ausgeprägte regionale Schwankungen und in einigen Gebieten auch starke Abnahmen, insbesondere im Bereich des Weddellmeeres und der Ostantarktis. Methodische Einflüsse von unterschiedlichen Satelliten und Sensoren können dabei weitgehend ausgeschlossen werden. Die negativen Trends sind auch in den Driftmessungen der Bojen dokumentiert. Diese Verlangsamung der Eisbewegung steht in Übereinstimmung mit den Grundmustern der atmosphärischen Zirkulation, insbesondere mit dem positiven Trend des sogenannten "Southern Annular Mode" in den letzten Jahrzehnten. Auf kleinerer Zeitskala sind die mehrjährigen Schwankungen durch den Eigenmode der "Southern Oscillations" auch im Verhalten der Meereisdrift und weiterer kinematischer Parameter wiederzufinden. Dies wird besonders in den gegensätzlichen Ausprägungen von Anomalien im pazifischen Sektor und östlich der Antarktischen Halbinsel deutlich. Desweiteren ergibt sich, dass für Anomalien in atmosphärischen Parametern und Meereisausdehnung, die mit der ostwärts wandernden Antarktischen Zirkumpolarwelle verbunden sind, auch eine Kopplung mit der Eisdrift und ihrer Varianz im Inneren des Packeises nachweisbar ist. Die jahreszeitliche Umverteilung der Masse in der Atmosphäre, die sich in der „Southern Semiannual Oscillation“ widerspiegelt, zeigt sich mit unterschiedlicher regionaler Ausprägung auch im Geschwindigkeitsfeld des Meereises. Dies ist auf die enge Beziehung zwischen Druckverteilung und Windfeld sowie durch den vom Wind an das Eis übertragenen Impuls zu erklären. Die dynamischen und thermodynamischen Beiträge zur Verlagerung des Eisrandes im Laufe des Jahres können unter Nutzung der Eisdriftdaten konsistent erklärt werden.

# Contents

<b>1</b>	<b>Introduction and Objectives</b>	<b>1</b>
<b>2</b>	<b>Sea Ice</b>	<b>5</b>
2.1	Sea Ice Dynamics . . . . .	11
2.2	Preferred Modes of Interannual Sea Ice Variability . . . . .	16
2.2.1	Trends and Oscillation Modes . . . . .	16
2.2.2	Southern Annular Mode SAM . . . . .	20
2.2.3	Southern Oscillation Index SOI . . . . .	20
2.2.4	Antarctic Circumpolar Wave ACW . . . . .	21
<b>3</b>	<b>Data Base</b>	<b>23</b>
3.1	Satellite Data . . . . .	23
3.2	Data from Drifting Buoys . . . . .	26
3.3	Meteorological Data . . . . .	28
3.4	Data Preparation . . . . .	29
3.4.1	Statistical Parameters and Covariance Ellipses . . . . .	29
3.4.2	Interpolation of Gridded Fields . . . . .	30
3.4.3	Differential Kinematic Parameters . . . . .	33
<b>4</b>	<b>Validation of Satellite Ice Drift</b>	<b>38</b>
4.1	Comparison Schemes . . . . .	38
4.1.1	Interpolation and Error Calculation . . . . .	40
4.1.2	Comparison Results for Weddell Zones . . . . .	41
4.2	Examination for all Antarctic Regions . . . . .	47
4.2.1	Comparison Results 1985 - 1997 . . . . .	49
4.2.2	Regional Differences . . . . .	50
4.2.3	Detailed Analysis of High Error Cases . . . . .	52
4.3	Conclusions regarding Validation . . . . .	56
<b>5</b>	<b>Trends in Sea Ice Motion</b>	<b>58</b>
5.1	Investigation Areas . . . . .	58
5.2	Mean Trends in Ice Motion and Variance . . . . .	60

5.2.1	Statistical Equations . . . . .	60
5.2.2	Ice Motion Velocity . . . . .	62
5.2.3	Ice Motion Variance . . . . .	68
5.3	Decreasing Variance in OI Data . . . . .	72
5.3.1	Influence of Buoy Data on the OI Algorithm . . . . .	72
5.3.2	Influence of Differences in 37 GHz and 85 GHz Channel Data . . . . .	72
5.3.3	Influence of different Satellite Sensors . . . . .	75
5.4	Trends from Buoy Data . . . . .	79
5.5	Conclusions from Trend Analysis . . . . .	83
<b>6</b>	<b>Modes of Interannual Variability of Sea Ice Motion</b>	<b>87</b>
6.1	Coupled Modes of Variability . . . . .	87
6.2	Decadal Trend of Ice Motion and SAM . . . . .	89
6.3	Interannual Variability . . . . .	96
6.3.1	Relationship between Ice Motion and SOI . . . . .	96
6.3.2	ACW in Ice Motion Data . . . . .	101
6.4	Annual and Semiannual Variability . . . . .	106
6.4.1	The Seasonal Cycle of Ice Motion . . . . .	106
6.4.2	Sea Ice Margin Variations . . . . .	120
<b>7</b>	<b>Summary</b>	<b>132</b>
	<b>References</b>	<b>137</b>
<b>A</b>	<b>Appendix</b>	<b>145</b>
A.1	Calculation of Covariance Ellipses . . . . .	145
A.2	Details for Comparison in 4.2 . . . . .	150
A.3	Error Values for Comparison in 4.2 . . . . .	151
A.4	Timeseries of Drift Components for 5.2.2 . . . . .	152
A.5	List of Abbreviations . . . . .	156

# 1 Introduction and Objectives

The fascinating environment of Antarctica and the Southern Ocean has always been subject of great scientific interest despite its remoteness and the inhospitable situation. After starting first expeditions (Meinardus, 1938) with the goal to learn more about the character and geographic situation of the unknown continent, the importance of meteorological and oceanographic processes in the Antarctic to the global climate system was soon recognised.

The unique role of the Antarctic is not only justified by being the Earth's coldest and driest place with the highest wind speeds, but also by its considerable influence on the atmosphere and the ocean. The ice covered surface reflects large amounts of solar radiation and causes a strongly negative surface radiation budget in that region. Combined geographical and meteorological effects result in an overall negative energy budget of the polar regions. Balancing with the positive heat budget at lower latitudes gives rise to strong atmospheric and oceanic currents. In contrast to the Arctic, the Southern Ocean is open to the Indian Ocean, the Pacific, and the Atlantic and makes zonal transport through all major ocean basins possible.

Polar sea ice plays an important role in the climate system which is, however, not well elucidated due to difficulties in obtaining regular information about the state of the sea ice cover, in particular in the Antarctic. Of all quantities describing the state of an oceanic ice cover, the vector of sea ice motion is of special importance, since it couples the vertical momentum fluxes in the lower atmosphere and in the upper ocean, causes opening and closing of the ice cover, which affects heat exchange, and transports the ice from the areas of freezing to those of melting and, thus, influences the thermohaline structure of the ocean as well as the convection by changing the density of water. Ice covered parts of the ocean with their high albedo change the surface heat balance of these areas due to the high amount of reflected radiation.

The climate system is sensitively coupled to changes of the state of sea ice at high latitudes. The recent IPCC report (Climate Change 2001) emphasises abrupt changes in the Arctic in the last decades. Such changes in polar

regions up to now have mostly been considered in terms of seasonal and interannual fluctuations of the sea ice extent. Rather abrupt changes of the ice extent have also been found west of the Antarctic peninsula (Turner et al., 2003). It is unclear how the observed instability of large ice shelves in the western Weddell Sea is associated with sea ice changes. Physically significant changes of the characteristics of the ice cover on the regional scale, especially in divergent areas and in the marginal ice zones, have been the subject of specific studies (Gordon and Comiso, 1988; Martin et al., 1992), but still contain a lot of uncertainties.

To deal with the manifold aspects of Antarctica's influence in global climate models, it is necessary to understand the ongoing processes and interactions and to have sufficient data that describe the state of atmosphere and ocean.

For a long time, investigations of the Antarctic sea ice zone were reduced to smaller subareas and short periods, restricted to data that were available from field campaigns. During the First Global Experiment of the Global Atmospheric Research Program (GARP) in 1979, meteorological buoys were deployed by parachute drop into the western Weddell Sea for the first time, giving meteorological data every 1 or 2 days (Ackley and Holt, 1984). Antarctic buoys were used more frequently in the years after 1986. They were capable of monitoring atmospheric pressure, air and ice temperatures as well as position data, and they provided some new and detailed information on geostrophic winds and ice motion from the Weddell Sea. Recent wintertime ship operations of the Winter Weddell Gyre Projects 1986 (WWSP86), the Winter Weddell Gyre Studies 1989 and 1992 (WWGS89, WWGS92), the Ice Station Weddell in 1992 (ISW), and the Antarctic Zone Flux Experiment (ANZFLUX) in 1994 were used to launch buoys, which lasted far beyond the ship cruises and covered large regions of the Antarctic sea ice belt. The buoys are frequently arranged in groups of three to seven to allow for the calculation of reliable estimates of geostrophic winds, ice motion, and their spatial derivatives under favourable conditions. Descriptions of the individual buoy programs and related process studies have been published by Allison (1989), Crane and Bull (1990), Kottmeier et al. (1992), Kottmeier and Lüdemann (1996), Vihma and Launiainen (1993), Ackley (1981), Wadhams et al.

---

(1989), Martinson and Wamser (1990), and Kottmeier et al. (2003). Since 1994, the International Programme for Antarctic Buoys (IPAB) has coordinated the acquisition of data with drifting buoys in the Antarctic. The IPAB data base provides the major part of present-day information about Antarctic sea ice motion.

A great progress in learning more about areawide changes in the Antarctic sea ice started with the era of improved remote sensing techniques. With polar orbiting satellites, it is possible now to monitor the daily state of atmosphere and ocean even in the remote areas of the Southern Ocean. Scanning microwave sensors give a detailed impression of the changing extension and concentration of Antarctic sea ice. Moreover, information on sea ice motion can be obtained from pairs of sequential satellite images by different algorithms. The basis is the detection of significant features in the satellite images, which move with the mean drift and appear at different places in the following image. The displacement vector of the single features is calculated with cross correlation methods after moving a search window in a defined region of the target image. Errors are caused mainly by weather effects (cloud cover) and surface change of the tracked feature (ridging, melting).

Today, we can look back on more than two decades of sea ice data from remote sensing and in-situ measurements. This allows for investigations of the immense annual and interannual fluctuations of the sea ice cover and for estimations of longer trends that are correlated with climate variations.

In the following sections, a detailed study of Antarctic sea ice motion and its variability in relation to atmospheric processes shall be presented. For this purpose, information on sea ice drift and its derivatives will be gained from satellite as well as from buoy data. The use of the two datasets based on different measurement principles and with different temporal and spatial resolution will make an extensive comparison necessary. Thus, satellite-derived drift estimates will be validated with buoy data in the first part of this thesis. Detailed studies concerning comparisons of satellite drift data with drifting buoy measurements (Geiger et al., 1998) show that it is not sufficient to just compare simultaneous values at the same position, but also necessary to consider the data from a certain radius around. Therefore, a comparison

scheme will be developed to account for regionally and temporally different influences on tracking accuracy. A quality index for satellite data, adapted to the local situation, will be derived.

In Chapter 5, multi-year timeseries of ice motion and its derivatives shall be investigated to find out if significant changes and trends exist in sea ice motion and whether these results are affected by the fact that the data are obtained from different sensors on changing satellites during the investigation period. These influences have to be excluded to correlate ice motion data with the trends of atmospheric parameters.

The last chapter will include investigations of the relation between variations of sea ice motion and atmospheric variability on interannual timescales. Statistics of sea ice motion, concentration and atmospheric data will be calculated based on the already established knowledge of climate variability on decadal, interannual, and annual scales. Thus, the response of sea ice motion to differences of the forcing parameters and also feedback mechanisms that reinforce or attenuate these fluctuations can be investigated to learn more about the interactions of atmosphere, ice, and ocean.

## 2 Sea Ice

Sea ice covers a large area of the polar ocean, with its extent showing pronounced annual fluctuations. In the Southern Ocean around Antarctica the area varies from  $4 \cdot 10^6 km^2$  in summer, when the remaining sea ice concentrates mainly in the areas of the western Weddell and the Amundsen and Bellingshausen Seas, up to about  $20 \cdot 10^6 km^2$  in austral winter, when the ice cover reaches  $55^\circ S$ . Compared to the Arctic, the Antarctic continent shows a much more zonal pattern which is surrounded by uninterrupted oceans.

The general characteristics of mean winter sea-ice drift are illustrated by the mean ice drift velocity vectors for July 1989 (Fig. 2.1).

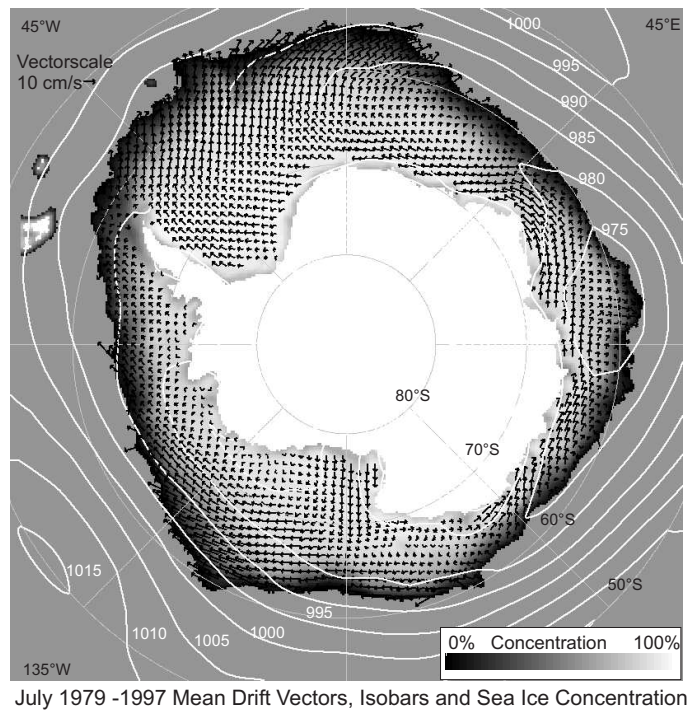


**Figure 2.1:** *Mean July ice motion. The plot represents the sea ice drift vectors superimposed on the PELICON sea-ice concentration field, together with the accompanying NCEP sea-level pressure field.*

A typical ice motion pattern consists of the predominant gyres in the Weddell and Ross Seas, westwards zonal drift along the Antarctic coast, and stronger eastward motion of the ice in the northern areas that are influenced by the Antarctic Circumpolar Current (ACC). A distinctive convergence zone occurs along the central axis of the Ross Sea ( $190^{\circ}\text{E}$ ,  $75^{\circ}\text{S}$ ), where large fractions of coastal perennial ice from the Amundsen Sea meet newly-formed ice that is forced northwards away from the Ross ice shelf by catabatic winds. Further north, sea ice accelerates, as it escapes the entrapment of the Victoria Land coast to enter the ACC. As a consequence, the westward extent of the Ross Gyre is clearly delineated at around  $170^{\circ}\text{E}$ , where sea ice exiting the Ross Sea turns east and flows towards the Amundsen and Bellingshausen Seas. Not surprisingly, the climatological maximum sea ice extent is observed at the location, where sea ice dynamics constantly reinforce the ice. A similar pattern is encountered in the Weddell Sea, with sea ice accelerating, as it escapes from the grip of the Antarctic peninsula. It turns sharply eastwards upon entering the region of influence of the ACC and forms a broad maximum of sea ice extent, reaching from  $45^{\circ}\text{W}$  to  $20^{\circ}\text{E}$ . Whereas the Ross Gyre exhibits a seasonally variable southward return limb in the Amundsen Sea, the Weddell gyre indicates no equivalent flow. All perennial ice surviving the summer is swept from the basin in the following year.

The sea ice layer itself exerts great impact on both the ocean and the atmosphere. The schematic overview in Fig. 2.2 illustrates the main influence of sea ice cover.

- **Sea Ice as Insulator**

The sea ice cover restricts the exchange of heat, mass, and momentum between the ocean and the atmosphere. Especially in the winter months, when a strong temperature difference between the warmer ocean and the cold atmosphere exists, the heat flux in open leads between the ice sheets grows to a considerable amount. Hence, the ice-water distribution and the opening and closing of leads is an important parameter for the local energy balance.

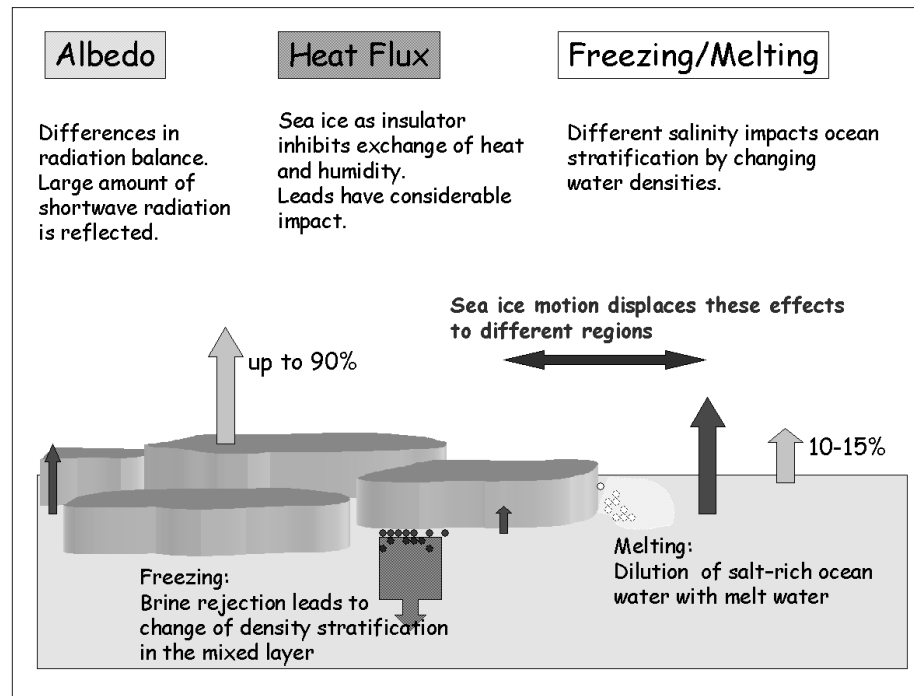


**Figure 2.2:** *Mean effects of sea ice cover and motion.*

- **Albedo**

Depending on its structure and state (e.g. ridged, snow-covered, melting), sea ice has an albedo of up to 90%, which differs from that of open water which is 10-30%. Hence, a large amount of shortwave solar radiation in ice-covered regions is directly reflected into space and not absorbed, which leads to a reduced supply of energy in these areas. On the climatological scale, a positive albedo feedback mechanism leads to a cooling of this area, followed by enhanced ice formation and growing areas of high albedo. In case of warming and ice melting, this effect occurs in the inverse direction.

- **Brine Rejection**

During the freezing process, the salt of the ocean water is not bound in the matrix of the solid. The salt remains highly concentrated, called brine, in small channels in the ice. During ice formation, this brine is rejected, leading to a higher salt concentration and higher water

density below the newly built ice surface. These density differences may cause convection in the mixed layer. The formation of the cold, dense Antarctic Bottom Water in regions of weak density stratification is enforced by this mechanism.

- **Ice Transport**

Driven by wind and ocean currents, sea ice moves far from the regions of its origin. This leads to freshwater and latent heat export to places, where no ice is built. In the melting areas, the upper ocean layers will be diluted with freshwater which stabilises the ocean stratification and prevents convection. Hence, sea ice motion leads to different density distributions in the water masses and, thus, drives the thermohaline circulation of the oceans.

Since the beginning of sea ice investigations, different sea ice types have been classified visually. Until today, optical classification results from ice surveys of ships may be an important aid in the validation of satellite-derived ice classification. A detailed classification scheme is defined by the World Meteorological Organisation WMO (WMO, 1970). Classification is based on structural and optical characteristics that result from the processes the ice is undergoing while growing. The groups range from smallest, flexible ocean cover to thicker, ridged multi-year ice which can reach a thickness of several decameters.

According to its age, sea ice is broadly classified into two groups: the perennial or multi-year ice (MY) and the seasonal or first-year ice (FY). The first-year ice is all sea ice that is newly built within one winter season by freezing. It has an average thickness  $d$  of 0.3 to 1 m and develops from thinner new ice ( $d \leq 30$  cm). Seasonal sea ice which plays an important role in air-sea interaction in the Weddell Sea (a region of large deep-water formation with potential impact on climate) depends critically on the heat flux from the deep ocean. (McPhee et al., 1999).

Sea ice that survives one or more melting seasons is called multi-year ice. Its thickness ranges from 1 m to several decameters and it normally has a rough, ridged surface. Due to its longer lifetime, it is nearly salt-free. This is an important parameter that allows to distinguish between FY and

---

MY ice in remote sensing data, since the salt concentration changes the radiation properties of the ice. In the Antarctic, the main regions with MY ice are the Weddell and eastern Ross Seas and small zones in the Bellingshausen/Amundsen Seas and around east Antarctica.

The sea ice region may also be divided into sections of different dynamic characters (Leppäranta, 2005), (Weeks, 1989). The coastal boundary zone consists of fast ice and shear ice. Fast ice means the immobile part of the sea ice cover that is directly attached to the coast or shelf ice or grounded icebergs. Away from the coast, this area is followed by the shear zone, which is the transition from fast ice to the neighbouring free drift field. This is an area of strong deformation and internal stresses, where ridging is the main sink of kinetic energy into deformation. Within the following central pack, sea ice motion is free and not influenced by any boundary effects. The marginal ice zone (MIZ) to the ocean is associated with the highest ice drift velocities and variabilities. Leppäranta (2005) describes the MIZ as a band of typically 100 km width, within which ocean swell can affect the ice surface.

The sea ice zone, especially the continental and oceanic ice margin areas are of great interest to the atmospheric processes, too. In these areas which consist mainly of first-year ice, strong temperature and structural differences occur between the ice and water surface. Discontinuities of albedo, radiation balance, heat fluxes, and surface roughness cause extreme differential heating and horizontal temperature differences in the atmosphere and, thus, favour these areas for cyclogenesis and polar lows (Rasmussen and Turner, 2003). The zone of most frequent cyclolysis is the Antarctic Circumpolar trough, a dominant feature in atmospheric circulation. It is situated in the convergence zone between the coastal easterlies close to the Antarctic continent and the warmer circumpolar westerlies at lower latitude and comprises several low pressure centres, the climatological positions of which are around the Amundsen Sea, the eastern Weddell, and the areas in the western Pacific around Wilkes Land and the Amery Ice Shelf (Fig. 2.1). The distance from the coast varies with semiannual and interannual frequencies and in response to the signals of ElNino/Southern Oscillations (ENSO), see sec-

tion 2.2.1. Near the coastal boundaries of the ice cover, the development of coastal polynyas is enhanced by the existence of cold catabatic winds which are caused by strong cooling of the near-surface air on the continent and imply strong seaward wind stress and offshore ice motion, mainly in areas with steep coasts.

## 2.1 Sea Ice Dynamics

Ice-covered ocean surfaces are the moving interfaces of wind and ocean forces. First historical data on ice motion come from the involuntary drifts of the ships *Endurance* and *Deutschland*, which got stuck in the pack. Their position reports provide a first overview of ice drift within the Weddell Gyre (Fig.2.3). In contrast to conditions in the Arctic, the basins around Antarctica are all partly open, which allows for an exchange with the neighbouring oceans. Only in the basins of the Ross and Weddell Seas do the boundaries have a barrier effect, whereas the free ocean does not restrict ice dynamics.

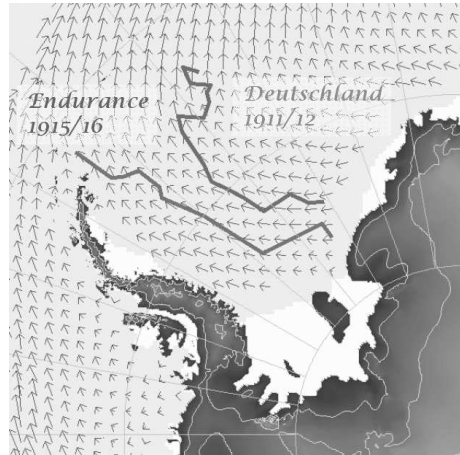


**Figure 2.3:** *Historical drift paths of the ships Endurance and Deutschland, with underlying mean ice motion field obtained from two decades of satellite data (Schmitt et al., 2004).*

Since the ice is located and moves on the ocean surface which can be treated as an equipotential surface, motion is almost 2-dimensional. Apart from the forcing from wind and ocean currents, additional forces affect the ice motion and are considered in the equation of motion.

The basic assumption in Newton's law  $m \frac{d\vec{v}}{dt} = \sum \vec{F} = \vec{F}_i + \vec{F}_e$  relates the vector of sea ice motion  $\vec{v}$  to the internal forces  $F_i$  and external forces  $F_e$ . Following Kottmeier and Sellmann (1996) and Vihma et al. (1996), the equation of momentum balance comprises the external forces from air  $F_a$  and water  $F_w$  stresses, ocean surface tilt  $F_T$  and Coriolis force  $F_C$ . This leads to:

$$m \frac{d\vec{v}}{dt} = \vec{F}_a + \vec{F}_w + \vec{F}_C + \vec{F}_T + \vec{F}_i \quad (2.1)$$

For a complete description of the motion, internal forces cannot be neglected. With force being defined as the divergence of stress, the internal

forces  $F_i$  can be expressed as  $\nabla \cdot \sigma$ . The divergence of the strain rate  $\sigma$  comprises the effects of internal stresses and is elucidated in more detail in Hoeber (1991) and Leppäranta (2005).

Air and water stresses can be parameterised by a linear quadratic law, including the respective densities of air ( $\rho_a$ ) and water ( $\rho_w$ ) and drag coefficients  $c_a$  and  $c_w$  of the medium as well as the relative velocity vectors between ice motion  $\vec{v}$ , surface wind  $\vec{v}_a$ , and ocean current  $\vec{c}$ .

$$\tau_a = \rho_a c_a |\vec{v}_a - \vec{v}|^2 \quad (2.2)$$

$$\tau_w = \rho_w c_w |\vec{c} - \vec{v}|^2 \quad (2.3)$$

Thorndike and Colony (1982) express two-component vectors as complex numbers, including the turning angles  $\alpha$  and  $\beta$  between the surface currents and the geostrophic wind vector  $\vec{v}_g$  and the resulting ice motion vector.

$$\tau_a = \rho_a c_a |\vec{v}_g - \vec{v}| (\vec{v}_g - \vec{v}) e^{i\alpha} \quad (2.4)$$

$$\tau_w = \rho_w c_w |\vec{c} - \vec{v}| (\vec{c} - \vec{v}) e^{i\beta} \quad (2.5)$$

As in Vihma and Launiainen (1993), the notation of the following equations is such that  $\tau_a$  is in the same direction as the surface wind, transferring momentum from the wind on the drifting sea ice floe, while  $\tau_w$  represents the momentum transfer from the moving ice on the ocean or vice versa. From boundary layer theory, it follows that  $c_a$  and  $c_w$  slightly decrease with increasing surface Rossby number, i.e. with sea surface and ice bottom roughness. Hoeber (1991) gives mean values of  $c_a = 0.0013$  and  $c_w = 0.0022$  to  $0.0047$  depending on the season. Stratification is another important parameter, since influences the transfer of momentum between ocean and atmosphere. Stable stratification near the ocean-ice and air-ice boundaries leads to decreasing  $c_a$  and  $c_w$ .

The tilt of the ocean surface is associated with a horizontal pressure gradient force.  $F_T$  is expressed by the mass per unit area  $m$  and the height

$H$  of the ocean.

$$\vec{F}_T = -mg\nabla H \quad (2.6)$$

In the Southern Hemisphere, the Coriolis force  $F_C$  is turned by  $90^\circ$  to the left of the ice motion vector. With the Coriolis parameter  $f = 2\omega\sin(\phi)$ , including the Earth's angular velocity  $\omega$  and the latitude  $\phi$ , the Coriolis force per unit area results as:

$$\vec{F}_C = mf\vec{k} \times \vec{v} \quad (2.7)$$

Including the above definitions, the equation of motion based on the mass per unit  $m$  is written as follows:

$$m\frac{d\vec{v}}{dt} = mf\vec{k} \times \vec{v} + \vec{\tau}_a - \vec{\tau}_w - mg\nabla H + \nabla \cdot \sigma \quad (2.8)$$

Various investigations reveal that the vector of relative sea ice motion is roughly in the direction of the geostrophic wind  $\vec{v}_g$  (Kottmeier and Sellmann, 1996). This is due to the fact that surface winds deviate by about the angle to the right from the geostrophic wind, as the ice drift deviates to the left from the surface wind (Fig. 2.4). Furthermore, the dominant timescale of ice motion variability is the one of wind forcing, which confirms the direct relationship. Commonly, this is to explained by the *free drift assumption*, where no internal stresses exist and wind, water, and Coriolis force balance each other.



For the ice motion  $v$  the complex model relationship reads:

$$\vec{v} = \tilde{A}\vec{v}_g + \tilde{C} + \epsilon \quad (2.9)$$

The complex parameters are marked by a tilde.

$\tilde{A}$  is the multiplier constant that relates the ice motion  $\vec{v}$  to the geostrophic wind  $\vec{v}_g$ . It is expressed as

$$\tilde{A} = |A| \cdot e^{-i\Phi} \quad (2.10)$$

and comprises a scaling factor  $|A|$  which gives the relation of the ice motion speed to the wind speed and a turning angle  $\Phi$  which shows the deflection of the drift vector.

The complex constant  $\tilde{C}$  is that part of the ice motion that is not wind-related. It comprises all constant effects, the mean geostrophic ocean surface current as well as the effects of internal stress and ocean surface tilt.

The factor  $\epsilon$  contains all the residuals, e.g. the drift changes that are neither constant nor linearly related to wind forcing. It includes contributions from nonlinear effects and all time-varying parameters, such as time-dependent currents, but also measurement errors or the like.

Eq. 2.9 can be applied as a complex linear regression equation to the ice drift and wind data from measurements or model estimates. Solutions are obtained by calculation and subtraction of temporal means  $\vec{v} - \bar{\vec{v}}$  of Eq. 2.9, taking into account  $C - \bar{C} = 0$  for the constant effects and  $\bar{\epsilon} = 0$  for the time-dependent ones. The resulting equation is:

$$\vec{v} - \bar{\vec{v}} = \tilde{A}(\vec{v}_g - \bar{\vec{v}}_g) + \epsilon \quad (2.11)$$

By this,  $A$  and  $\Phi$  are determined as regression parameters from timeseries for the geostrophic wind and ice motion velocity via linear regression. For stronger geostrophic winds  $\vec{v}_g$ , the nonlinear effects in  $\epsilon$  can be neglected. Higher values of  $\vec{v}_g$  lead to decreasing angles  $\Phi$ .

Extensive studies of this relationship are performed for example by Kottmeier et al. (1997) for timeseries in the Weddell region. They found

that average values of the ice drift are 0.5 – 1.5% of the geostrophic wind velocity and that about 50 – 80% of the total variance of drift speeds can be explained by the linear model. Other investigations specify the ice velocity to be 2.6% of the wind speed at 10 m height in the inner pack and up to 3.4% around the marginal ice zone. Deflection angles vary about 36° to the left of the wind direction, with higher values during summer and smaller ones in winter times. The wind speed/drift ratio is reduced by ocean currents opposing the winds, by stable stratification in the atmospheric surface layer and by internal stresses.

## 2.2 Preferred Modes of Interannual Sea Ice Variability

The progress in remote sensing techniques helped making a wider range of data on Antarctic sea ice available in the last years. Various studies have focussed on trends and anomalies mainly of sea ice concentration (SIC) and sea ice extent and area for more than two decades. The sea ice extent (SIE) comprises the whole area covered with sea ice and open water up to a minimum concentration value of 15% in most studies. The sea ice area (SIA) means the total area that would be covered by the sea ice cover available, if compressed to 100%. By this definition, SIA always has to be smaller than SIE, especially in wide areas with lower concentration.

### 2.2.1 Trends and Oscillation Modes

The mechanisms behind the dominant modes of variability around Antarctica are essential to understand the coupling of polar and other regions. In this context, sea ice plays an important role. The sea ice extent in the Antarctic was shown to slightly increase during the last two decades in contrast to the Arctic (Cavalieri et al., 1997). Within the *Project for estimation of long-term variability of ice concentration* (PELICON), Heygster et al. (1996) found a positive trend of monthly mean anomalies (Fig. 2.5), representing the differences of one month's mean from the climatological mean of that month for the whole examination period.

In Fig. 2.5, the anomalies of the sea ice area exhibit large interannual vari-

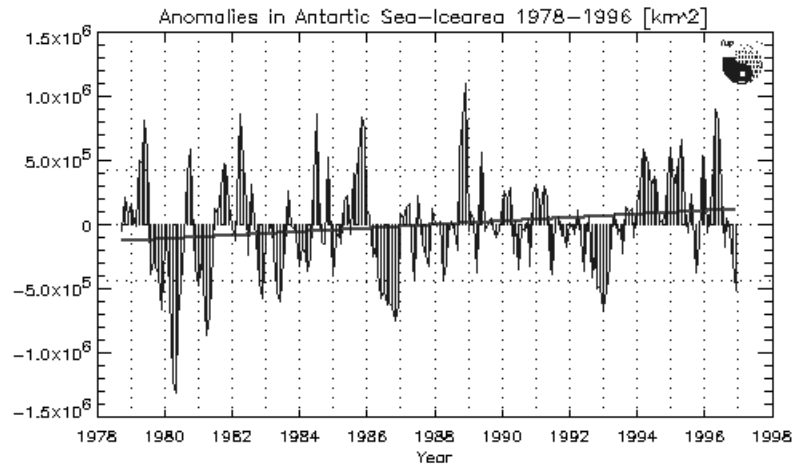


**Figure 2.5:** *Positive trend in Antarctic SIA anomalies, according to Heygster et al. (1996).*

ations, but an evident positive trend. The investigation of Cavalieri et al. (1997) gives a positive trend of sea ice extent of  $14.3 \cdot 10^3 \text{ km}^2/\text{year}$ . Similar values are obtained by Watkins and Simmonds (2000), who compared time-series of SIC, SIE, and SEA for the period 1997-1996. Their investigations differ from earlier ones, where no statistically significant change could be observed. The main reason is that their investigations already included the years after 1994, when the SIE increased strongly with a substantial effect on the longer-term trend. Moreover, these changes are proposed to be caused by modifications of the position and depth of the Antarctic circumpolar trough which was dislocated to the South, as ascertained by Simmonds et al. (2003) and Stammerjohn et al. (2003). This brings stronger zonal winds, the so-called "Westerlies" to the sea ice regions. With the related northward Ekman transport of sea ice it leads to an increase in sea ice extent.

Another parameter to describe the regional and temporal change of sea ice properties is the so-called "length of sea ice season" (SIS), defined as the number of days per year with a sea ice concentration exceeding a threshold value, in most cases 15% again. The length of the sea ice season changes

with the onset of freezing and melting in the different regions. Regional differences are evident from this parameter, too. In an extensive comparison, Parkinson (1998) found that the length of SIS was shortened in the northern areas of the Weddell Sea and the Bellingshausen Sea. An opposite behaviour was found in the central Weddell as well as in the Ross Seas and the coasts of the Indian Ocean.

When observed over a wider area, the trends and anomalies of Antarctic sea ice parameters can be related to the influence of ocean-atmosphere modes of variability. So far, the relations of sea ice variations to these modes have been based mainly on data of sea ice extent anomalies and changes in area. Investigations that include the dynamic contributions from sea ice motion are only sparse.

The dominant modes of variability of atmospheric parameters are reflected by pressure anomalies that can be identified by *Empirical Orthogonal Functions* (EOF) from monthly mean height anomalies of specified pressure levels (e.g. 850 hPa). The resulting EOF modes cover most of the explained variance. A good general overview is given by Thompson and Wallace (2000). The following figure (Fig. 2.6) shows the correlation maps of the first three EOF of extratropical 850 hPa height with the pressure anomalies. The structure of these EOF patterns can be related to the dominant modes of atmospheric variability, as will be discussed below.

EOF1, according to different studies, explains 27-33% of the total variance of the pressure height anomalies, shows a nearly zonal configuration around the continent, and is related to the Southern Annular Mode (SAM). EOF2 explains up to 22% of the variance and shows a typical dipole pattern with positive correlations over the Ross and Amundsen Seas being in antiphase with the negative ones of the other regions, mainly in the Weddell Sea. This is associated with the Southern Oscillation Index (SOI). EOF3 can explain 9% of the variance and represents a wavenumber 3 pattern. It is dominated by the mean synoptic pressure pattern around the Antarctic continent, which is shown in Fig. 2.1. In the following chapter, these modes will be described in more detail.

EOFs 1-3 of SH extratropical 850 hPa Z (plotted as correlations)

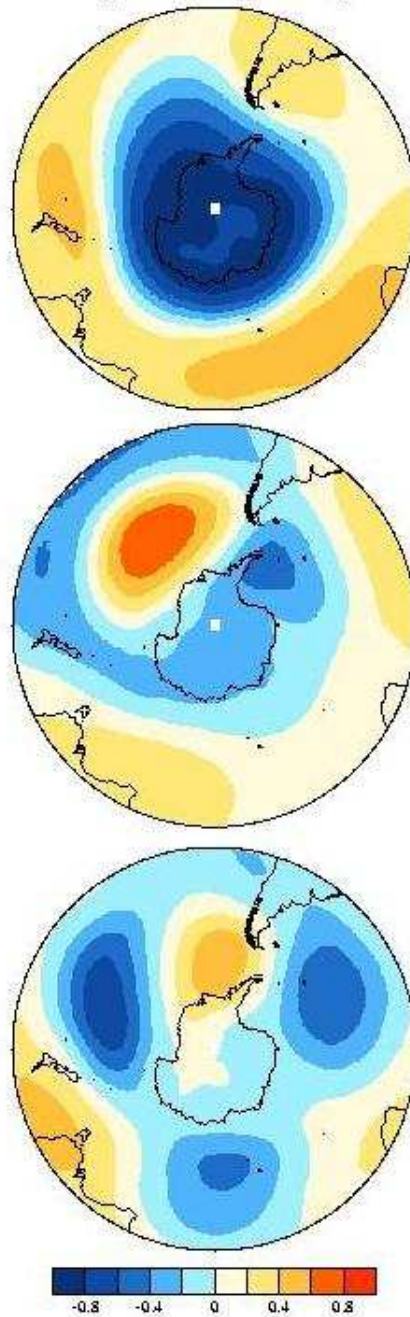


**Figure 2.6:** Correlation maps of EOF 1-3 of the 850 hPa level, from Todd Mitchell, (available at <http://www.jisao.washington.edu/aao>). The fields show positive and negative correlations of the first three EOF of extratropical 850 hPa height with the pressure anomalies.

### 2.2.2 Southern Annular Mode SAM

The Southern Annular Mode SAM is the dominant pattern of tropospheric circulation variations. It originates from pressure anomalies of the air mass south of 60°S and at 45°S. This pressure distribution results in an almost polar symmetric pattern with zonal winds, which is represented by the first EOF of the 850 hPa level height from 20°- 90°S (Fig. 2.6). Strongest negative correlation values are obvious over the Antarctic continent and in the coastal sea ice zones, especially in the Ross and Amundsen Seas and positive ones are obtained for the Indian and Pacific oceans. The fluctuations of SAM do not show any dominant period. In the last years, however, SAM exhibited a strong positive trend which is documented by various investigations (Kwok and Comiso (2002b), Kwok and Comiso (2002a), Zwally et al. (2000)).

A positive SAM leads to stronger negative pressure anomalies over the Antarctic continent. The pressure distribution results in stronger zonal winds, the so-called "Westerlies", in the sea ice zone and a negative anomaly in the meridional wind component in the areas of the Amundsen Sea.

As a consequence of prevailing positive SAM indices, Kwok and Comiso (2002b) found temperature anomalies over the continent with a net cooling of 0.07 K/year and a positive temperature trend at the Antarctic peninsula and the surrounding seas of 0.09 K/year. Due to the already annual pattern, the ice concentration does not reveal any clear response to the leading EOF of sea level pressure.

### 2.2.3 Southern Oscillation Index SOI

The Southern Oscillation Index SOI is defined as the surface pressure differences between the Indian Ocean/Australia and the southeastern tropic Pacific. It can be calculated from measurements of the difference between standard sea level pressures in Tahiti and Darwin. The main changes occur with periods from 3 to 5 years. The large air mass redistribution associated with the SOI also affects Antarctic regions. As a result, ice edge anomalies in Pacific and Atlantic sectors show alternating patterns. Timeseries of the SOI do not show any trend, but a negative bias, superposed by quadrennial variations with main effects in Pacific sector. Strongly negative SOI values occur

in the ElNiño years, as described by Allan et al. (1996). Several Antarctic climate anomalies are correlated with the SOI, with strongest responses in the Bellingshausen, Amundsen, and Ross Seas. A negative SOI is linked to a higher sea level pressure and warmer sea surface temperature. This leads to a warming of the sea ice zones around Antarctica, with mainly positive temperature anomalies and sea ice retreat in the Pacific sector, the Ross and Bellingshausen Seas. Kwok and Comiso (2002a) found a decrease of SIE and SIS in these regions, but no significant trends of SIC for phases of negative SOI.

For the ENSO event in 1987, a record decrease in SIE was detected in the Bellingshausen and Amundsen Seas (Jacobs and Comiso, 1997). This was connected with extremely high surface pressures and strong southerly winds. Parkinson et al. found for the ENSO event of 1992 a shortening of sea ice seasons in the Ross, Amundsen and western Weddell Seas as well as along the coast of East Antarctica. In contrast to this, longer sea ice seasons occur in the western Ross, the Bellingshausen, and the central Weddell Sea.

#### 2.2.4 Antarctic Circumpolar Wave ACW

Further investigations of the quasi-quadrennial anomalies in atmospheric and sea ice data reveal pronounced anomalies that propagate eastwards around Antarctica. The first overview of this Antarctic Circumpolar Wave (ACW) is presented by White and Peterson (1996). They compare anomalies of sea level pressure (SLP), sea surface temperature (SST), mean wind stress (MWS), and sea ice extent (SIE) to find a simultaneous propagation around the continent. For a clearer view of these anomalies, the mean values of the timeseries were removed and the results were bandpass-filtered with an acceptance window of 3 - 7 years to remove trends and seasonal variations. Their results and a later investigation (White et al., 1998) document an eastward propagation of the selected anomalies during the years. The average velocity is around 6-8 cm/s. Thus, it takes 8 to 10 years to circulate around Antarctica. The correlations of SST with SLP show maximum positive correlations for negative temporal lags of around 12 months. This means that positive pressure anomalies precede the positive SST anomalies by about 90° longi-

tude. Investigations were extended to cover relations with other atmospheric parameters (White et al., 2004).

Detailed examinations of the coupling of anomalies in the Ross and Weddell Seas were carried out by Venegas et al. (2001) and Venegas and Drinkwater (2001). They found phase-shifted signals of the ACW in the different basins. In the Ross, Amundsen, and Bellingshausen Seas, atmospheric oscillations with a 3-5 year's period dominate the variability. Propagation of atmospheric anomalies lead to a zonal shift of the low pressure centres and to changes of the ice drift pattern from a closed Ross Gyre to strong equatorward drift patterns with consequent ice margin anomalies. Gloersen and White (2001) as well as Peterson and White (1998) consider the relation of the ACW with the ENSO a possible source for the interannual anomalies to sustain, even in the sea ice with its large annual changes between winter and summer.

Model simulations have shown (White et al., 2004) that the atmosphere-ocean coupling is necessary to explain the persistence of the anomalies. The single process of advection by the ocean results in too small values, while results of coupling with an atmospheric model come closer to reality. The balance between negative heat flux anomaly and meridional heat advection helps the anomalies of the ACW to sustain. A detailed description of these processes can be found in Venegas (2003). They tried to detect the mechanism behind the ACC and the reasons for its variability by revealing a combination of two signals via frequency-domain composition. The investigations show a wavenumber 3 pattern with a 3.3 year's period that consists of oscillation atmospheric anomalies at fixed positions that seem to be oriented by the land-ocean distribution and a propagating pattern in the ocean driven by the ACC. The second one is a wavenumber 2 pattern with a 5 year's period that is forced by the ENSO and, hence, reaches its largest intensities in the eastern Pacific. The variability of the ACW is explained by the interference of the two wave patterns.

---

## 3 Data Base

This chapter introduces the datasets on sea ice motion and atmospheric parameters that are used for the following investigations. To learn more about sea ice motion variability, drift data based on two different measurement principles are applied. Each type of data is characterised by different advantages and restrictions that have to be considered.

Drifting buoy data reach a good temporal resolution and position accuracies from 350 m for ARGOS buoys to about 50 m for GPS buoys. However, all regions and temporal seasons in the Southern Ocean cannot be covered homogeneously.

A better spatial and temporal coverage of ice motion is achieved by data from polar-orbiting satellites, that cross the region of interest several times a day and, hence, provide daily composite images, but of coarse resolution and lower accuracy. Various schemes and algorithms have been developed and tested to determine ice motion from pairs of sequential radar or passive microwave radiometer images (Kwok et al. (1990), Kwok et al. (1998), Maslanik et al. (1998), Liu and Cavalieri (1998)).

This analysis takes advantage of algorithms developed for ice drift using data from passive microwave sensors on polar orbiting satellites as well as of drifting buoy data gathered within various national programs. All data are uniformly georeferenced and combined in a Geographic Information System (GIS). This allows for a spatial and temporal superposition of the different data and makes a combined analysis possible.

### 3.1 Satellite Data

The *Special Sensor Microwave/Imager* SSM/I has been operated on the satellites of the DMSP *Defence Meteorological Satellite Program* since 1987. The sun synchronous orbit, the period of about 100 minutes, and the sensor's swath width of 1394 km allow for a regular coverage of the polar regions at least once a day (Hollinger et al., 1987). Its 19 GHz and 37 GHz channels have a resolution of 25 km. The 85 GHz channel reaches the double resolu-

tion of 12.5 km, but is more sensitive to atmospheric influence. SSMI was preceded by the *Scanning Multichannel Microwave Radiometer* SMMR on the NIMBUS 7 satellite from 1978 to 1987. It provides information on 5 frequencies from 6 to 37 GHz (Cavalieri et al., 1984).

Drift vectors are estimated by tracking features through consecutive images of the area. Maximum cross correlations within a moving search window in the target images allow for the recognition of significant structures and, hence, of the appropriate displacement vector (Fig. 3.1). Atmospheric conditions such as clouds and humidity, represent limitations of this method, as do changes of the surface parameters of the tracked feature by melting, snowfall or ridging, and fast deformation or rotation, which aggravate the retrieval.

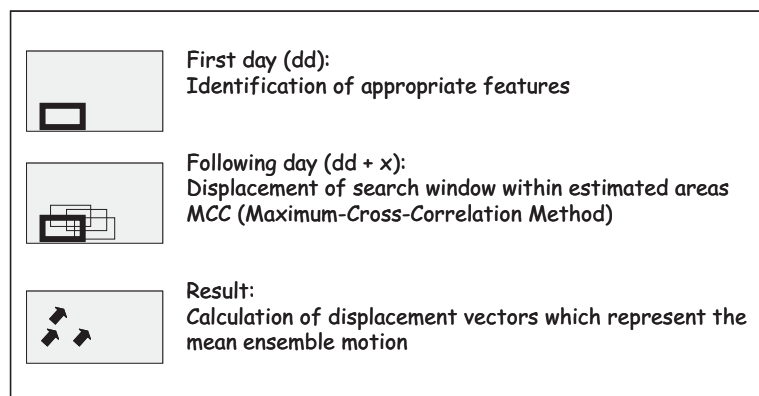


**Figure 3.1:** *Satellite drift estimation principle.*

Agnew et al. (1997) describe detailed methods for the calculation of sea ice motion from 85 GHz data. They give a theoretical error of these estimations of about 4.6 km/d, thus accounting for the geolocation error, tracking error, swath smearing effect, and timing error. Velocity errors are divided by the time interval between the images; longer time intervals between the images compared lead to a decrease in errors. This results in a worse temporal resolution and greater tracking inaccuracies, since the recognition of tracked features is more difficult after longer periods. SSMI drift data are available as optimal interpolated and not interpolated 37 GHz and 85 GHz

values, with errors in 37 GHz being smaller than expected compared to the double-resolution 85 GHz channel (Maslanik et al., 1998).

Drift estimates are calculated every second day and available from 1979 to 1997, while one-day calculations exist for the time after 1992 only (since the 85 GHz channel was available on SSMI only more recently). The size of the search window of the feature tracking algorithm also affects the results, because a large window reduces noise, but also leads to more spatial averaging and, hence, reduces the number of independent velocity vectors (Lemke and Martin, 2001). The search window size determines the spatial resolution of the acquired drift vectors. The ground resolution of the pixels and the temporal intervals between two images determine the minimum detectable velocity.

For this investigation, *SSMI Optimal Interpolated Data* (thereafter referred to as *OI-data*) are used. Results from the 37 GHz and the 85 GHz passive microwave radiometer channel are combined with additional drift information from buoys when geographically and temporally available.

The data are calculated with a weighting function according to Kwok (2000):

$$\vec{v} = \sum_i^{85GHz} \alpha_i v_i + \sum_j^{37GHz} \beta_j v_j + \sum_k^{buoy} \gamma_k v_k \quad (3.1)$$

using the two channels with different spatial resolution on a final rectangular grid with 100 km grid spacing. The weighting coefficients  $\alpha$ ,  $\beta$ , and  $\gamma$  are determined according to Colony and Thorndike (1984). Solutions for each point are obtained at each point based on the uncertainties, the expected variance of the motion, and the distance from observations available (Kwok et al., 1998). The correlation lengthscale varies between 300 km near the coast up to 800 km within the pack (Kwok, personal communication, 2003), which is in agreement with measurements (Kottmeier et al., 1992).

The OI-drift data from SSMI and SMMR are available only for the months from March to November because satellite ice drift products cannot be derived for the austral summer. The ice surface properties decorrelate and prevent tracking during the melt season. Data are available with one-day and two-day resolution, the two-day resolution covering the longer time span from 1979 to 1997. For homogeneity reasons, the two-day resolution data are

used for this analysis.

In addition to the information about sea ice motion, ice concentration data are utilised from the EU-funded Project PELICON *Project for Estimation of Long-term Variability in Ice Concentration* (Heygster et al., 1996). For temporal constancy with drift information, data calculated with the NASA2 Team algorithm (Comiso et al., 1997) are chosen, which are available for the whole examination period. The algorithm uses 17 and 37 GHz channels to derive ice concentrations from brightness temperatures. The PELICON algorithm applies a correction scheme by Thomas (1998) for areas with ice an concentration below 50%, which reduces concentration overestimation due to atmospheric influences.

## 3.2 Data from Drifting Buoys

Data from buoys drifting on sea ice floes and measuring meteorological parameters may provide a better temporal and spatial resolution than satellite based data. Sea ice drift velocities from buoys are collected in the *Atlas of Antarctic Sea Ice Drift* (Schmitt et al., 2004) for a comprehensive presentation and for verification of satellite drift fields.

For the most part, data have been provided within the *International Programme for Antarctic Buoys* IPAB since 1995. Former data were collected by the *Alfred-Wegener-Institute* AWI. The absolute number of buoys per month has continuously increased (Fig.3.2), with exceptions of some years. During the first decade, the buoys were mainly concentrated in the Weddell Sea, drifting towards the adjacent parts of the Indian Ocean. In the later years, drift data from all ocean basins around Antarctica were available. Ice drift is calculated from the change of buoy positions reported at different times by the Argos data collection and localisation system. The accuracy of the ice drift and its derivatives is estimated from the *rms* (root mean square) error of Argos positioning at approx. 350 m by the Doppler shift of the transmission frequency at different satellite positions. It is assumed that position errors are Gaussian-distributed and temporally uncorrelated, which is confirmed by the Argos positioning of an automatic weather station on the Filchner-Ronne Ice Shelf.

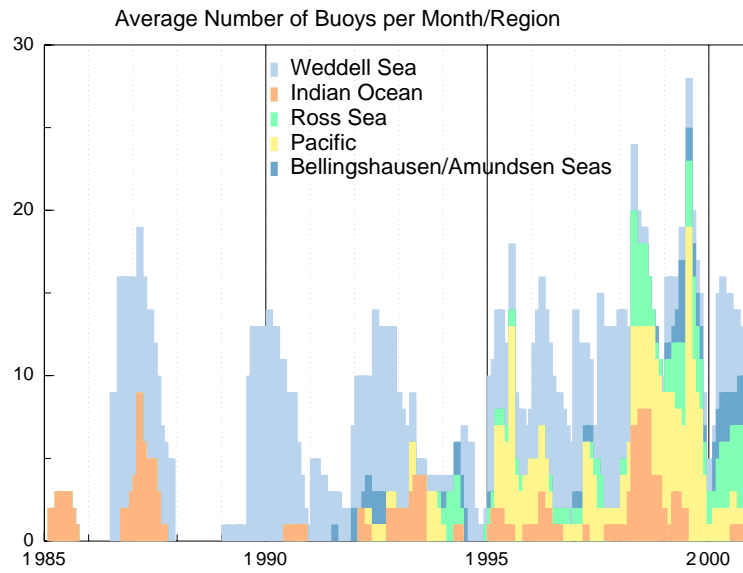


**Figure 3.2:** Monthly mean number of Antarctic buoys in different regions. Weddell ( $300\text{-}30^\circ\text{E}$ ), Indian ( $0\text{-}90^\circ\text{E}$ ), Pacific ( $90\text{-}160^\circ\text{E}$ ), Ross ( $160\text{-}230^\circ\text{E}$ ), Bellingshausen/Amundsen ( $230\text{-}300^\circ$ ).

Position reports of different temporal intervals are interpolated to 3h resolution, with gaps being filled by linear interpolation between two points to obtain regularly spaced time series, see Kottmeier and Sellmann (1996) for details. The errors of the ice drift components decrease with increasing averaging period. Typically, they are 4.6 cm/s for three-hourly data and around 1 cm/s for daily data. From 1994 onwards several buoys have been equipped with Global Positioning System (GPS) receivers which provide an improved location accuracy. Using the GPS transmission of the Standard Positioning Service (SPS) and averaging times of 10 min, position accuracies of better than 50 m are obtained. The errors of the drift velocity for daily data goes down to 0.3 cm/s.

### 3.3 Meteorological Data

Model output data from *NCEP Reanalysis Project* (NNRP) datasets, a 40 year record of global analysis of atmospheric fields, are used to combine ice drift and atmospheric parameters. The basis of this long-term reanalysis dataset is to use a fixed system for assimilation, analysis, and forecasting using the data from 1957 to the present. This allows for an investigation of interannual variability ensuring that model changes do not influence the results. It includes land surface, ship, rawinsonde, pibal, aircraft, satellite, and other data from various organisations. For an analysis that is as accurate as possible for the past 40 years, all data available at given times are used by applied data assimilation schemes. Additional information is available from Kalnay et al. (1996). In newer investigations of the synoptic variability in the Southern Ocean, Simmonds et al. (2003) use an enhanced NCEP-2 dataset (Kanamitsu et al., 2002) that excludes errors like the ones caused by the Australian PAOBS sea level data. With the influence of this error decreasing for longer averaging timescales (Kistler et al., 2001), the *40-year Reanalysis* dataset should be sufficient for the investigation and is treated in a way similar to that described in Venegas et al. (2001).

The datasets in use were pressure level partition or surface data on a  $2.5^\circ \times 2.5^\circ$  latitude/longitude grid and have a temporal resolution of 6 hours. Sea level pressure and temperature and the wind velocity components from the lowest model level (1000hPa) are used for further investigation. Although 1000 hPa is mostly below MLS, winds at this pressure level provide reasonable estimates of surface geostrophic winds.

## 3.4 Data Preparation

The following steps were undertaken to obtain homogeneous, temporally averaged datasets of vector and raster data from all different datasets.

- **Georeferencing**

Data with Cartesian x-y coordinates like the SSMI and PELICON data are converted into latitude-longitude coordinates according to the grid in which they exist. Georeferencing is done using the Hughes ellipsoid with a latitude of true scale at 70°S. This leads to the smallest distortions in length in the areas around Antarctica's coast, where most of the sea ice processes take place.

- **Temporal averaging**

Employing daily data, the following different mean values are calculated. Due to the restricted availability of satellite products of only nine months per year, there are monthly means from March to November, seasonal means for the three seasons of March-May (autumn), June-August (winter), and September-November (spring), and annual means including all nine months. For the same three averaging intervals, interannual means, including the mean of a month or period, of the complete data range from 1979 to 1997 are available. Due to an average ice motion of around 200 km in 30 days (Kottmeier and Sellmann, 1996), a spatial averaging of ice drift must be taken into account in the mean values.

Raw buoy data of variable temporal resolution from hours to days are checked and controlled carefully, and then put together to daily means. These data as well as daily means of 6-hourly NCEP data shall hereinafter be treated like the satellite data to calculate monthly means and statistics, so that the monthly or seasonal temporal variances always relate to daily input values.

### 3.4.1 Statistical Parameters and Covariance Ellipses

Statistical values like the variance  $\sigma_i$  (Eq. 5.3) of each velocity component, the complete drift variance, and covariance (Eq. 5.4) are calculated for all

datasets. For a better illustration of the coupling variability, covariance ellipses are calculated and plotted. Similar to vector arrows, their size and orientation describe the magnitude of the variance as well as the relation of variance in the longitudinal u-component and meridional v-component. The covariance ellipses are derived from the covariance matrix as

$$C = \begin{pmatrix} \sigma_1^2 & cov(x_1, x_2) \\ cov(x_1, x_2) & \sigma_2^2 \end{pmatrix}$$

with  $\sigma_1$  and  $\sigma_2$  being the standard deviation and  $cov(x_1, x_2)$  the covariance between the two velocity components. The inverse of this covariance matrix  $C$  is included in the exponent of the probability density function for normally distributed variables. When looking for curves of the same probability density, the exponent is set constant. This leads to the equation of an ellipse with its point of origin shifted in the coordinate system and its axes turned by an angle  $\alpha$  from the normal axis of the system. After coordinate transformation to the principal axes of the ellipses, the new equation is comparable to a general equation for ellipses

$$\frac{x^2}{p_1^2} + \frac{y^2}{p_2^2} = 1 \quad (3.2)$$

with the semi-major axes  $p_1$  and  $p_2$ . These axes as well as the turning angle  $\alpha$  can be expressed by the variance and covariance of  $x_i$ . Details for calculation and interpretation can be found in Appendix A.1.

### 3.4.2 Interpolation of Gridded Fields

The SSMI and NCEP data are imported into the GIS as vector data with their geographic coordinates for positioning and the drift components and statistic values being vector attributes. For evaluation of climatological patterns and changes in sea ice motion and atmospheric data over the last 20 years, gridded fields of these values are best to use.

The fields of sea ice motion, drift variance, pressure, and temperature are created by interpolation of vector data to raster data. Interpolation is done by using a nearest-neighbour-interpolation with 6 nearest neighbours (i.e.,

the 6 nearest of all sample points to the grid point in question) weighted by their distances from the grid point. The interpolation equation then is:

$$Z_{xy} = \frac{\sum_{i=1}^k \frac{Z_i}{D_i^2}}{\sum_{i=1}^k \frac{1}{D_i^2}} \quad (3.3)$$

Here,  $Z_i$  are values of each  $k$  nearest neighbour and  $D_i$  are the distances from the current grid point, the value of which is to be interpolated. For each grid point, the  $k$  nearest neighbours have to be identified from the entire data set before the distance-weighted equation is employed. This spatial interpolation range for single grid points is similar to the interpolation of gridded fields from buoy positions with an acceptance circle of approx. 300 km, as it was done in Kottmeier et al. (1997). All gridded fields related to ice motion data are circumscribed by the ice margin derived from PELICON data. As drift vectors often are not available at all points of the ice-covered region, interpolated values are only representative in the regions with drift arrows drawn.

The following figures show exemplary results of monthly means of these datasets for November 1982. They give information about the general state of the atmosphere and the response of sea ice dynamics.

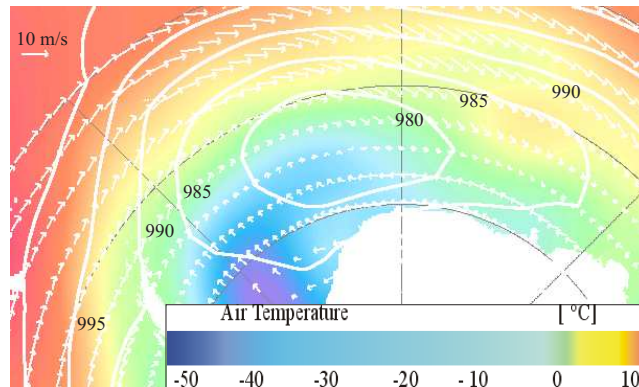


**Figure 3.3:** November 1982 mean synoptic field. The temperature distribution is in accordance with the colour bar, isobars are plotted in 5hPa increments, and the scaling arrow for wind velocities indicates 10 m/s.

In the section of the meteorological chart (Fig. 3.3) a low pressure system is centred over the northern Weddell Sea. The corresponding wind field shows the expected pattern with wind vectors surrounding the pressure centre in a clockwise manner. According to the mean wind field, lowest temperatures occur in the southern Weddell Sea, forced by cold winds from the continent, while the southward flow around 10°E advects warmer temperatures.

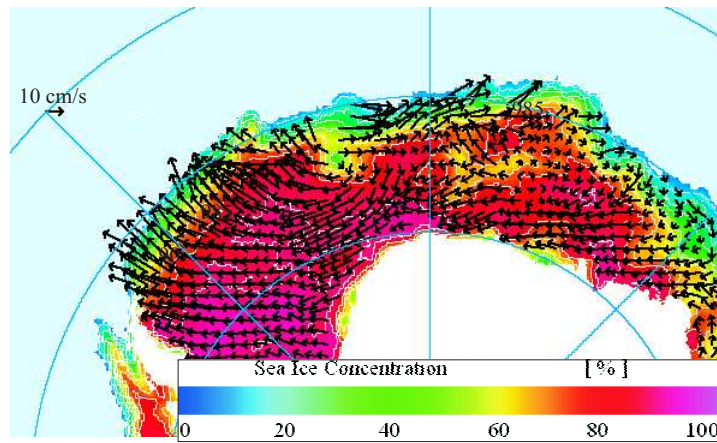


**Figure 3.4:** *November 1982 mean sea ice concentration and ice drift arrows. The scaling arrow indicates 10 cm/s.*

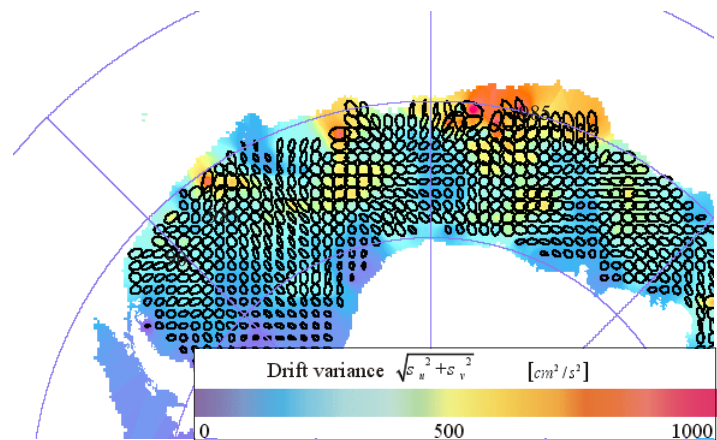


**Figure 3.5:** *November 1982 mean variance field with corresponding covariance ellipses (calculated according to A.1).*

The sea ice motion field of the same month (Fig. 3.4) shows a similar drift pattern, with the typical gyre displaced to the northeast. Thus, uniform northwestward drift prevails in the central Weddell Sea. Only at the barrier of the peninsula does the motion turn directly northwards. Of the underlying field of mean ice concentration, a small area of apparently lower concentrations exists in the centre of the low pressure system. Reduced concentration values also occur around 10°E and at the eastern coast of the Weddell Sea. While the first concentration decrease can be attributed to the advection of warmer air, the second occurs as a result of the strong seaward forcing winds and ice motion, a mechanism that also is an important factor in building up coastal polynyas.

The corresponding field of variance (Fig. 3.5) shows the magnitude of the monthly mean variance at each gridpoint. The overlying covariance ellipses give information beyond these values. The size of the ellipse is given by the general magnitude of the variance, while its shape (stretched or circular) shows the size of the impact of the meridional or zonal drift component. Additionally, the axes of these ellipses are not always parallel to the axes of the geographic coordinate system. The turning angle  $\alpha$  depends on the correlation coefficient between the two parameters and may have a positive or negative sign. One centre of high variance values is coincident with the centre of the low pressure system. Interestingly, another area with high variance values can be found east of this centre, in the areas that also have lower concentrations. In the central Weddell Sea, where ice motion has a stronger zonal component than usual, the ellipses show more meridional orientation, indicating that the main contribution of total variance comes from deviations in this direction. Directly in the main pressure centre, the shape is round, which reflects regularly distributed influences on variance from both velocity components.

### 3.4.3 Differential Kinematic Parameters

Differential kinematic parameters (DKP) like vorticity, divergence and shear give a detailed overview of the motion of the sea ice field.

In analogy with the mathematical meaning of the divergence of a contin-

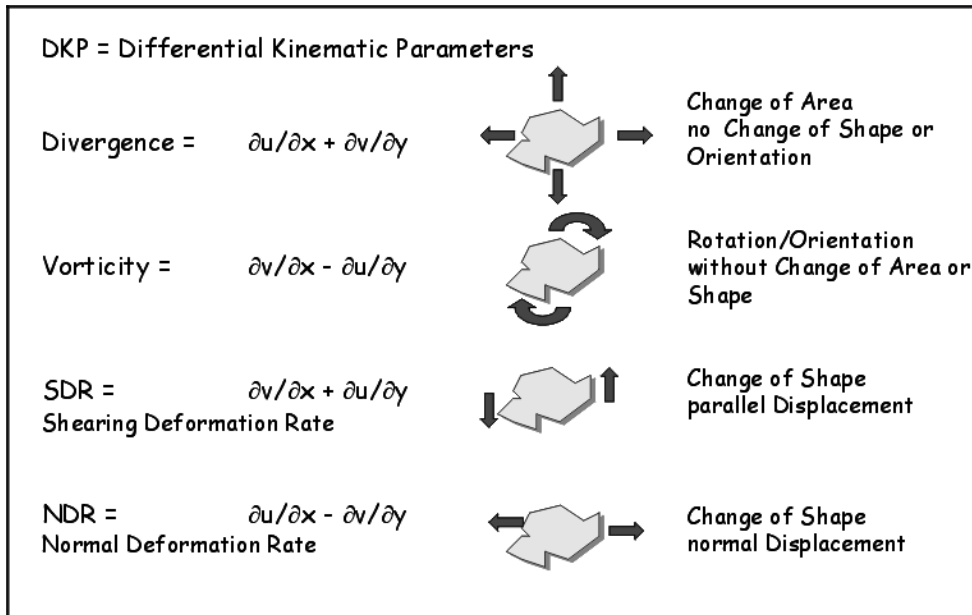


**Figure 3.6:** Schematic overview of the differential kinematic parameters (DKP) of the drift vector and their interpretation.

uous vector field, the **Divergence** of the 2-D vector field of sea ice motion represents the relative change of an area covering all neighbouring ice floes within an enveloping curve, whereas changes of the shape or orientation of these curves do not affect divergence. Divergent ice motion causes an opening of leads and enhanced heat losses from the ocean in direct contact with the atmosphere. Convergent ice motion decreases the size of leads between the floes and may result in larger internal ice stress.

**Vorticity** describes changes of the orientation of the enveloping curve. Ice drift vorticity was empirically found to be related to the vorticity of the geostrophic wind (Kottmeier and Sellmann, 1996). This is mainly documented by the investigation of buoy drift for certain regions and can be seen here for all areas and longer periods.

**Shear** causes the changes in shape, having two components in the direction of the mean motion and perpendicular to it. The shear rate of ice drift is found to be relatively close to the shear rate of the geostrophic wind field in case studies of drift.

To suppress effects of noise errors of zonal velocity  $u$  and meridional component  $v$  on derivatives, the spatial increments  $dx$  and  $dy$  are chosen to be 600 km, which comes close to correlation lengths of ice motion detected in many investigations of ice motion in the Southern Ocean. For different seasons during the Winter Weddell Sea Project (WWSP), Kottmeier et al. (1992) calculated the spatial correlation lengths of the buoy drift speeds and components. The longitudinal correlation lengths of the drift speeds varied between 490 and 680 km; the lateral ones between 270 and 540 km. Vihma et al. (1996) provide correlation lengths of 700 km for the longitudinal and of 550 km for the lateral drift speeds in the central and western Weddell Sea. As a result of the large correlation lengths, spatial gradients of ice drift obtained from SSMI reflect vorticity and divergence on these scales. Smaller-scale DKPs may be much more important to lead and polynya formation (Timmermann et al., 1999), (Eisen and Kottmeier, 2000), but cannot be obtained reliably from SSMI-based ice drift.

For the ice motion field of November 1982 presented above (Fig. 3.4), the differential kinematic parameters are now presented with overlying ice motion vectors to illustrate the motion field. Highest values of shear (Fig. 3.7) occur along the  $0^\circ$  meridian in an area that is east of the main centre of low pressure. The sharp change-over between the clockwise rotation around the low pressure and a neighbouring westward drift gives rise to large differences in drift direction and, thus, causes high tension and deformation in the ice field. Higher shear values also exist on the eastern Weddell coast, where strong seaward motion pushes the ice away from the coast, creating areas of open water and areas of higher compressed ice in the direction of mean forcing. Near the oceanic ice margin, high shear values generally occur under the influence of an abrupt change of direction, e.g. when the ice is carried along and accelerated by ACC, while higher shear exists between the immobile and the moving parts of the ice cover at the coastal boundary.

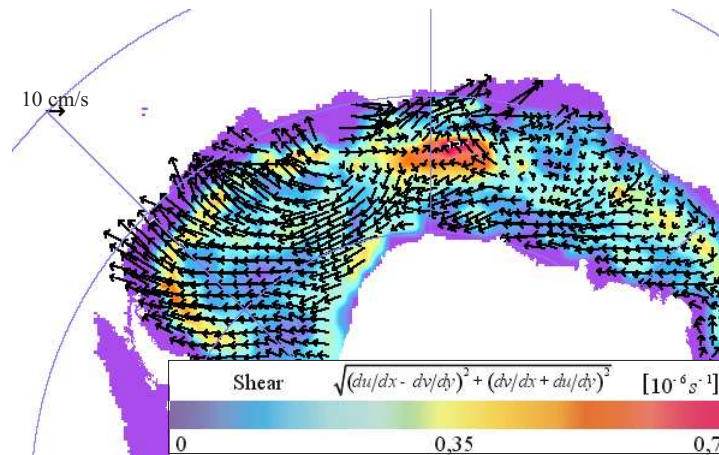


**Figure 3.7:** November 1982 ice motion shear and ice drift arrows. The scaling arrow indicates 10 cm/s.

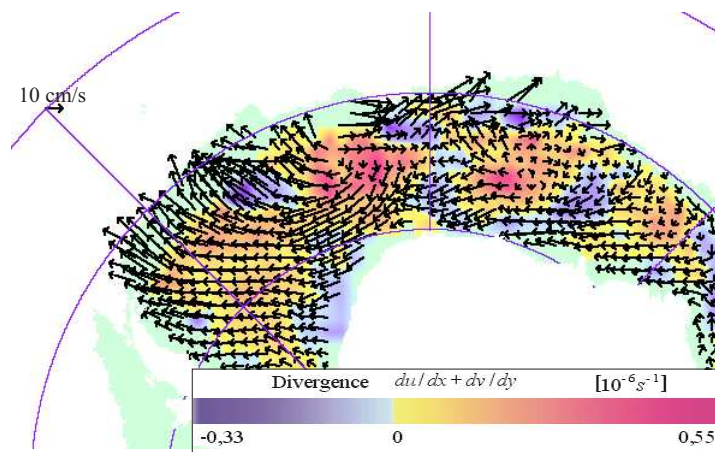


**Figure 3.8:** November 1982 ice motion divergence and ice drift arrows. Fields of divergence are blue and those of convergence red. The scaling arrow indicates 10 cm/s.

The corresponding image of ice motion divergence (Fig. 3.8) shows divergent motion patterns in the centre of the low pressure system, in the central Weddell Sea, and east of the  $0^\circ$  meridian. Convergence of the ice motion field occurs in the northern Weddell Sea, where ice escaping from the gyre meets with a northward drift from the central Weddell Sea (Padman and Kottmeier, 2000). From the field of vorticity (Fig. 3.9), it is evident that the vorticity of the ice follows that of the atmosphere. Positive vorticity values occur, when the ice motion vector circle around the low pressure system in a clockwise manner, while negative vorticity dominates in the southern Weddell Sea that is already influenced by the opposite pattern of higher pressure (Fig. 3.4).

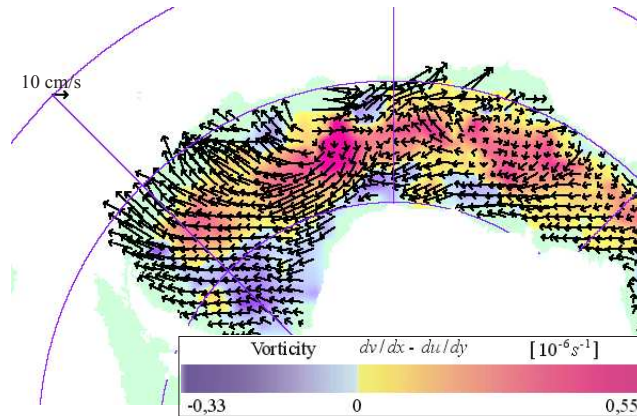


**Figure 3.9:** *November 1982 ice motion vorticity and ice drift arrows. Fields of positive vorticity are red and those of negative blue. The scaling arrow indicates 10 cm/s.*

Concurrence of largest drift divergences with the areas of lower ice concentration (Fig. 3.4) illustrates the influence of sea ice dynamics on the ice cover. The divergent sea ice motion that is enforced by winds according to the local pressure situation directly results in the change of ice concentrations.

## 4 Validation of Satellite Ice Drift

To compare the long-term variability of ice drift data from different measurement principles, an intercomparison and verification of differences and bias is necessary. Generally, a quality index for satellite data is helpful for the validation of modelling outputs with this satellite data. The collection of buoy data in the *Atlas of Antarctic Sea Ice Drift* (Schmitt et al., 2004) allows for a use of buoy data from different sea-ice regimes to investigate differences of seasonal bias and *root-mean-square error* (rms) of the satellite data. The uncertainty relating to these different conditions will be revealed and, hence, a quality flag for different seasons and regions of OI satellite drift data will be provided.

Detailed comparisons of satellite drift data with drifting buoy measurements (Maslanik et al., 1998; Kwok et al., 1998; Geiger et al., 2000) show that it is not sufficient to just compare a speed value at a certain buoy's position and time to the nearest gridpoint of the SSMI grid. For this purpose, a method is used and tested for best temporal and spatial scales.

### 4.1 Comparison Schemes

As done in the above-mentioned literature, velocities derived from the OI data existing on a regular 100 km spaced grid are interpolated to the buoy's position by radial search. All grid values within a given search radius  $r$  around the actual buoy position are distance-weighted and averaged to a single mean comparison value.

Studies in the Arctic for the SSMI 85 GHz data indicate the best results, i.e. smallest *rms* differences between buoy and satellite drift values for a search radius around 600 km (Geiger et al., 2000), which is in agreement with a length scale of around 1000 km for the dominant wind forcing. Satellite drift data used here were sampled every 1 or 2 days and buoy data were filtered with moving means to obtain comparable values.

In the first step, it was investigated whether the optimal 600 km search radius of the Arctic is applicable to the Southern Ocean or whether there are some

fundamental differences that require a different approach. The sampling time scales for the SSMI-OI data are one day and two days. Hence, the time averaging of buoys should be adapted to this sampling interval. Furthermore, it should be kept in mind that the OI data already are an interpolation product and some artifacts which will not be seen in simple 85 GHz data might be included when performing radial search.

OI and 85 GHz data are compared with different time-averaged buoy data to find out the best combination. The comparisons are first done for the year 1992, where two buoy clusters, one close to the coast of the Antarctic peninsular and the other in the central Weddell gyre, also allow to look at regional effects.

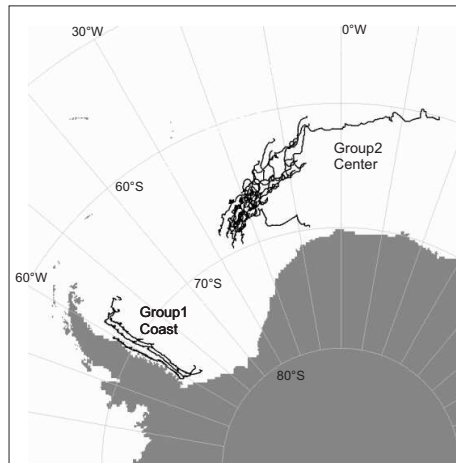


**Figure 4.1:** *Weddell buoys 1992 and their division into two groups.*

In the coastal regions of the western Weddell Sea more perennial ice is expected and the buoy motion is constrained with the ice being compressed against the coastal barrier. In contrast to this, the central region consists predominantly of seasonal ice with relatively free drift and divergent motion (Kottmeier and Sellmann (1996), Drinkwater and Kottmeier (1994), Drinkwater (1998), Drinkwater et al. (1999)).

For comparison, OI and 85 GHz data are used. OI drift calculated every second day is available from 1979 to 1997, while one-day calculations exist in the time after 1992 only, since the 85 GHz channel was available on SSMI more recently only. To investigate long timeseries and statistics and detect interannual variability and change, the two-day data (hereinafter called 2d) which cover the longer time span are mainly used here. In this way, problems of non-uniformity and differences in data sets resulting from different channels, sampling intervals, and dataset duration are avoided. The choice of 2d

drift is also due to the improved tracking accuracy of these products. By comparison, accuracy differences between one-day and two-day data can be revealed. The basic buoy data are already preprocessed and error-corrected and contain the 3-12 hourly position, calculated drift, and additional values, measured according to the buoy's equipment. To fit to the satellite data and other daily data, daily fixed means (*b1*) are calculated from the daily fixed interval 00:00 - 24:00 hrs, centred on 12:00 hrs. It should be kept in mind that the 2day OI drift values for one day  $d$  are calculated by using the displacement from day  $d + 2$  to day  $d$ . It is therefore useful to calculate 3-day sliding means for the buoy velocities (*b3*) to be comparable to the satellite time interval (spanned by the satellite drift products) and to filter tidal and inertial loops out of the buoy records.

#### 4.1.1 Interpolation and Error Calculation

For each day and buoy, the nearest gridded satellite drift vectors are interpolated to a specific buoy location within a fixed search radius using a weighted distance method.

Search radii vary from 200 km, the range which comes close to the GIS borders of calculating gridded fields from the 12 nearest neighbours (described in Section 3.4), to ranges between 600 to 800 km as used in Geiger et al. (2000) for the Arctic. For each day and buoy, the velocity difference between satellite and buoy is calculated for different dataset combinations. To obtain an overview of how different conditions (season/regions) influence the magnitude of the *rms* error, separate regional investigations are performed.

For the 1992 investigation, three different seasons and two different examination regions are defined, as described in more detail in Appendix A.2. For the radius range between 200 and 600 km, rms differences are calculated using different dataset combinations. The satellite-buoy data combinations are named as follows:

2day SSML\_OI data + b1 buoy data  $\Rightarrow$  OI2\_b1

2day SSML\_OI data + b3 buoy data  $\Rightarrow$  OI2\_b3

2day SSML\_85V data + b1 buoy data  $\Rightarrow$  85V2\_b1

2day SSML\_85V data + b3 buoy data  $\Rightarrow$  85V2\_b3

### 4.1.2 Comparison Results for Weddell Zones

The influence of different search radii ranging from 200 to 600 km on the error size is investigated. Fig. 4.2 gives an overview of all regions rms and bias for the different seasons of the year 1992.

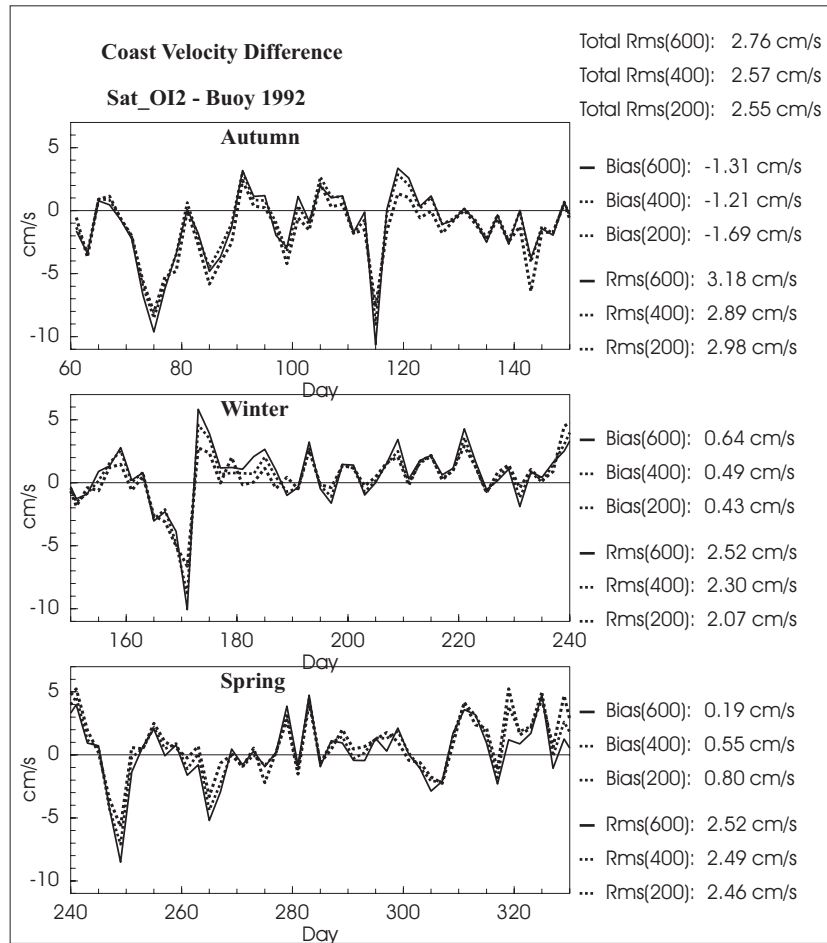


**Figure 4.2:** Example of 1992 comparison of rms error and bias (in cm/s) for different search radii on each day of the year for the coastal buoys in the Weddell region. Solid and dashed lines give the RMS errors for different search radii. Values on the right are seasonal means.

The rms errors resulting for all comparison schemes are presented in Fig. 4.3. In all cases, the error magnitude reaches its lowest values for the combination OI2\_b3, which implies that the OI data describe the motion field better than the non-interpolated data and that the 3d moving window averaging method for sampling the buoy data minimises the rms difference between satellite and buoy drift and, hence, is better than the 1day buoy means. This result is consistent with some of the findings of Geiger and Drinkwater (2001).

	All oi_b1	All oi_b3	All 85_b1	All 85_b3	Coast oi_b1	Coast oi_b3	Coast 85_b1	Coast 85i_b3	Center oi_b1	Center oi_b3	Center 85i_b1	Center 85_b3
R600	4.83	3.22	5.18	3.75	4.45	4.51	4.60	4.77	9.46	4.49	10.59	6.37
R400	4.45	3.29	4.95	3.99	4.31	4.43	4.70	4.97	8.88	4.59	9.93	6.60
R200	4.16	3.31	4.94	4.42	3.94	3.99	4.97	5.28	8.42	5.00	9.53	7.06
R600a	3.59	2.89	3.60	2.91	4.61	4.08	4.35	3.77	-	-	-	-
R400a	3.50	2.84	3.53	2.95	4.52	4.07	4.30	3.86	-	-	-	-
R200a	3.32	2.70	3.62	3.24	4.32	3.88	4.47	4.27	-	-	-	-
R600b	3.99	3.16	4.47	3.70	4.60	4.77	4.41	4.53	7.95	3.89	9.03	6.17
R400b	3.70	3.14	4.31	3.82	4.40	4.68	4.48	4.63	7.45	3.74	8.62	6.10
R200b	3.36	2.99	4.21	3.85	3.80	4.08	4.44	4.49	7.21	3.98	8.47	5.95
R600c	6.42	3.56	6.88	4.46	4.21	4.73	5.04	5.76	10.51	4.81	11.46	6.52
R400c	5.79	3.82	6.48	4.89	4.09	4.65	5.29	6.11	9.63	5.02	10.66	6.90
R200c	5.45	4.08	6.41	5.64	3.76	4.13	5.81	6.58	9.06	5.50	10.09	7.59

**Figure 4.3:** *RMS error of drift velocity for different data combinations in 1992. The search radius is 200, 400 and 600 km and seasons are a(autumn), b(winter) and c(spring). Smallest values for each region are shaded.*

As regards the different influences of search radius, regions, seasons, and temporal averaging, the results of Fig. 4.3 are summarised as follows:

### On the search radius

In most cases the 85V2/b3 comparisons yields the best results (i.e. minimum rms differences) at a search radius of 600 km with typically a fairly continuous decrease in rms difference between 200 and 600 km. Further examinations with increasing radius up to 800 and 1000 km show the opposite with an increase of the rms difference. Consequently, the search radius was set to 600 km. In the OI data, the minimum rms difference is reached by the r600 minimum when looking at the total dataset only. However, the way the minima differ between the different search ranges is smaller than in the non-OI case.

In the coastal region, the minimum for the OI data is clearly found at the smallest search radius of 200 km. The rms error decreases slightly again when the search radius goes beyond 800 km. In contrast to this, the minimum of not interpolated data for the same region is still decreasing with increasing the radius.

Apparently, the smaller search radius for optimal interpolation used in the vicinity of the coast affects the consistency between buoy and satellite data. It is best for the r200 comparisons. In the central Weddell region, longer correlation scales were used for optimal interpolation. Here, smallest error values occur at 400 km. However, long correlation length scales can be found due to stress transfer. Probably because the correlation length scale is larger in certain configurations.

Despite this regional effect, the error values show, that for non-interpolated data an optimal search radius of around 600 km, as it was used in the Arctic studies by Geiger et al. (2001) can also be used in the Antarctic region. Interpolated data exhibit quite smaller rms differences than not interpolated ones, but the dependence on the search radius is superposed by the effect of the interpolation radius used to calculate the OI data.

### On the temporal windowing for buoy data

As described above, the best temporal window for comparing the buoy data with the satellite 2d ice drift velocity data seems to be the 3day sliding means. In most cases, the rms errors decrease considerably. In the central Weddell

region, the improvement is strongest, because the higher frequency variations in the buoy drift data caused by tidal and inertial oscillations are removed by this smoothing. In coastal regions, it is not so obvious which is the best method of comparison, because the buoy movement here is always constricted as a result of compact ice conditions and exhibits a lower frequency variance. In the few cases considered, there is a chance that the rms difference becomes larger as a consequence of buoy smoothing, particularly during the winter months.

### **On the different regions**

In general, rms differences in the coastal area are larger than at other locations, and data from this region do not appear to show a clear dependence on the averaging interval, search radius or temporal season like the other data do. When measuring in the region of perennial ice, the buoy data appears to be less influenced by the seasonal cycles. When comparing the OI data and 3day smoothed buoy data, the error always is smallest when data are compared within a 200 km search radius. The ice motion here is limited with ice being compressed and ridged near the coast. In these areas, the correlation length scales even become smaller, which explains the best values from the nearest positions around. Another effect already mentioned for OI and 85 GHz is that the error continues to decrease with increasing search radius. For buoys positioned near the Antarctic peninsular, a big search radius could even include data from the western side. The errors for the data from the central Weddell Sea show a similar behaviour like the data of the complete set. However, the r400 error is smallest for OI data.

### **On the different seasons**

With the satellite motion products only available for the months 3 - 11 (Mar - Nov), seasonal rms and bias were computed for the seasons of autumn (months 3,4,5) winter (months 6,7,8), and spring (months 9,10,11). For the total area as well as for the coastal one, the OI rms differences generally reached their smallest values in the spring period, when the ice melts. Here, the smallest error for all comparisons was reached. The examination period

1992 did not contain any autumn data in the central Weddell region, for the next two periods, however, rms differences are smaller for the winter season and reach height values in spring, when the melting starts, which has more effect in this region than in the coastal one.

### On the bias

With the OI2\_b3 data combination being found to be overall best, the seasonal bias for these data was examined. The differences are always calculated

	All	Coast	Center
A March-May	1.26	2.86	-2.09
B June-August	1.61	4.65	-0.41
C September-November	-0.05	4.55	-1.37

**Table 4.1:** *Seasonal bias in cm/s for r600 interpolation on OI2\_b3 data combination.*

by subtracting the buoy velocity from the satellite value  $v_s - v_b$ . Consequently, positive bias values mean that the satellite velocity is higher than that of the buoys, while negative values show the satellite data tend to underestimate the buoy drift. Values cover a large seasonal and regional range, and it is difficult to make clear conclusions. Coastal regions always have a positive bias which means that the drift is overestimated by the satellites. This is also obvious for the total area. In the central Weddell region all seasons show a negative bias, which indicates that drift is underestimated by satellite data. A clear seasonal dependency is not easy to see, and further investigations with more buoy comparison sets seem to be necessary.

To give a first quality statement concerning the OI data on basis of this examination for the year 1992, the rms error is 2.49 cm/s for the complete area and year when using the 600 km search radius. For seasonal distinctions, an error of 2.32 cm/s may be assumed for autumn, 2.58 cm/s for winter, and 2.31 cm/s for spring. For coastal regions with better comparisons at 200 km search radius, an all-year error of about 3.66 cm/s is calculated. Seasonal

values range from 3.73 cm/s (autumn), over 3.96 cm/s (winter), to 3.60 cm/s (spring). The central Weddell region shows an r600 average rms of 3.19 cm/s, with 2.82 cm/s winter values and 3.42 cm/s spring values.

## 4.2 Examination for all Antarctic Regions

With the best data combinations and interpolation schemes determined above, examinations are carried out for the whole dataset with a 600 km search radius ( $r600$ ) to see whether the rms differences are comparable for a multi-year analysis. During this investigation with a 600 km search radius it should be kept in mind that the rms differences in the coastal areas are smaller when using a smaller interpolation radius.

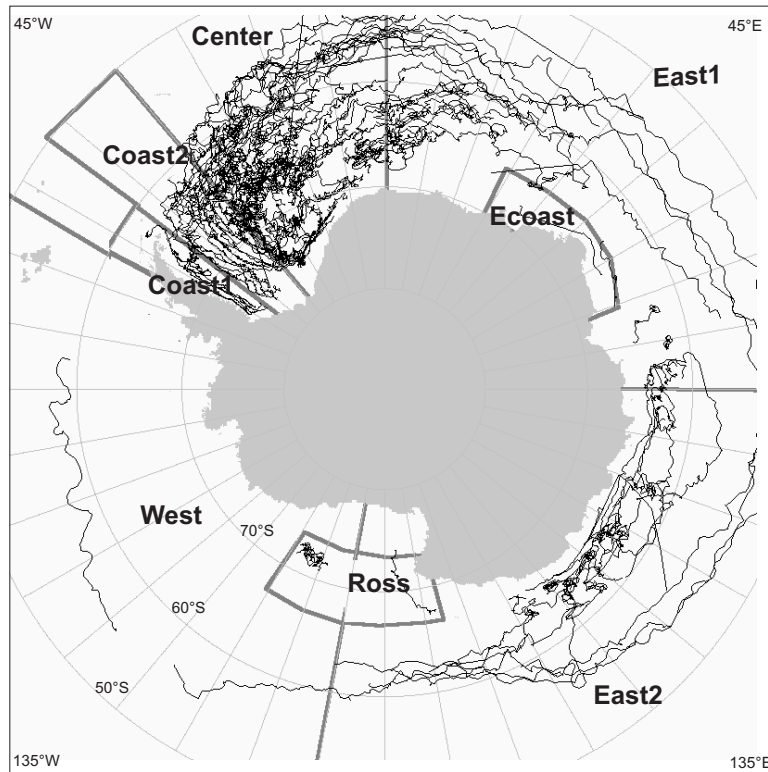


**Figure 4.4:** Tracks of all buoys between 1979 and 1997. Different examination areas are defined according to buoy position and tracks.

According to the regional and temporal distribution of buoys, 9 different examination areas of different ice or circulation regimes were defined. Values for the year 1992 could slightly differ from above, because now, all buoys of the year and not only the selected groups were involved.

<b>Sector</b>	<b>Longitude Range</b>	<b>Latitude Range</b>
Coast1	295 - 305 °E	80 - 50 °S
Coast2	305 - 320 °E	80 - 50 °S
Center	320 - 360 °E	80 - 50 °S
East1	0 - 90 °E	65 - 60 °S
Ecoast	30 - 70 °E	70 - 65 °S
East2	90 - 190 °E	67 - 60 °S
Ross	160 - 210 °E	80 - 67 °S
West	190 - 295 °E	80 - 67 °S
East1out	0 - 90 °E	60 - 50 °S
East2out	90 - 190 °E	60 - 50 °S
Westout	190 - 295 °E	67 - 50 °S

**Table 4.2:** *Names and borders of areas for buoy comparison according to the areas in Fig. 4.4.*

The areas in the Weddell region are similar to the ones used in the previous investigation, with Coast1 (being the former group Coast for 1992) now representing all the buoys close to the Antarctic Peninsular and Coast2 including a new group, that is further away from the coast, but still influenced by its boundary effects and the occurrence of perennial ice.

The central Weddell regions stay the same as in the investigations for 1992. When moving in a clockwise manner, they are followed by the sectors East1 and East2 around East Antarctica and the sector West for the remaining areas, as shown in Fig. 4.4. In the sectors East1 and West, most of buoys are distant from the coast. Hence, small subareas (Ecoast and Ross) are defined to distinguish them from drift regimes in the outer areas. In addition, these three areas are divided into outer regions (East1out, East2out, West-

out) which cover the same longitudinal range but have latitudes smaller than  $60^{\circ}\text{S}$ . This is necessary to separate buoys that already are under influence of the marginal ice zone and the strong Antarctic Circumpolar Current.

### 4.2.1 Comparison Results 1985 - 1997

The total rms differences and bias for all the seasons and regions show that the 1992 data which were investigated in more detail are among those with the best error fits and smallest bias. Similar small values are obtained for the years 1991 and 1995/1996. These are years with a high number of buoy deployments. Hence, it is reasonable that the OI drift based on these data is quite realistic. Further large rms differences appear in 1985, in autumn 1989, in winter and spring 1990, and in autumn and winter 1993. Most of them show a large negative bias, too.

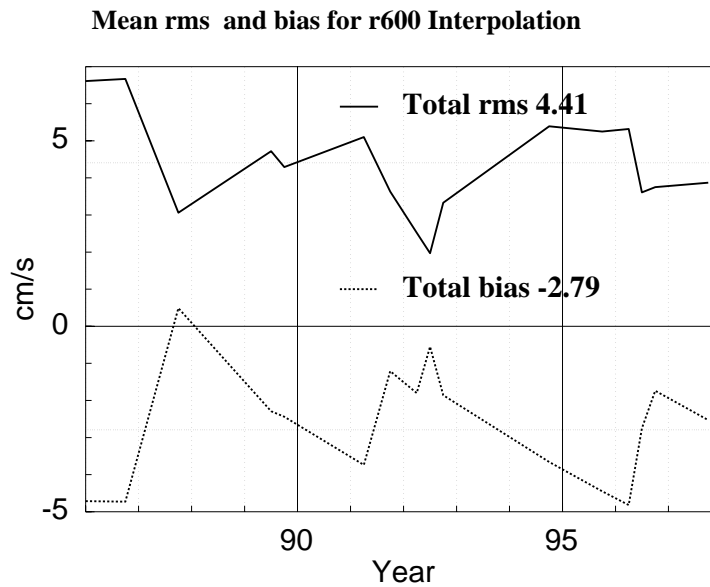


**Figure 4.5:** *Rms error (top) and bias (below) for all seasons and regions in cm/s.*

These differences mainly originate from certain days with events of high buoy velocity. This even applies to the 3day averaged data where the ice drift velocity is significantly underestimated by satellites. Presumably, the

data are not included in the optimal interpolation, since the number of buoys concerned when calculating the OI data differed from that of the IPAB buoy database used for the Sea Ice Motion Atlas. When these strongly varying values are included, the total mean rms error becomes relatively high with 6.37 cm/s. The total mean bias is -3.66 cm/s, indicating a tendency of underestimation of drift values. When neglecting data from the above-mentioned singular events for the investigations, the total mean rms error is reduced to 4.96 cm/s and the bias is -2.62 cm/s (Fig. 4.5). After checking the error peak values with the corresponding buoy data and detecting the one-day velocity peaks, these data were filtered out to obtain a better view of the usual error distribution.

### 4.2.2 Regional Differences

To examine the seasonally varying rms error and bias in more detail, the same values were calculated for all investigation areas and compared in Fig. 4.6. Explicit values can be found in Appendix A.3. As in 1992, the big error peaks are often caused by single events lasting a few days and, hence, do not imply that the whole dataset is wrong. In most of these cases, the coastal buoys show a similar behaviour and a bias close to zero or positive, except for that coastal buoys outside the Weddell Sea on at the coast of East Antarctica. This result here is in agreement with findings of Heil and Allison (1999), who made comparisons for east Antarctic buoys. Ross Sea data do not seem to differ much from the central Weddell data. The largest rms differences occur for the regions, where buoys are already entrained by the motion of the ACC close to the ice margin. They show a consistent negative bias which might be explained by satellite orbits processing in the other direction, resulting in poorer sampling or smearing of the motion due to the composite image formation. Large rms differences with a positive or nearly zero bias always come from coastal regions. Here, satellite drift values seem to overestimate the real drift velocities.

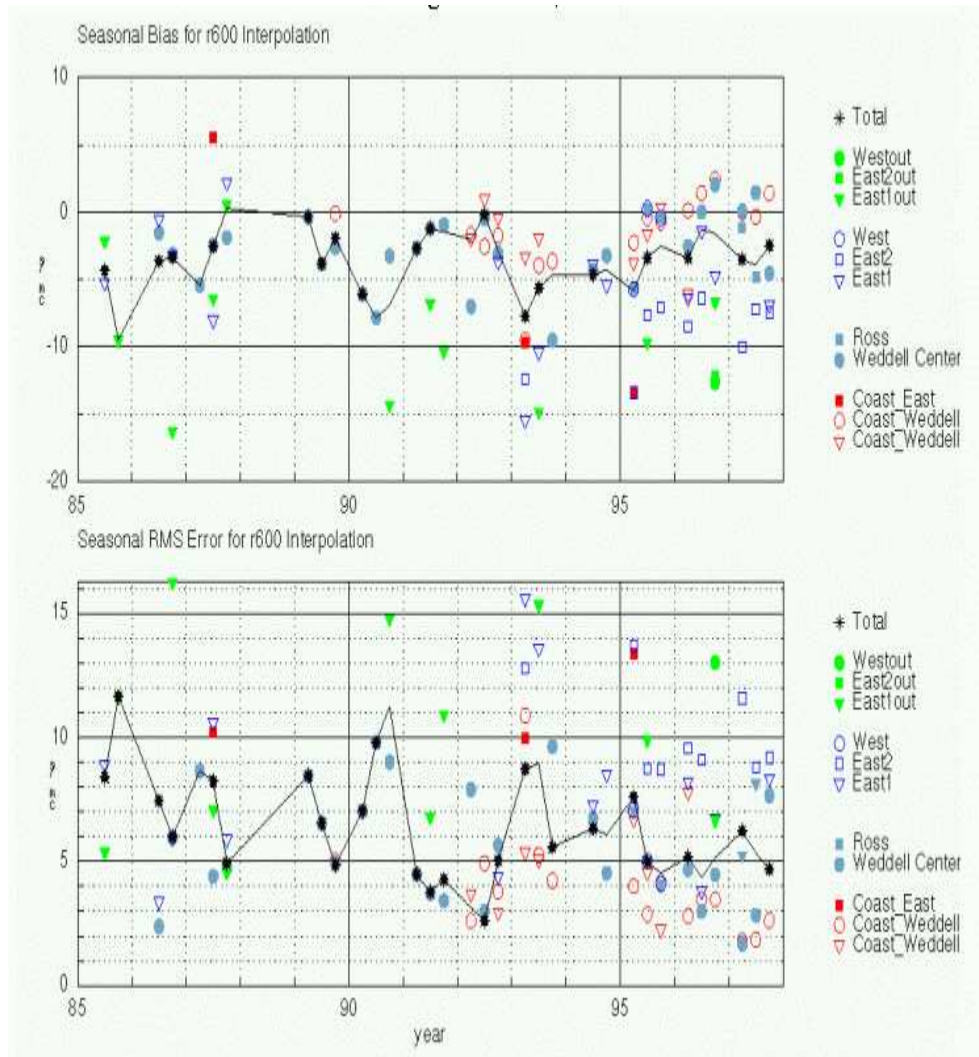


**Figure 4.6:** Total bias and rms error as black lines. The coloured dots show the contribution from the different regions and seasons. The red ones represent the values from coastal regions. The filled blue ones come from the two big basins of the Weddell and Ross Sea. Open blue symbols stand for values from the other regions around Antarctica, the same symbols in green come from the outer regions, north of  $60^{\circ}$ S. Explicit values can be found in Appendix A.3.

### 4.2.3 Detailed Analysis of High Error Cases

With the previous sections giving an overview of the range and distribution of total rms differences, some cases with strikingly high differences remain. Here, a closer analysis of the daily datasets is necessary.

#### Winter season 1986

In this season, a large rms error of about 10 cm/s is obtained with a strong negative bias of 6 cm/s, which means that the satellite data significantly underestimate the buoy drift at one time. The buoy data (Fig. 4.7) show that there is a strong peak of negative zonal velocity (which means westward drift) for some days in August 1996, around day 229. This peak is evident in the data of three buoys.

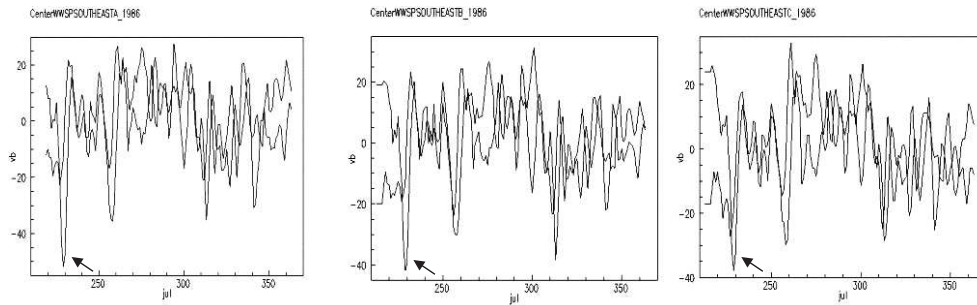


**Figure 4.7:** *Drift components  $u$  and  $v$  for buoys 3291, 3294, and 6574. The arrows point out the strong westward drift around day 229.*

To see, whether this is evident from the satellite data, the overlay of the OI satellite drift vectors from the GIS is plotted in Fig. 4.8. On August 15, 1986, before the velocities increase rapidly, there is a good agreement between satellite and buoy motion. At this time, the southerly cyclone approaching ahead is pushing ice towards the shore.

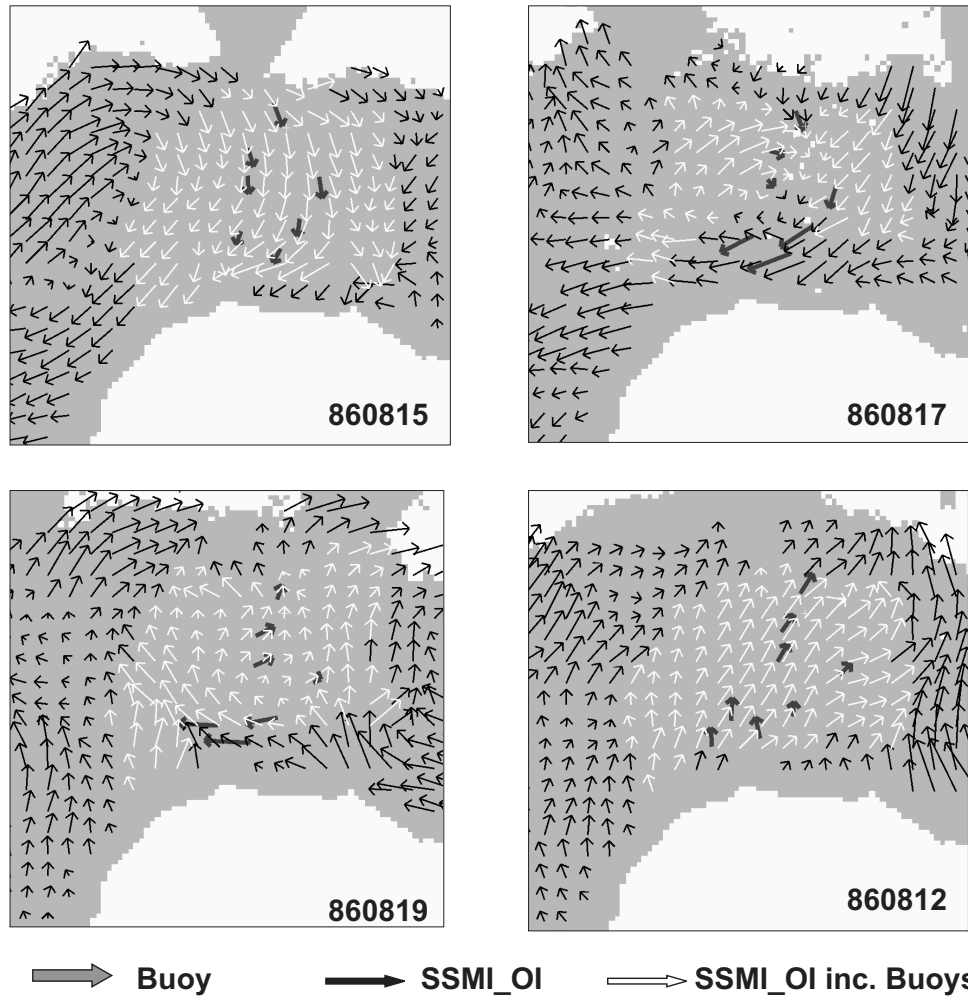


**Figure 4.8:** Comparison of satellite and buoy drift vectors. Satellite OI data are black, when including buoy information in optimal interpolation they are white. Buoy drift is represented by thicker dark grey arrows.

On August 17 and 19, when the strong motion occurs, there is a large difference between the buoys and satellite vectors closest to the coast. For these two days, the optimally interpolated vectors were not calculated by integrating the buoy information, and for some reason the buoy data were filtered or rejected.

This example illustrates the discrepancies that can be found between the two datasets. It also shows the great impact of buoy data on the quality of

satellite products, provided that the OI scheme correctly takes into account rapid adjustments of buoy motion (particularly in near-shore regions, such as this).

### Autumn season 1989

During this year and season, there is a significant mean rms difference, but nearly zero bias. Investigations of the plots of rms differences show that there is a strong daily variation of negative and positive differences in satellite and buoy velocity. This is the reason, why the rms increases, whereas the bias stays relatively low.

### Central Weddell and Outer Regions 1990/1993

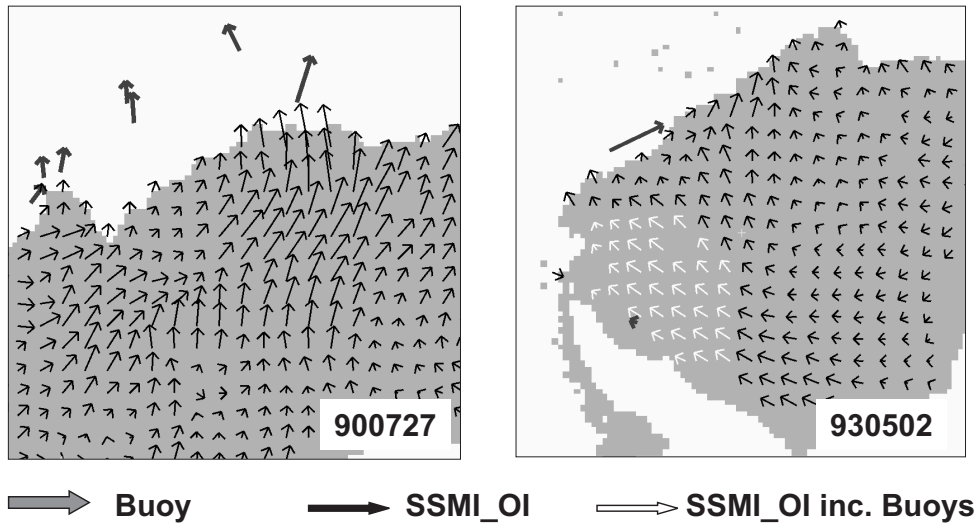


**Figure 4.9:** Comparison of satellite and buoy drift vectors. Satellite data, including buoy information in optimal interpolation, are highlighted.

Large rms differences with a negative a bias are obtained for the central Weddell Sea marginal ice zone and the Weddell Coast2 region for these two years. In both cases shown in Fig. 4.9, the buoy data are very close to the ice edge. In 1990, they are not even included in satellite interpolation, perhaps as a consequence of a combination of rapid ice edge growth and northward ice

margin advection. Since these buoy data are not flagged as outside the ice, these cases go into the comparisons and make the errors larger. As evident in 1993 and particularly in the regions near the coast, there is a good agreement between the data and buoy drift.

### Ice Margin Problems

As in the previously examined case, the comparison always encounters problems (i.e. large rms differences) in cases, where buoys are close to the ice edge. Though sometimes in ice, they are often not flagged as being outside and, thus, causing high error values when included in the comparison. In these cases, the method using a search radius large enough to capture these buoys produces large errors. In Fig. 4.10, the buoys of 1993 that circumnavigated nearly half of the Antarctic continent illustrate this problem very well, since they mainly stay close to the ice edge, but not directly in the ice that can be resolved by remote sensing instruments.

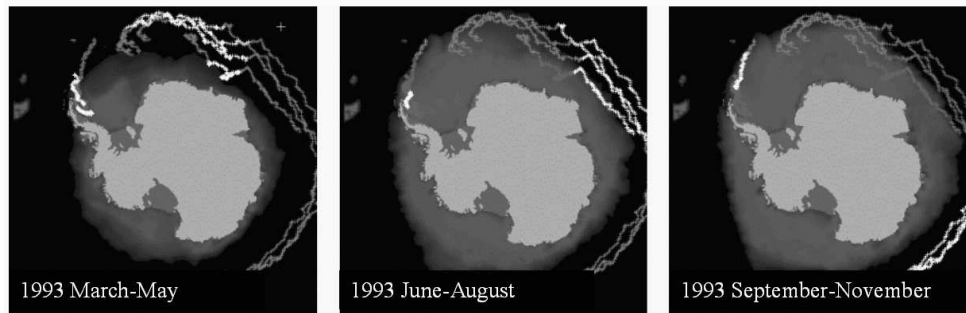


**Figure 4.10:** *Track of 1993 buoys and ice concentration for different seasons. The section of the path of the buoys during these seasons is marked in white.*

### 4.3 Conclusions regarding Validation

The main findings from this investigation were:

- The optimal interpolated OI data show smaller errors than the 85 GHz data when compared to buoys.
- Sliding means for buoy data, adapted to the time interval of the satellite data, are better for comparisons.
- Search radii around 600 km, as used in the Arctic, are appropriate for the Antarctic too, except for coastal regions with more compressed, perennial ice.
- Coastal regions generally show smaller rms errors and a positive or close-to-zero bias. Values there are not so season-dependent than in other regions.
- A general dependence on the different seasons is not clearly evident from the data. In most cases, except for the outer areas, there are decreasing errors and a smaller negative bias in the spring seasons.
- The division of the investigation areas into the parts south and north of 60°S produces great differences of the values and a very strong negative bias for the regions near the ice margin zone that are already influenced by the ACC.

This comparison clearly invalidates some former results and indicates quite conclusively that the satellite products provide a better representation of the spatio-temporal patterns of sea-ice drift when buoy data are exploited into the OI scheme. Furthermore, optimal merging of satellite and IPAB data allows to provide modellers with a dataset of practical value and with uncertainty estimates with regionally and seasonally varying values. It is clear that the satellite/buoy comparisons must be made carefully, for the correct rms differences to be found between the two datasets. Former comparisons have clearly encountered difficulties in this regard. Early point-to-point comparisons with buoys were rather crude and, under certain circumstances, gave the impression that the satellite products were actually worse than they really

are. It is a consequence of non-optimal schemes to compare the Lagrangian drift track data with an Eulerian gridded product. It should even be kept in mind that the buoy data were smoothed to the satellites temporal resolution. Hence, many of the high-frequency changes were not considered. Furthermore, the results show that the method should carefully consider the seasonal and regional uncertainties/biases due to variations of ice conditions, and of the length scale and time scale inherent to sea ice variability.

## 5 Trends in Sea Ice Motion

To assess long-term trends and interannual variability of sea ice in different regions, selected points are chosen from the database and the corresponding timeseries are analysed. Areawide availability of satellite data allows for an estimation of timeseries at various points spread over the whole area, in contrast to sparse timeseries of in-situ measurements. Hence, with this new 20-year's timeseries on ice motion it is possible to investigate whether there are significant trends and changes in the mean ice motion velocity and variability.

### 5.1 Investigation Areas

Due to the changing sea ice coverage, satellite drift data are not available continuously at all points. As mentioned in the data description (3.1), drift data cannot be calculated during summer season. Additionally, some regions have an insufficient sea ice cover for drift determination in the other months of the year. To find appropriate grid points for long-term studies, the data available for each pixel in the database were summed.

By fixing the positions of these points, it was aimed at collecting data from different oceans and sea ice regimes. This allows to evaluate simultaneous timeseries all around Antarctica. The maximum number of months with drift data is 171 for regions that are covered with sea ice around the year. However, this is only a small area in the whole database. Using the criterion that the selected spots should have drift data in 75% of the time at least, this is necessary to make comparisons for extended periods, only points closer to the continent come in to consideration (Fig. 5.1). Ice motion data from the outer sea ice regions as well as from the marginal ice zone could not be used here, since they have no sufficient temporal resolution.

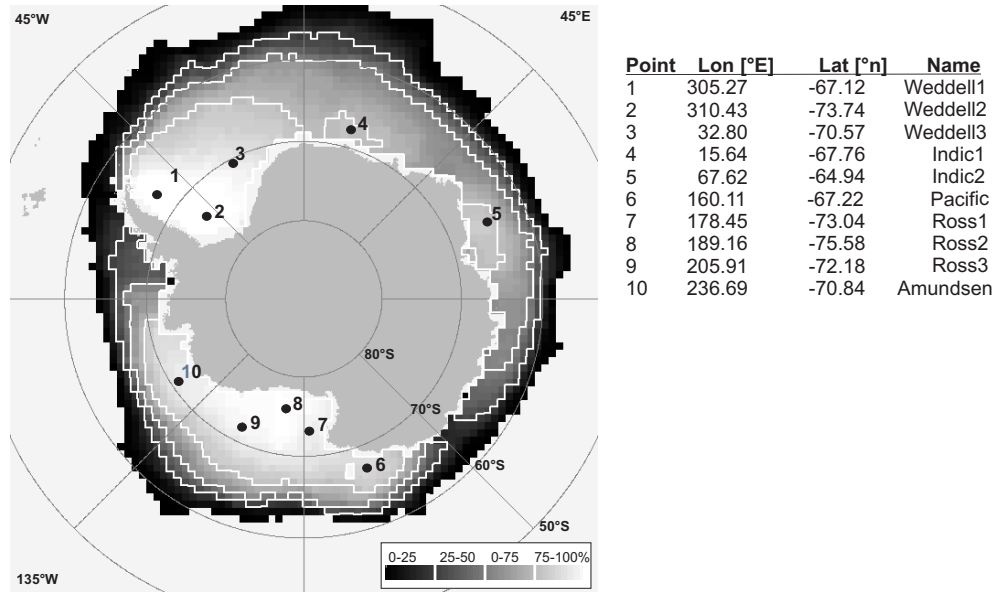


**Figure 5.1:** *Percentage of monthly mean OI-2day drift data available between 1979 and 1997, white lines indicate 25% differences. The points are chosen to be located inside the 75% concentration lines.*

Points 1 to 3 represent data from the inner Weddell Sea, with the first point being close to the Antarctic Peninsular, and point 2 and 3 being oriented along the mean streamlines of the Weddell Gyre. The coast of East Antarctica in the Indian Ocean is represented by points 4 and 5. Point 4 is situated around 15°E and point 5 is located near the Amery ice shelf. Following the coast eastwards, no more regions with enough data samples are encountered, until the areas around point 6, which is already near the northeastern edge of the Ross Sea. Within the Ross Sea, there are three more points available, covering this area from east to west. Further to the west, point 10 in the Amundsen Sea is the last one of areas with more than 75% data. Regions in the Bellingshausen Sea and the western parts of the Antarctic Peninsular could not be taken into account.

## 5.2 Mean Trends in Ice Motion and Variance

Timeseries of sea ice motion, its meridional and zonal components, and the monthly mean variance are investigated at the specified points with the aim to learn more about long-term trends of these parameters. The monthly means of the zonal and meridional velocity components  $u$  and  $v$  as well as the absolute velocity  $|\vec{v}|$  and the corresponding variance  $\sigma$  are calculated by

$$|\vec{v}| = \sqrt{u^2 + v^2} \quad \sigma = \sqrt{\sigma_u^2 + \sigma_v^2} \quad (5.1)$$

The following statistic calculations are necessary to look for significant trends in the respective timeseries.

### 5.2.1 Statistical Equations

First, the statistical values to describe characteristics and trends of sea ice motion as well as equations for linear regression and confidence estimation are introduced.

#### Linear Regression

The linear trends in section 5.3 are calculated by a linear regression of the form  $\hat{y}_i(x) = A + Bx_i$  on the ice motion parameters, with the  $x_i$  values representing the time and  $y_i$  values the ice data, such as drift velocity or variance.

The statistical values are defined and calculated as follows, taking into account  $x_i' = x_i - \bar{x}$  as deviation of the single monthly values from the temporal mean over 19 years.

$$\text{Standard Deviation} \quad s_x = \sqrt{\frac{1}{n-1} \sum x_i'^2} \quad (5.2)$$

$$\text{Variance} \quad \sigma_x = s_x^2 = \frac{1}{n-1} \sum x_i'^2 \quad (5.3)$$

$$\text{Covariance} \quad s_{xy} = \frac{1}{n-1} \sum x_i' y_i' \quad (5.4)$$

$$\text{Correlation} \quad r = r_{xy} = \frac{s_{xy}}{s_x s_y} = \frac{\sum x'_i y'_i}{\sqrt{x_i'^2} \sqrt{y_i'^2}} \quad (5.5)$$

The equations to solve to obtain the regression parameters A and B are:

$$B = \frac{s_{xy}}{s_x^2} = \frac{\sum x'_i \sum y'_i}{\sum x_i'^2} \quad (5.6)$$

$$A = \bar{y} - B\bar{x} \quad (5.7)$$

The mean trends for the single timeseries correspond to the slope B derived from all years of monthly mean data.

### Confidence Intervals for Linear Regression

Differences between the real data  $y_i(x)$  and the regression points  $\hat{y}_i(x)$  are so called *errors* or *residuals* and defined as follows:

$$\text{Residual} \quad e_i = y_i(x) - \hat{y}_i(x) \quad (5.8)$$

with a separate residual  $e_i$  for each data pair  $x_i$  and  $y_i$ .

Wilks (1995) introduces  $s_e^2$  as the *estimated residual variance* that follows from Eq. 5.2 under the assumption of the sample average of the residuals being guaranteed to be zero:

$$s_e^2 = \frac{1}{n-2} \sum e_i^2 = \frac{1}{n-2} \sum [y_i - \hat{y}(x_i)]^2 \quad (5.9)$$

where the sum of squared residuals is divided by  $n-2$ , because the estimation is carried out with the two parameters  $x$  and  $y$ .

The estimated residual variance  $s_e^2$  represents the scatter of  $y_i$  around the regression line. With increasing  $s_e^2$ , determination of the regression decreases. The slope of the regression line, e.g. the trend of the sample, always has to be judged by its scattering. Even a small trend may be significant when the stray area is small enough. The estimated residual variance is used to obtain estimates of the sampling distribution of regression coefficients. With these

values, confidence intervals for  $A$  and  $B$  around the regression line can be constructed.

For the intercept  $A$  and slope parameter  $B$ , the sampling distribution parameters are calculated according to Wilks (1995) :

$$\sigma_A = s_e \sqrt{\frac{\sum x_i^2}{n \sum (x_i - \bar{x})^2}} \quad (5.10)$$

$$\sigma_B = \frac{s_e}{\sqrt{\sum (x_i - \bar{x})^2}} = \sigma_A \frac{\sqrt{n}}{\sqrt{\sum x_i^2}} \quad (5.11)$$

The confidence intervals, to which the regression coefficients belong with an indicated probability  $P$ , can be determined by using the above definitions and the  $z_\alpha$  values from the *Student's t Distribution* according to the chosen probability  $P$ .

$$\Delta A = \pm z_\alpha \sigma_A \quad \text{and} \quad \Delta B = \pm z_\alpha \sigma_B \quad (5.12)$$

Another parameter describing the fit of a regression is the *relative explained variance*

$$B = r^2 * 100 \quad (5.13)$$

This value indicates, how much of the variance existing in the timeseries is explained by linear regression.

### 5.2.2 Ice Motion Velocity

The trends (Eqs. 5.7 and 5.6) and confidence intervals (Eqs. 5.12 and 5.13) according to the 95% significance level are calculated for the timeseries of velocity and variance at the ten points around Antarctica and presented in Figs. 5.2 through 5.5 for a quick intercomparison between the different regions. In addition, the lines of the annual means are plotted in all diagrams. The following sections show and discuss the absolute values of velocity and variance, similar graphs for the zonal and meridional components can be found in the Appendix A.4.

The confidence intervals may help judging whether the trends of variance are statistically significant. For the ten investigation points, the velocity

curves are plotted in Fig. 5.2 and Fig. 5.3. Mean and trend values as well as the relative explained variance at each point are presented in Tab. 5.1.

Point Number	19 year's Mean [cm/s]	Trend per year [cm/s]	Confidence Interval [cm/s]	Explained Variance
1	6.40	-0.15	$\pm 0.09$	8.00%
2	5.13	-0.15	$\pm 0.10$	7.56%
3	7.46	-0.20	$\pm 0.10$	10.94%
4	10.09	-0.02	$\pm 0.18$	0.03%
5	9.56	0.04	$\pm 0.16$	0.41%
6	6.04	-0.15	$\pm 0.10$	7.89%
7	8.89	0.07	$\pm 0.10$	1.79%
8	6.92	0.08	$\pm 0.09$	2.88%
9	5.39	-0.05	$\pm 0.09$	1.27%
10	4.82	-0.02	$\pm 0.10$	0.13%

**Table 5.1:** *Statistics of monthly mean drift velocity at different points.*

The mean results for ice motion velocity are summarised in Tab. 5.1. At all points, the drift velocity trend is slightly negative or close to zero, but is of no evident significance. The largest values in Tab. 5.1 come from points 1-3 in the Weddell Sea. Here, a slight decline of the velocity can be assumed, which contradicts the results of the other part of the investigation area. In the Ross and Amundsen Seas, no decrease, but even a small increase in the velocity trend can be detected at some points. Points 4 and 5 in the Indian Ocean, which showed the strongest conspicuity in the variance behaviour, also exhibit negligible trends of velocity itself.

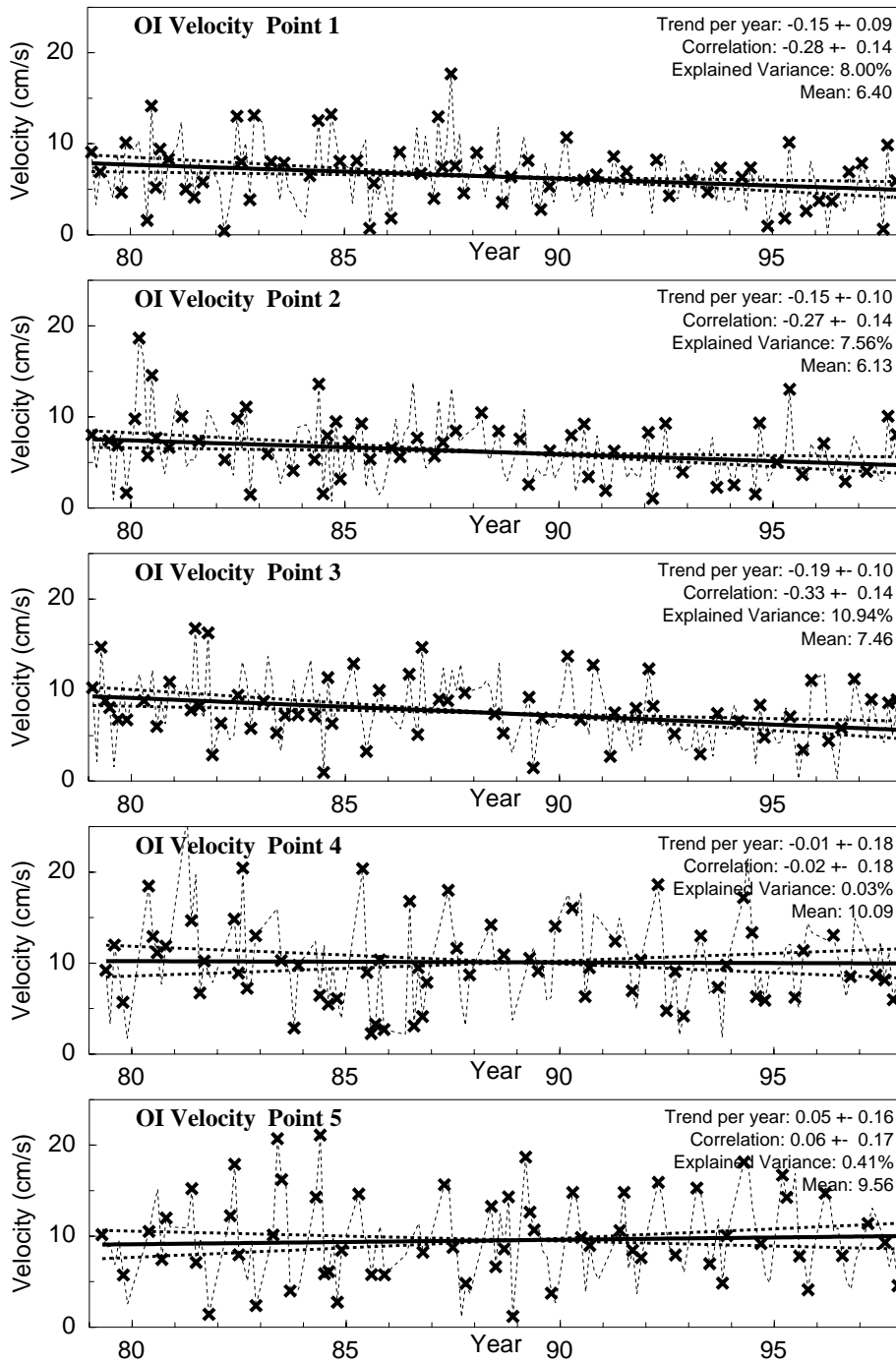


Figure 5.2: Monthly mean drift velocity at points 1 - 5. The black line indicates the mean trend with its confidence intervals as dashed lines.

The monthly mean velocity (Fig. 5.2) in the Weddell region (points 1-3) shows similar mean values and decrease. The maximum monthly mean velocities reach 15 to 18 cm/s. From the general clockwise rotation pattern in this area, it is expected that the fluctuations at point 2 precede those at point 1. Interannual fluctuations are various, with one or two velocity peaks in the beginning and middle of the year in most of the cases. Towards the end of each year, the velocity generally decreases. Superposed larger structures, such as a general increase of the velocity, appear in the years 1986 and 1987 at all three points. With the barrier of the Antarctic peninsular blocking westward drift, a positive (northward) meridional component is predominant (see Appendix A.4).

On the eastern side of the Weddell Sea (point 3), slightly higher drift values occur, but also a stronger average decrease per year. Here, the main velocity contribution comes from a negative (westward) zonal drift component. In general, the velocity values at the end of the examination period are smaller than at the beginning, which leads to these negative trends of -0.15 to -0.20 cm/s per year.

At the coast of East Antarctica in the Indian Ocean (point 4 and 5), the largest drift velocities, up to 25 cm/s, occur. An annual cycle with high values shortly before the middle of the year and small velocities at the beginning and end is evident nearly every year. Due to these yearly fluctuations, the annual mean values are only slightly higher than in the other regions without a significant trend. Due to the position in the East Wind Drift Zone, a negative zonal component contributes most to the drift values.

In literature (Heil et al. (2001), Emery et al. (1997)), another clockwise gyre in the ice motion field is documented in the area of the Amery Ice Shelf (point 5). It is supposed to manifest itself by higher positive meridional components at this point. This is not evident from the summation of the mean winter OI-data (Fig. 2.1). A positive difference between the meridional velocity at point 5 and to point 4 is visible in the last years of the investigation period only.

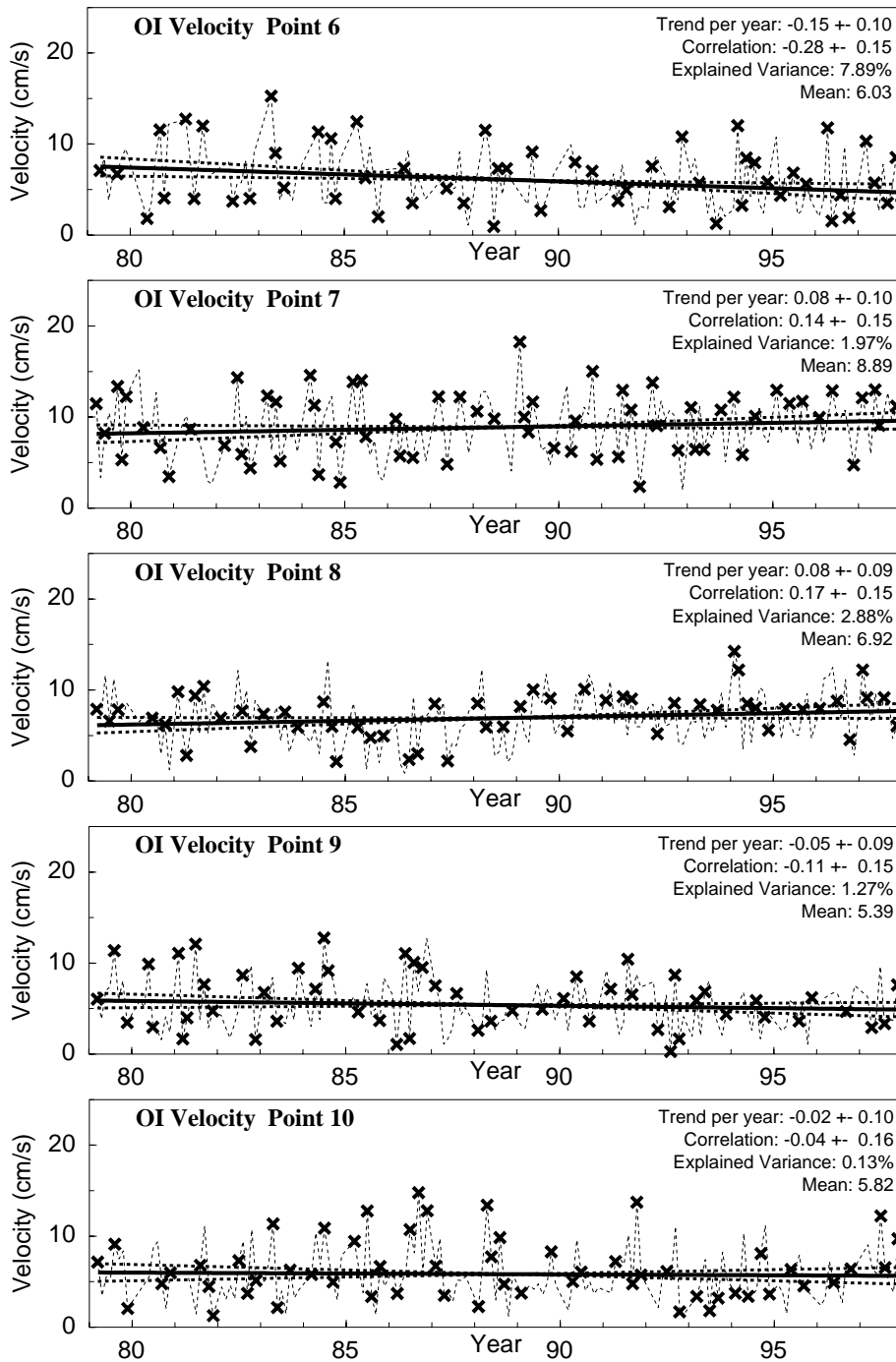


Figure 5.3: Monthly mean drift velocity at points 6 - 10. The black line indicates the mean trend with its confidence intervals as dashed lines.

In the marginal ice zone of the eastern Ross Sea and the Pacific Ocean (point 6), eastward drift is prevailing. Therefore, the main velocity contribution here comes from the negative zonal component. A velocity pattern similar to that of the points before, with an annual maximum velocity in winter, appears in the first half of the investigated period only. After 1990, there are numerous, smaller peaks per year, thus, indicating a generally changed drift pattern. Average values and the slightly negative trend have the same magnitude as in the Weddell Sea.

In the Ross Sea (point 7 through 9), the average trend is close to zero or slightly positive, in contrast to the Weddell Sea. At the eastern coast (point 7), velocity shows obvious annual cycles and a dominant northward component similar to points 4 and 5. In the central Ross Sea (points 8 and 9), a number of peaks occur per year, with point 8 having more contribution from the negative zonal drift component along the western Ross coast, while in point 9 westward components are encountered already.

Velocity patterns in the Amundsen Sea around point 10 are similar as those of point 9, also with the higher annual means in 1984, 1986, and 1991. The meridional velocity component is smaller already, with more westward drift contribution from the Antarctic Circumpolar Current ACC.

### 5.2.3 Ice Motion Variance

The monthly variance of drift velocity is discussed as a measure of the variability over the months, related to e.g. synoptic-scale atmospheric forcing. Timeseries of monthly mean variance are calculated and further treated as in section 5.2.2.

Point Number	19 year's Mean [cm <sup>2</sup> /s <sup>2</sup> ]	Trend per year [cm <sup>2</sup> /s <sup>2</sup> ]	Confidence Interval [cm <sup>2</sup> /s <sup>2</sup> ]	Explained Variance
1	115.14	-6.67	± 2.10	25.29%
2	105.61	-5.70	± 1.89	23.43%
3	174.30	-8.44	± 2.70	25.69%
4	252.69	-15.68	± 4.16	39.38 %
5	182.93	-10.00	± 3.70	23.60%
6	138.02	-6.76	± 2.68	20.65%
7	124.88	-4.86	± 1.67	23.09 %
8	115.31	-3.36	± 2.12	8.03%
9	149.33	-2.36	± 1.99	4.74%
10	143.37	-0.31	± 2.30	0.06%

**Table 5.2:** *Statistics of monthly mean drift variance at different points.*

A significant decrease of drift variance (Tab. 5.2) is found for all locations throughout the period from 1979 to 1997. It is evident that, starting in the early 1990s, the variability of monthly variances decreases significantly (Fig. 5.4 and Fig. 5.5). This means that the differences of drift velocity variances within different months and seasons vary much less than in the decade before. The plots are based on the 2day data, but a comparison with the variance of 1day data, existing after 1992, shows that the curves are very similar. Therefore it may be concluded that this decrease is not caused by a different sampling interval.

In the inner Weddell region (points 1-3), variance decreases by about 6 to  $8.5 \text{ cm}^2/\text{s}^2/\text{year}$ , with the strongest effect in the eastern Weddell. The corresponding confidence intervals are around  $\pm 2 \text{ cm}^2/\text{s}^2$ , with the higher values belonging to the stronger decrease. Hence, a significant negative trend of sea ice motion variance can be established for the Weddell region. Around 25% of the timeseries variability there can be explained by linear regression.

In the coastal regions of the Indian Ocean (points 4 and 5), the strongest variance decline takes place. This is reflected by the decrease rates of 10 to  $16 \text{ cm}^2/\text{s}^2$  at points 4 and 5. With the confidence intervals staying around  $2 \text{ cm}^2/\text{s}^2$ , the negative trend is significant, too. In the regions around  $10^\circ$  to  $20^\circ$  East (point 4), where the strongest negative trend is located, linear regression explains nearly 40% of the variability.

Trends per year and confidence intervals similar to those in the Weddell region appear in the Pacific Ocean (point 6) and in the northeastern part of the Ross Sea (point 7). The trend in this region of the Ross Sea is smaller than at the points of lower longitude, but with a small confidence interval it is still significant. The relative explained variance ranges from 20% to 23%.

In the central Ross Sea (points 8 and 9) and in the Amundsen Sea (point 10), trend values become very small and the confidence intervals show no significant negative trend can be derived for these points.

The reasons of the decreasing drift variance observed in the different regions around Antarctica shall be analysed below. The negative sea ice trends will be studied carefully for artificial reasons before comparing them with atmospheric variabilities.

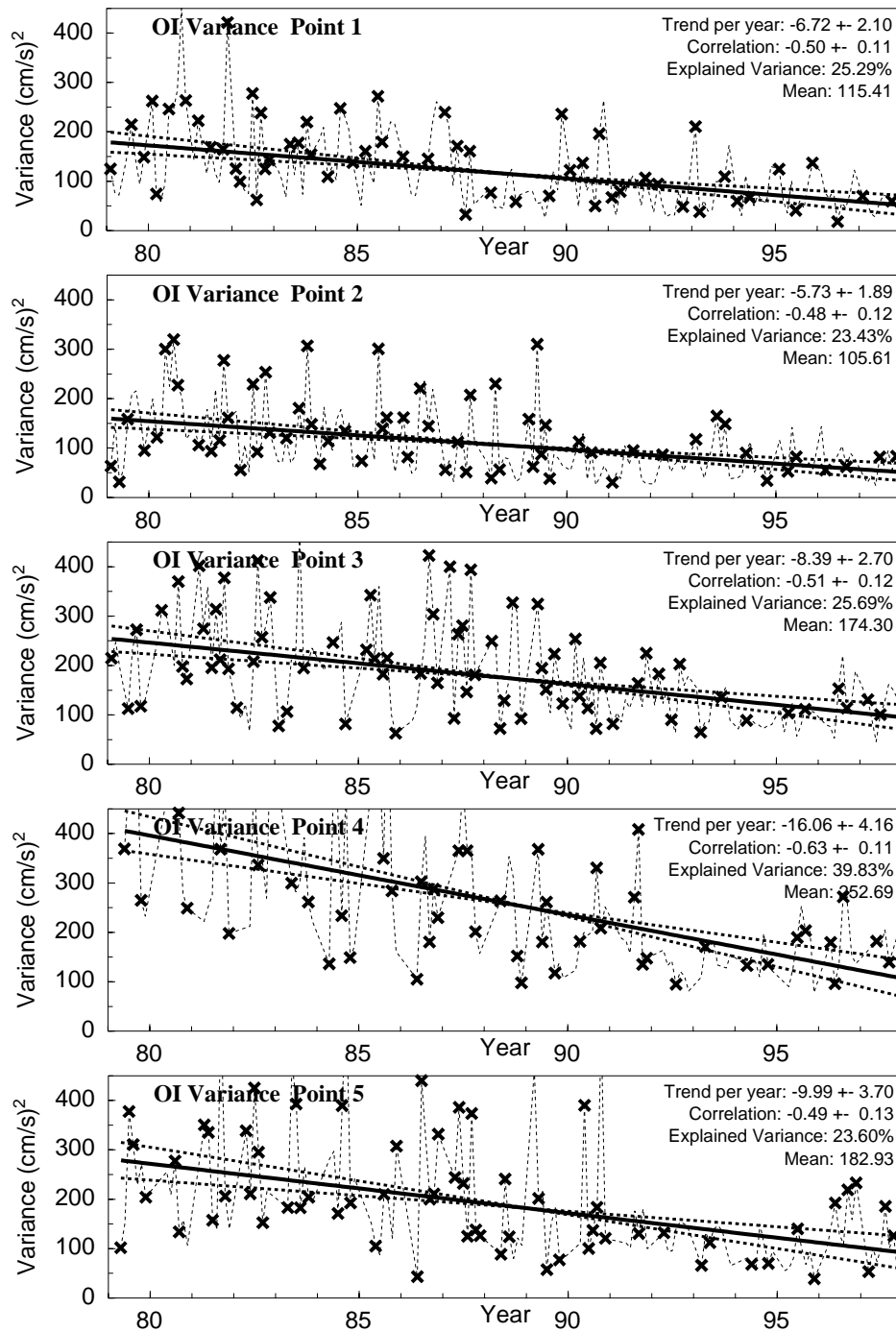


Figure 5.4: Monthly mean drift variance at points 1 - 5. The black line indicates the mean trend with its confidence intervals as dashed lines.

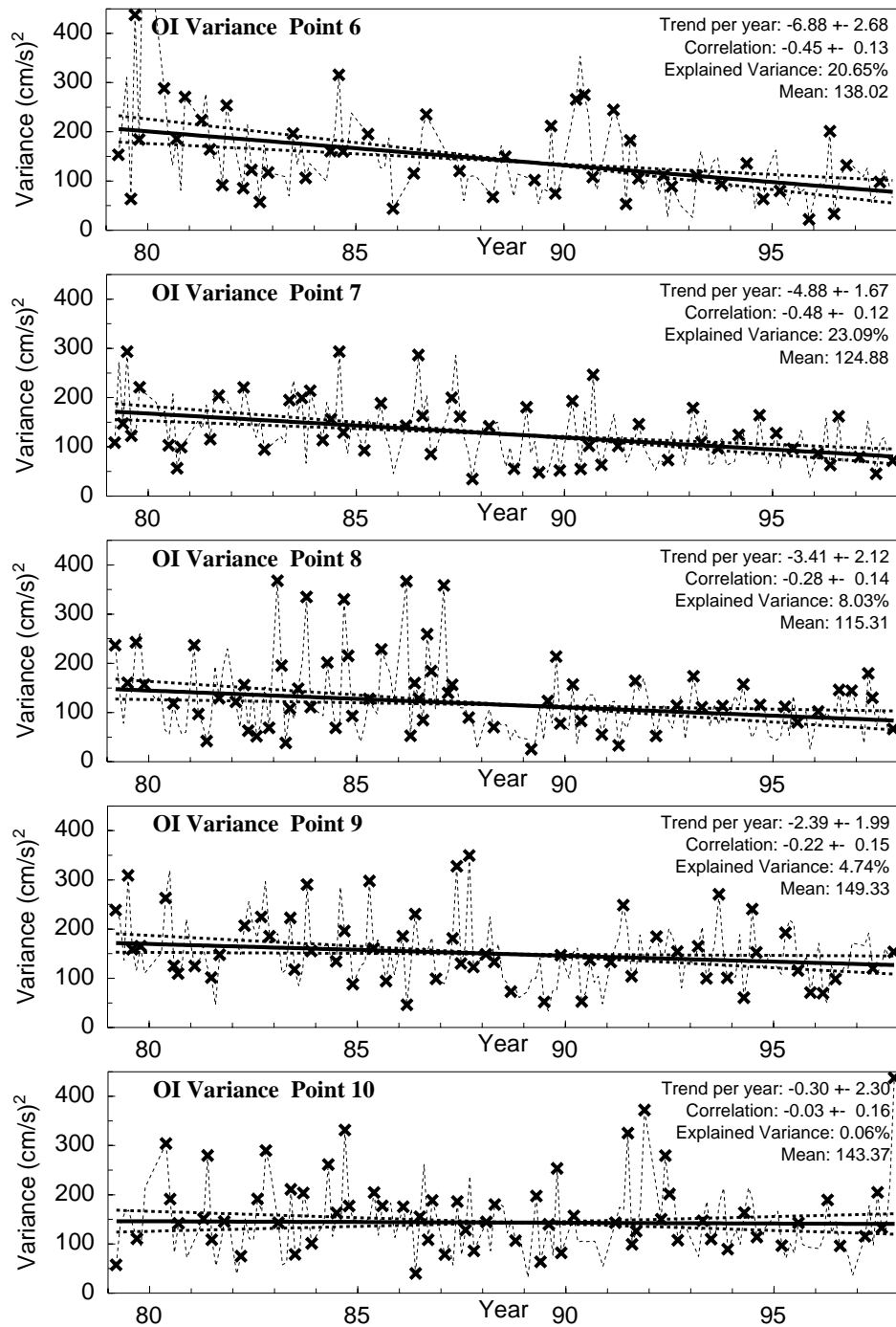


Figure 5.5: Monthly mean drift variance at points 6 - 10. The black line indicates the mean trend with its confidence intervals as dashed lines.

## 5.3 Decreasing Variance in OI Data

The composition of the *Optimal Interpolated* ice motion data is investigated in detail with the purpose to find out whether the decrease in ice motion variance may be caused by artefacts introduced by the algorithm for ice motion calculation.

The first thing to consider is the fact that the OI drift is composed of data from different sources, that is the 37 GHz and the 85 GHz channel as well as auxiliary buoy data. The basic data available for all the years come from the 37 GHz channel, whereas 85 GHz data have been included after 1992 only. It has to be checked whether the combination with other channels or buoy data has a smoothing effect on the ice motion variance.

The second influence that cannot be ignored originates from the different sensors of SSMI, which were in use during the data period.

### 5.3.1 Influence of Buoy Data on the OI Algorithm

Use of the OI algorithm might lead to the assumption of the smoothing effect of the inclusion of buoy data explaining the decrease of variance in periods when buoy data could be added.

Admittedly, the buoy data set included in the calculation of OI data is much smaller than the total amount of buoys from 1985 to 1998. Buoy data included in the algorithm mainly come from the Weddell Sea and the surrounding areas (Fig. 5.8), but this also in the period before 1992, when the strong variance decrease appeared at most of the points. Moreover, the variance decrease can also be observed at locations where no buoy data have been included for the whole period. Thus, it can be excluded, that the influence of buoy data on the OI algorithm leads to an artificial change of variance.

### 5.3.2 Influence of Differences in 37 GHz and 85 GHz Channel Data

In the complete OI dataset, 85 GHz data have been included since 1992. However, a sudden break exactly at 1991/1992 (Fig. 5.4) is not evident,

instead it occurs at different times along the ten investigation locations. To judge whether this abrupt decrease is an artefact, the dataset can be checked by comparison with 37 GHz ice motion data for the same period.

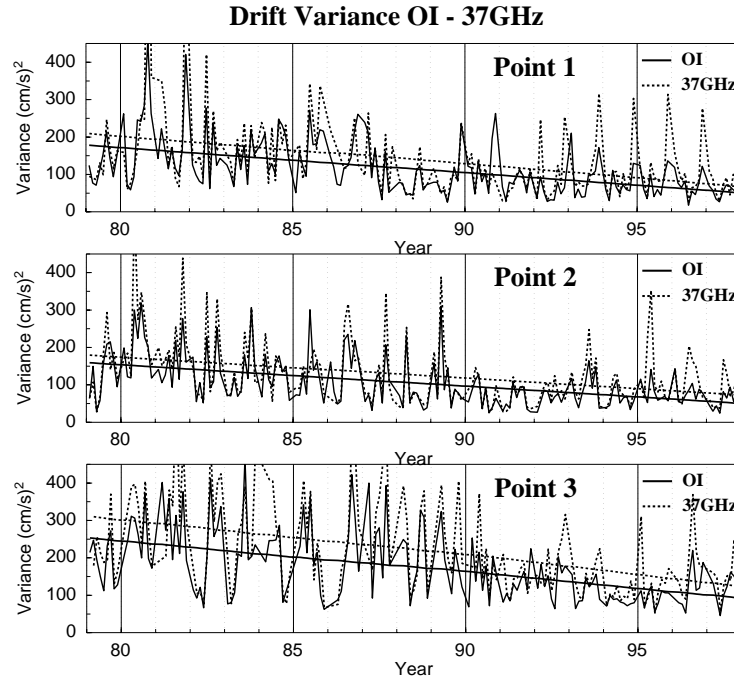


**Figure 5.6:** Comparison of OI (solid lines) and 37 GHz (dashed lines) variance, monthly values and trend.

The prevailing variance trend is negative in the 37 GHz dataset, too. The average values are higher by about  $30 \text{ cm}^2/\text{s}^2$  than in the OI data, but the rates of decrease are nearly similar. In general, the higher values of 37 GHz variance in Fig. 5.6 can be explained from the already higher velocity values (Fig. 5.7) in this dataset as compared to the OI data which have already undergone the optimal interpolation that causes a smoothing effect.

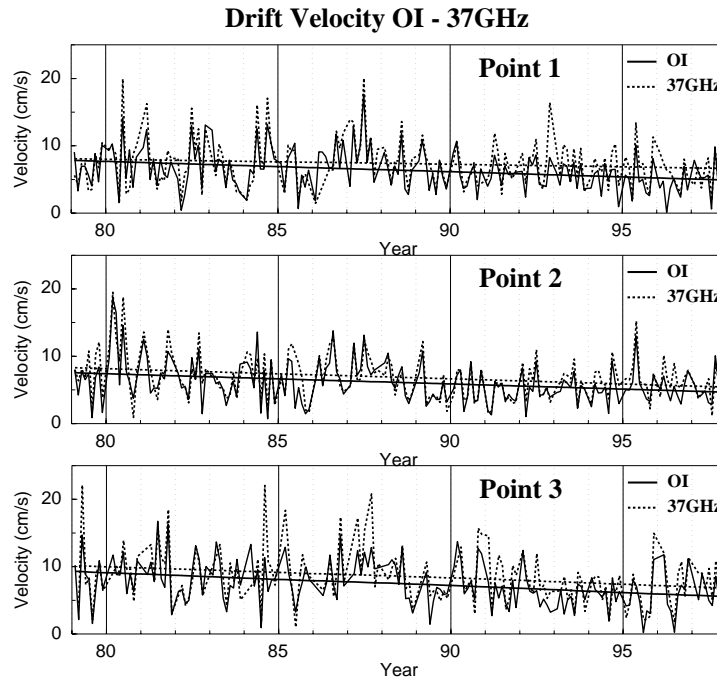


**Figure 5.7:** Comparison of OI (solid lines) and 37 GHz (dashed lines) drift, monthly values and trend.

Smoothing does not only result from the OI scheme itself, but also from the larger OI grid spacing and the fact that correlation length scales are respected in the OI method. The result shows that the OI scheme is consistently lower and smoother in both drift speed and drift speed variance.

A striking difference between the two data sets remains: In the OI data, not only the mean variance values are decreasing, but also the amplitudes of the variance (Fig. 5.6). In contrast to the merged data from both channels, 37 GHz values alone still show high amplitudes in the later years.

High amplitudes are observed mostly for months at the beginning or end of the sea ice season. In-between, the fluctuations are quite similar. Hence, it is assumed that the peaks are caused by wrong captured high drift values in the 37 GHz data. These values are better represented in the OI, which benefits from the additional sources of 85 GHz and buoy data.

Moreover, the 85 GHz data in comparison to 37 GHz-only data are supposed to increase the potential of capturing variance - despite the smoothing discussed above. This is simply because the resolving power of the instrument is greater and generally, more variability is captured in the drift field, the higher the resolution is.

### 5.3.3 Influence of different Satellite Sensors

To investigate whether the different satellites/sensors have an impact on the observed decrease in variance and velocity, the timeseries are divided into short periods according to the operation times of the satellite sensors. The SMMR period lasts from 1979 to June 1987. For the later SSMI, the periods are listed in the following table:

SSMI Period	From	To
F08	July 1987	December 1991
F10	January 1991	November 1997
F11	January 1992	May 2000
F13	May 1995	present
F14	May 1997	present
F15	December 1999	present

**Table 5.3:** *SSMI periods, from Remote Sensing Systems, according to [www.ssmi.com/ssmi/ssmi\\_description.html](http://www.ssmi.com/ssmi/ssmi_description.html) .*

**Optimal interpolated** data exist from 1979 to 1997 consequently there are seven periods for intercomparison:

- **19a:** The complete 19-year dataset
- **SMMR:** 3/1979 to 6/1987
- **37 GHz:** 1997 to 1992, when the 85 GHz channel was not yet available
- **SSMI:** 7/1987 to 11/79 with the subsections F08, F10, and F11

For each of these periods, the mean values of variance and the trend per year are calculated.

### Mean Variance for Different Periods

Mean variance results given in Tab. 5.4 may be summarised as follows: The main difference in variance decrease is between the periods of SMMR and SSMI, divided into a strong decrease of variance at the points 1-6 and a smaller decrease in the Ross Sea (points 8-10).

Point	19a	SMMR	37 GHz	SSMI	F08	F10	F11
1	115.41	160.43	136.19	79.02	90.13	71.91	70.78
2	105.61	139.50	120.60	78.21	84.68	71.47	73.41
3	174.30	221.11	204.62	138.01	173.86	114.89	112.50
4	252.69	352.40	304.17	185.78	229.65	160.59	152.12
5	182.93	248.23	220.77	136.88	173.56	113.84	111.37
6	138.02	179.35	163.90	111.41	138.47	102.55	94.06
7	124.88	158.57	139.66	100.34	107.16	97.71	95.31
8	115.31	144.83	125.13	92.94	90.53	97.08	94.77
9	149.33	166.44	152.09	135.60	125.92	146.32	143.19
10	143.37	147.48	144.51	140.16	139.05	148.87	140.98

**Table 5.4:** Mean drift variance in  $cm^2/s^2$  for different satellite periods, at the points outlined in Fig. 5.1.

Generally, the mean variance in the central Weddell Sea (points 1 and 2) and the central Ross Sea (points 7 and 8) is much smaller than at the other points for all averaging periods.

Within the total SSMI period, the smaller sections of F08, F10, and F11 also show differences. Compared to the whole period, the velocities in the F08 period are larger at points 1-7. At the other points, they stay quite similar. Generally, the F10 and F11 period do not show any big difference, since they only differ for one year. Differences between F08 and F10/F11 are most obvious at points 1-6. They become smaller at points 7 and 8 and disappear at the last points.

A strong influence of the later available 85 GHz channel can be excluded, since periods with 85 GHz data (after 1992) do not exhibit any sudden change compared to the data before. From Tab. 5.4 it may be assumed that the difference between SMMR and SSMI only could lead to this decrease in variance. On the other hand, however, it should be considered that this is only effective in at points in the Weddell Sea and East Antarctica and not in the whole dataset.

### **Trend per Year**

In analogy to the variance mean values, the trend per year is calculated for each of the different satellite seasons for intercomparison (Tab. 5.5), with the result being as follows:

Similar to the mean values from Tab. 5.4, variance decreases in the whole 19-year's period, with largest negative trends in the Weddell Sea and the Indian Ocean (points 1-6 ) and smaller but still negative trends at the other places. For the years after 1987, the SSMI period reveals a similar behaviour. The points with a small negative trend in 19 years (points 8-10) show slightly positive values. Compared to the total 19 years, the SSMI period generally shows a weaker decrease.

Point	19a	SMMR	37 GHz	SSMI	F08	F10	F11
1	-6.67	0.31	-6.85	-2.21	7.88	-1.22	-0.84
2	-5.70	-5.04	-7.66	-2.87	-13.73	0.67	-1.19
3	-8.44	-1.64	-6.47	-10.66	-25.64	-2.37	-1.60
4	-15.68	-13.25	-17.92	-10.91	-24.72	0.33	10.11
5	-10.00	1.61	-7.71	-8.71	-4.49	-1.41	0.57
6	-6.76	-10.54	-6.23	-4.63	16.63	-5.88	1.10
7	-4.86	-1.24	-5.67	-1.62	2.49	-2.40	-0.92
8	-3.36	4.91	-3.93	1.27	10.79	-2.10	-1.04
9	-2.36	-2.20	-4.90	1.34	-1.29	-5.60	-5.27
10	-0.31	1.11	-0.08	0.90	11.33	-6.27	-1.34

**Table 5.5:** *Average variance trend [ $cm^2/s^2/year$ ] for different satellite periods.*

This allows the conclusion to be drawn, that the main negative values come from the previous SMMR period. For this period, as well as for the single periods of F08, F10 and F11, values vary strongly between the different regions and seasons and do not allow for any clear assumptions of the variance trend.

## 5.4 Trends from Buoy Data

To find out, whether the discussed decrease in variance is obvious in other ice drift data, too, comparisons of data obtained at the single points with the whole buoy dataset are performed. From Fig. 5.8 it is obvious that there are too few buoy data close to the OI points to derive reliable trends for different satellite periods. Due to the different distribution of buoy measurements

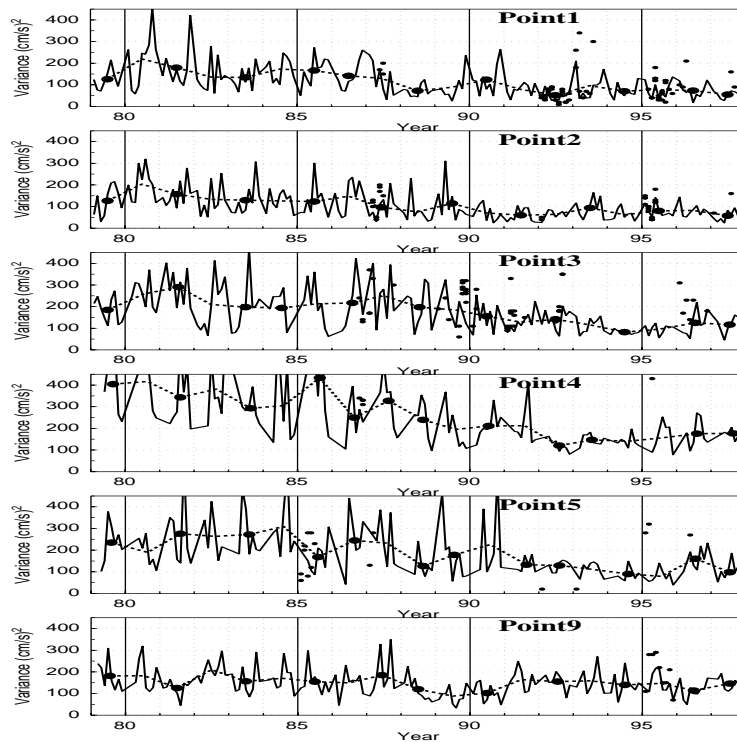


**Figure 5.8:** OI variance in  $\text{cm}^2/\text{s}^2$  from 1979 to 1997 (solid) and annual mean (dashed), buoys (dots).

around Antarctica, as discussed in 4.2, comparisons cannot be made for the whole Antarctic sea ice zone. Instead, buoys from the Weddell Sea area that makes up the main part of the investigations are chosen, since the most significant decrease in variance happens there. In order to reach the same temporal resolution as the satellite data, daily mean buoy drift is calculated, and from this, the monthly mean velocity and variance. These values may

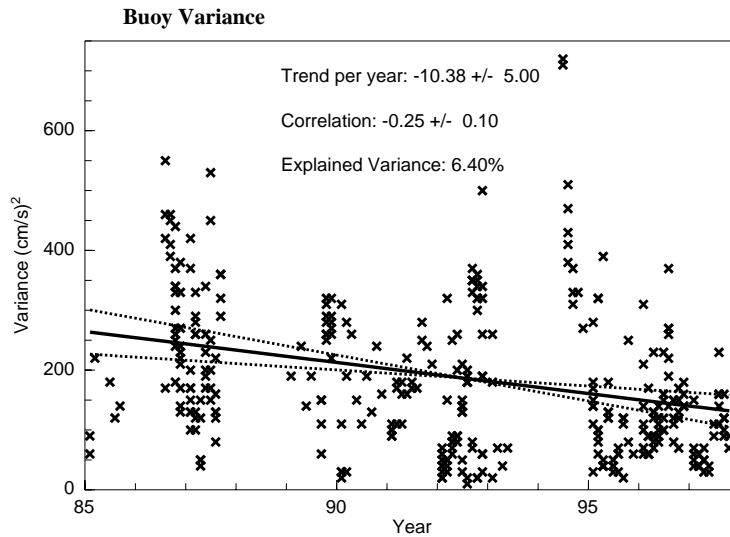


**Figure 5.9:** Monthly mean buoy variance (dots for single buoys, solid line gives the 15-year's trend, dashed lines show the confidence intervals).

be compared to timeseries at points 1-3 in this area.

The maximum monthly speed variances from buoy data (Fig. 5.9) of  $650 \text{ cm}^2/\text{s}^2$  exceed those from SSMI data by about 30%. This reflects a generally smoothing effect in the satellite-based drift estimates.

Apart from several extremely high values which mainly exist in 1987 and 1993/94 and come from buoys near the ice margin, as discussed in chapter 4, a decreasing variance trend in the Weddell region can be observed for buoy data, too. The mean trend per year for this timeseries is about  $-18 \text{ cm}^2/\text{s}^2$ . This is larger than the mean trend of satellite data, but it must be taken into account that this timeseries is not based on a temporally and regionally homogeneous dataset as the satellite data. The strong variability of monthly buoy data also causes the trend to be statistically uncertain.

To overcome this problem and check how ice drift velocity and variance develop and whether sensor-dependent differences exist, the regional average values and trends are taken from the region around points 1-3 (Weddell

<b>Period</b>	<b>Total</b> Trend/Mean	<b>F08</b> Trend/Mean	<b>F10</b> Trend/Mean	<b>F11</b> Trend/Mean
<b>OI</b>	-0,29 / 6,15	-0,9 / 6,61	-0,02 / 5,45	-0,02 / 5,40
<b>37 GHz</b>	-0,24 / 7,28	-0,96 / 7,46	-0,05 / 6,76	-0,14 / 6,81
<b>Buoy</b>	-0,22 / 5,93	-1,05 / 6,11	-0,09 / 5,47	-0,20 / 5,54

**Table 5.6:** *Velocity trend per year/mean velocity (cm/s) for different periods for Weddell region (0°-60° W/Points 1-3).*

region), where OI data, 37 GHz data and buoy data, are available at the same time. Then, the trend per year and the period's mean value are calculated for each dataset and the total period of incident datasets as well as for the different satellite periods (from Tab. 5.3).

Concerning velocity trends, the following conclusions may be drawn from Tab. 5.6:

For the total period, all three observation systems show a similar negative velocity trend, which is represented by the values on the left hand sides of the columns. The highest velocities are measured in the 37 GHz data, followed by OI, and buoys. This effect is also obvious from the buoy-satellite comparison (Chapter 4), where, in contrast to the whole area, the drift in the coastal regions of the Weddell Sea is slightly overestimated by the satellite. As in the general investigations, the F08 period shows the strongest decrease and the highest mean values for all observation systems, leading to the conclusion that general changes in ice motion regimes took place in these years. In contrast to this, F10/F11 show clearly reduced negative trends and the smallest mean velocities with no big differences between F10 and F11 (which only differ for 1 year of data).

Apart from their systematic difference, the distribution of mean values is similar for the different periods, especially for the two satellite datasets. In buoy data, the decrease of the mean values is weaker than in satellite data, but the trend is stronger negative.

Period	Total Trend/Mean	F08 Trend/Mean	F10 Trend/Mean	F11 Trend/Mean
<b>OI</b>	-7.30 / 109.86	-10.05 / 114.74	-1.17 / 85.79	-1.43 / 85.25
<b>37 GHz</b>	-4.41 / 128.33	-16.27 / 133.44	-2.14 / 115.38	-1.14 / 119.20
<b>Buoy</b>	-9.25 / 171.50	-22.39 / 199.13	-8.94 / 155.56	-11.91 / 154.73

**Table 5.7:** Variance trend per year/mean variance ( $cm^2/s^2$ ) for different periods in the Weddell region ( $0^\circ$ - $60^\circ$  W/points 1-3).

The mean values and trends of drift variance are summarised in Tab. 5.7. When looking at the variance trend per year for the total period from 1986 to 1997, all three observation systems have negative values, with the smallest ones found in the 37 GHz data. The mean variance reaches its largest values in buoy data that differ by  $70\text{ cm}^2/s^2$  from OI and by  $50\text{ cm}^2/s^2$  from 37 GHz data. The comparison between the different periods reveals that the F08 period shows the strongest decrease and the highest mean variances for all measurements, the same as in the velocity data from Tab. 5.6. The F10/F11 period shows a smaller negative trend and smallest mean values for both satellite datasets, with no big difference between F10 and F11. In comparison to OI, the 37 GHz mean value for F10/F11 is not so much reduced. 37 GHz generally shows higher mean values and not so strong changes between the periods. The variance trend in buoy data differs strongly for the F10/F11 periods compared to the satellite data, while the behaviour of mean variances itself is similar.

Generally, a negative trend of ice motion velocity and variance is detected independently of the different measurement systems. The period with highest values and strongest negative trend is 1987-1991 (F08). Higher means exist in the preceding SMMR period which is not included in this comparison due to lack of buoy data. Since only 37 GHz data is available in this period, the differences in Fig. 5.6 in the years from 1979 to 1987 only may be compared.

## 5.5 Conclusions from Trend Analysis

Trend analysis for ice motion and variance shows negative trends for most of the regions. Based on the previous investigations, it may be stated that the influences of the OI algorithm or smoothing by the inclusion of buoy data on the decreasing variance can be neglected.

The same holds for the comparison of different SSMI sensors. The only striking difference comes from the two different periods of SMMR and SSMI. Here, mean variance values become smaller in the second decade at all points, with the strongest effect in the Weddell Sea and Indian Ocean and smaller ones in the Ross and Bellingshausen/Amundsen Seas. Similar differences for the two main periods have also been reported by Watkins and Simmonds (2000). They studied anomalies and trends of SIC, SIE and SIA and compared them for the two periods. They found a decreasing trend of SIE and SIA for the SMMR period, and a significantly positive one during the SSMI measurements, resulting in smaller overall positive trend for the whole time-series. The opposite behaviour is exhibited by sea ice concentration. It shows an increasing trend for SSMI and a reduction for SMMR. Unfortunately, the velocity trends in the inner pack regions, where our investigation points are located, do not directly refer to the above-mentioned parameters of SIE and SIA, the changes of which influence the outer ice regions more. A decreasing ice concentration in the SMMR period would allow for higher ice velocities, since there are less moving restrictions than with higher ice concentration. This may explain the higher ice motion velocities for this period in Tab. 5.4. Consistent with these observations is the reduction of mean ice velocity in the SSMI period with increasing ice concentration trend.

Previous investigations at selected points revealed a significantly negative trend of ice motion variance in the Weddell Sea and the adjacent coastal parts of the Indian Ocean. Further eastwards, the trend becomes less significant. In parts of the Ross Sea and the Amundsen Sea, the effect vanishes. The spatial distribution of the trend for the whole area is given in Fig. 5.10. This overview shows a dipole pattern with stronger negative trend values in the eastern Weddell Sea and East Antarctica and smaller negative up to positive

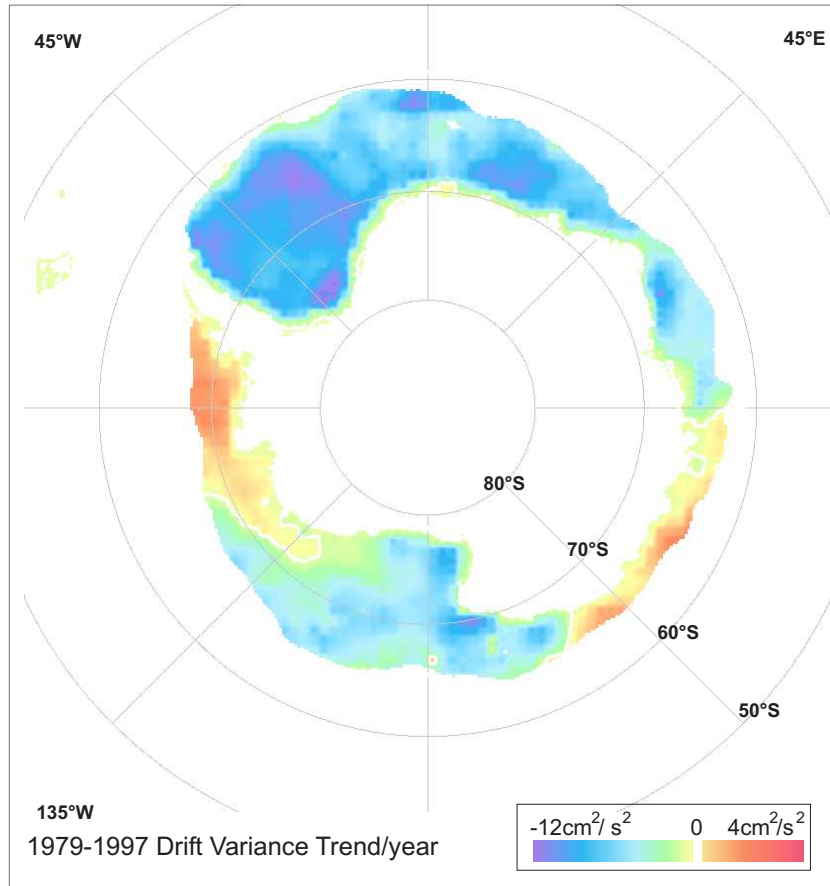


**Figure 5.10:** *Ice motion variance trend per year. White isolines show the separation between positive and negative trends.*

values in the Ross and Bellingshausen/Amundsen Seas.

The congeneric map for the trend of ice drift velocity (Fig. 5.11) shows a similar regional distribution, but with smaller negative or even positive trends and a finer partition of regions with different trend values. The areas with a positive trend around 0°E to 80° E indicate that trends of velocity and its variance are not always positively correlated. The striking area with strongly positive drift trends around 135°E suffers from poor data availability (also Fig. 5.1) and is uncertain.

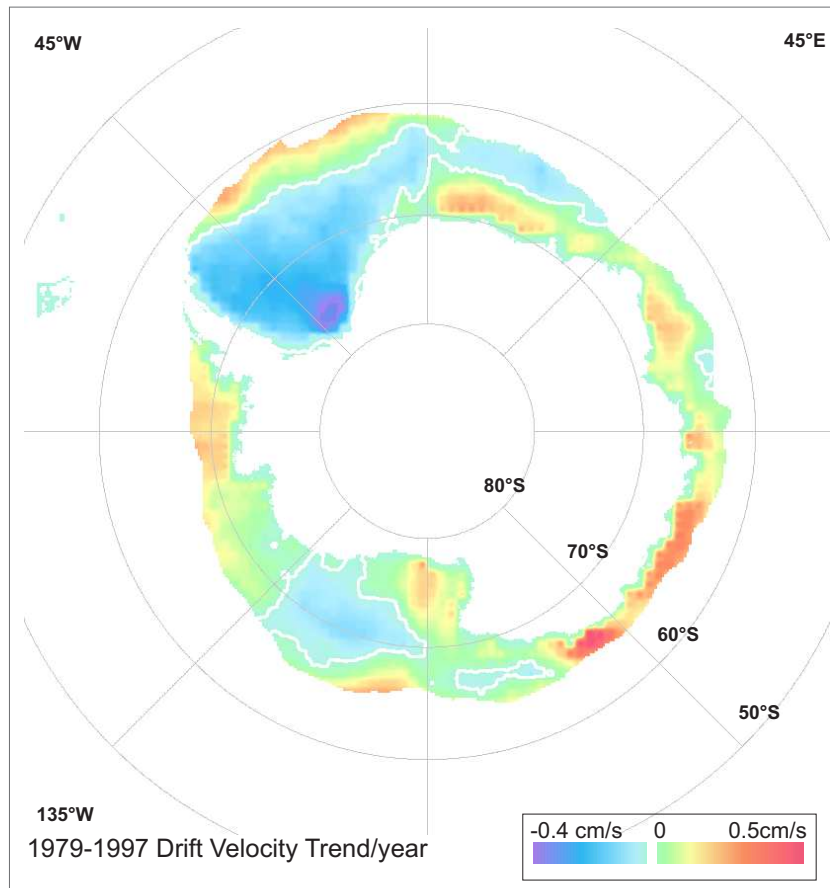


**Figure 5.11:** *Ice motion velocity trend per year. White isolines show the separation between positive and negative trends.*

The drift speed results indicate that Weddell Sea ice appears to have slowed down over the last 19 years. In this respect, the pole of greatest slowing-down in the southernmost Weddell Sea near the Filchner ice shelf front is of significance. Indeed, grounded icebergs in the vicinity of Berkner island had an impact on regional drift by pinning sea ice in this location and creating a fast ice barrier that retarded circulation in the southern part of the basin. Importantly the Weddell Sea and eastern Ross Seas exhibit the same trend, whereas the West Antarctic peninsula area and large parts of East Antarctica exhibit an increase in velocity.

From synoptic investigation, it is obvious that in the Weddell Sea, where

most of the significant variance decrease occurs, the general variance is caused by storm forcing and the superimposed mean synoptic pattern.

In Simmonds et al. (2003), the authors claim that the number of cyclones over the satellite era (January 1979 to February 2000) has been decreasing: The counts of cyclones in the 21st year of NCEP analyses show negative trends over most of the subantarctic region. At the same time, however, the annual mean cyclone intensity, radius, and depth exhibit increases. They also state that the high southern latitude cyclone system density is greatest in the Indian Ocean and south of Australia near, or to the south of,  $60^{\circ}\text{S}$ . The numbers in winter exceed those in summer, except for a few, but important regions such as the Bellingshausen Sea. The Antarctic coastal region is confirmed to be of high cyclonicity, as is the northern part of the Antarctic Peninsula and over and north of the Drake Passage. Cyclolysis is much more confined to the near-coastal region. The mean intensity, radius, and depth of subantarctic cyclones assume their largest values near  $60^{\circ}\text{S}$ . This is also consistent with the observation of greatest drift variance in the records for points 4 and 5 as well as with the strongest negative trend at point 4. This leads to the assumption of a general relation between the distribution of cyclones and the ice motion variance.

---

## 6 Modes of Interannual Variability of Sea Ice Motion

The relationship between atmospheric parameters and sea ice on scales beyond 1 year has been subject of various studies in recent years. They focused mainly on connections between ice drift dynamics and meteorological forcing as well as on relations between changing sea ice concentration and anomalies in the atmosphere and ocean.

The following examination relates variability of atmospheric parameters on different scales to anomalies of sea ice data. In contrast to the more common use of sea ice concentration and extent, the additional use of sea ice motion data brings further advantages and allows to learn more on the nature of these anomalies. Ice concentration alone cannot reflect a clear response to forcing modes due to annual configuration. Examinations of concentration anomalies are restricted, since after reaching 100% concentration, further accumulation of ice results in an ice thickness increase which cannot be measured homogeneously nowadays. Comparison of variations of sea ice extent is always reduced to the area of the sea ice edge. Thus, sea ice motion data are a valuable parameter, since information on its magnitude and its variability are available for the whole sea ice region.

### 6.1 Coupled Modes of Variability

The relation between interannual changes of sea ice parameters and the different atmospheric modes of variability, such as the Southern Annular Mode (SAM), the Southern Oscillation Index (SOI), and the Antarctic Circumpolar Wave (ACW) is documented by various investigations (White and Peterson (1996), Yuan and Martinson (2001), Drinkwater and Venegas (2001)).

These different modes have already been introduced in section 2.2.1. Below, the general configuration of these modes shall be investigated to find out whether a relation to sea ice motion can be established. Selected time-series reflecting SAM and SOI (Kwok and Comiso, 2002b) are shown in Fig.

6.1. The SAM (panel a) shows a clear positive trend that superposes its annular configuration. In contrast to this, the SOI (panel b) has irregular variations, but a negative bias. The strongly negative peaks come from the ELNino events in 1983, 1987, 1992, and 1997. Positive peaks are associated with the opposite pressure pattern during LaNina events and evident for the years 1989, 1996 and 1999.

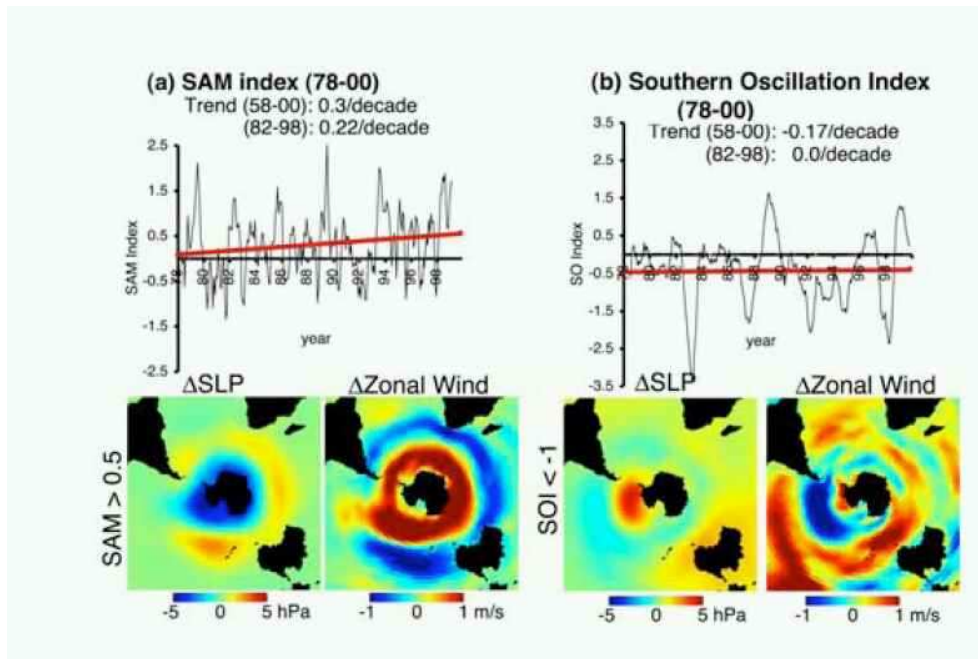


**Figure 6.1:** Trends of SAM and SOI and the related SLP and ZW anomaly patterns, from Kwok and Comiso (2002b).

A general long-term trend towards positive SAM and negative SOI values generates a characteristic pattern for atmospheric parameters:

- Positive polarities of SAM are accompanied by lower SLP over the Antarctic continent and within the Antarctic circumpolar trough. This pressure distribution leads to enhanced circumpolar Westerlies around Antarctica, except for the Ross Sea regions. There, the low pressure over the Amundsen Sea, in combination with the SAM, reinforces the northward flow component. Thus, reduced ice concentrations and less compression near the continent may be expected.

- The main effects of a negative SOI result in a dipole pattern with positive pressure anomalies in the Bellingshausen/Amundsen Seas. Furthermore, colder temperatures over the continent and a warming on the Antarctic peninsula can be found. Sea surface temperature (SST) trends show warmer temperatures in the Pacific region with a resulting ice edge retreat. Zonal winds are enhanced at the coast of the Amundsen Sea.

Investigations by Kwok and Comiso (2002a) show that SAM and SOI do not explain the same variance of the SST and are not directly correlated. The strongest influences occur in the regions of the Bellingshausen/Amundsen Seas, where the general pattern of positive SAM and negative SOI enforces an opposite pressure distribution, leading to a higher variability.

It may be speculated that variations of the SLP pattern are transferred to sea ice motion anomalies through wind forcing by the established relation between wind and sea ice motion (see section 2.1). Below, the relation of ice drift to the different modes of variability or to a combination of them shall be investigated .

## 6.2 Decadal Trend of Ice Motion and SAM

This section focuses on deviations from the typical long-term mean drift pattern of sea ice in an attempt to isolate modes of variability associated with SAM. From EOF analyses of 850 hPa height anomalies, the SAM turned out to be the dominant mode of atmospheric variability (2.2.2). It is directly linked to the meridional pressure gradient. From long-term investigations, SAM was found to exhibit a strongly positive trend. The impact of the corresponding pressure distribution on the ice motion field in some areas shall be studied here.

The impact becomes apparent by comparing ice motion composite fields of consecutive months with a strong positive index ( $SAM > 1$ ). They were selected on the basis of the SAM index defined by Nan and Li (2003). This index is defined as the difference in the normalised monthly zonal mean SLP between 40°S and 70°S - as opposed to the more traditional 65°S limit.

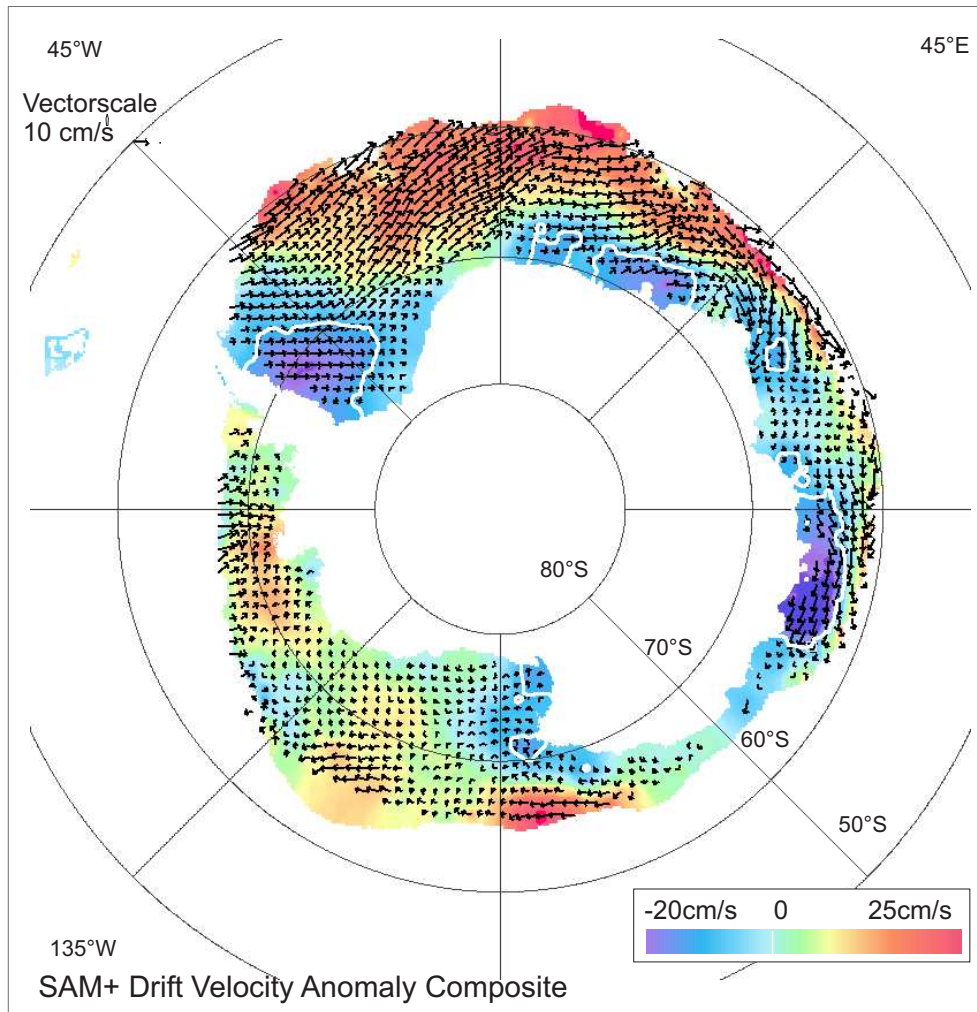


**Figure 6.2:** Mean drift velocity anomaly for all months with  $SAM > 1$ . The colour distribution shows areas of higher and lower than normal drift velocities. Vectors give the average direction of the drift.

This modified index is used to find a more robust relationship between SAM and the predominantly geostrophically forced sea ice drift south of 60°S. Furthermore, it is tried to mitigate any artificial bias introduced in the trend in the SAM index derived from NCEP reanalysis data (Hines et al., 2000). To determine how high values of the SAM index influence the sea ice motion pattern in comparison to periods of moderate SAM, the monthly mean drift anomaly field for these months (Figure 6.2) is studied. The monthly anomalies are obtained after removing the 1979 - 1997 monthly mean drift from the single monthly means. The parallel NCEP atmospheric reanalysis SLP and air temperature fields (Fig. 6.3) are added.

It is obvious from the composite (Fig. 6.2) that the sea ice drift pattern is considerably modified in response to the large-scale sea-level pressure anomalies during months with a persistently positive spring and winter SAM index. The eastward zonal component of drift is enhanced in the northern Weddell Sea and Ross Sea sectors (between 60°S and 70°S latitude), while the coastal drift in the southern Weddell Sea and around a significant part of East Antarctica is considerably slower than the average. In addition, the typical feature of SAM in the West Antarctic peninsula region is reproduced by an enhanced poleward meridional flow. East of the Antarctic peninsula, the Weddell Sea experiences an enhancement of the southward component of drift, whereas the northward component of ice drift over the entire Ross sectors is enhanced only slightly.

The corresponding chart of the distribution of meteorological parameters (Fig. 6.3) also shows the typical pattern for positive periods of SAM. The pressure field has a characteristic low in the Ross/Amundsen Seas, leading to enhanced poleward winds on its front and northwards winds in the central Ross Sea. These winds may explain the extremely low temperatures that occur in the areas of the Ross shelf ice as related to cold air outbreaks from the Antarctic continent. An enhancement of the zonal Westerlies north of 70°S is evident for most of the regions. The position of the 0°C isotherm shows the related extension of cold temperature to the North in the Ross and Weddell regions and the warmer air moving southwards in the Bellingshausen Sea. This, together with the poleward wind components, is presumably the main cause for sea ice retreat in this region.

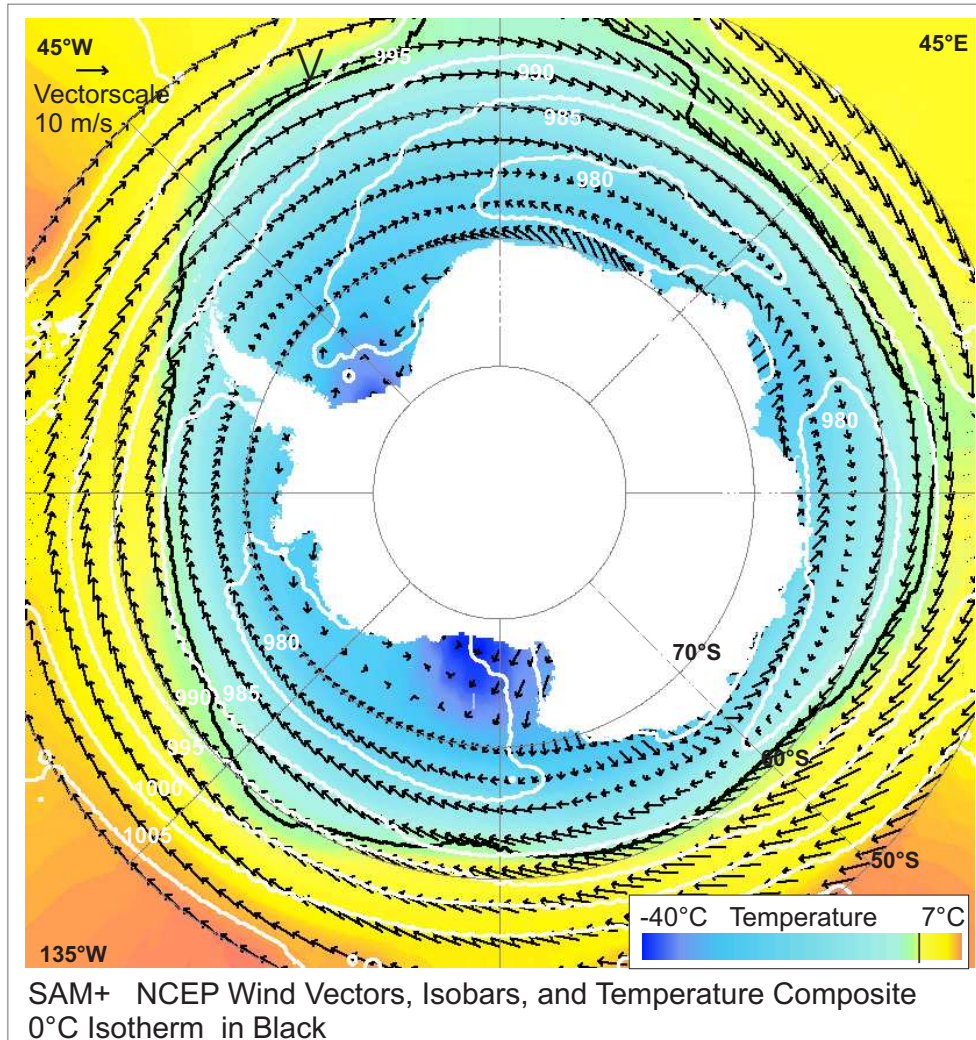


**Figure 6.3:** Mean meteorological conditions for all month with  $SAM > 1$ . The colours give the SAT distribution with the  $0\text{ }^{\circ}\text{C}$  isotherm highlighted black, arrows indicate mean wind vectors and SLP is given in 5 hPa increments (white lines).

It was expected that regions experiencing the effects of a positive SAM index would respond by an increased zonal component in velocity. To check this hypothesis, the complete timeseries of the zonal and meridional components have to be considered (Appendix, Figs. A.4 through A.7). Though the first three points located in the Weddell Sea indicate a weak (statistically insignificant) increase in eastward velocity, they likely are too far south (see Figure 5.1 for positions) to experience any significant effect in terms of zonally enhanced ice drift.

A better regional overview is obtained from the areawide distributions of the zonal and meridional drift trend (Fig. 6.4). Pronounced positive trends of zonal velocity occur in the outer regions of the Weddell Sea and, to a smaller extent, in the Ross and Amundsen Seas. Marked negative trends are observed for the westward zonal component of drift in the Indian Ocean, that is represented by point 4. Sea ice extension is not so far north there. Hence, the influence of the Westerlies is not predominant. Strongly positive (equatorward) meridional trends are evident at locations in the Indian Ocean and in the western Ross Sea. Interestingly, negative (poleward) meridional drift trends are observed in the Weddell Sea and around point 10, perhaps partly due to small increases in poleward components of surface winds in response to SAM and effects of the SOI that will be discussed in the following chapter. Besides the general distribution of the ice motion pattern corresponding to positive values of SAM, it is important to see, whether the overall positive trend of SAM can be related to similar trends in timeseries of ice motion. The major finding from the drift trend analysis (Section 5.2.3) is the observation of uniform long-term decreases in drift variance over most of the Southern Ocean sea ice zone. The results of the drift variance analysis (Tab. 5.2) indicate a robust, statistically significant downward trend of Antarctic sea ice drift variance at all points 1 - 10 over the 19-year's interval, with the strongest negative trends observed at locations 1, 3, 4, and 5.

The spatial pattern of the variance trends in Figure 5.10 shows a uniform reduction over most of the Southern ocean ice-covered region, with exceptions in isolated regions in the Bellingshausen and coastal Amundsen Seas, and the East Antarctic quadrant between 90°E and 145°E along the Wilkes Land coast.

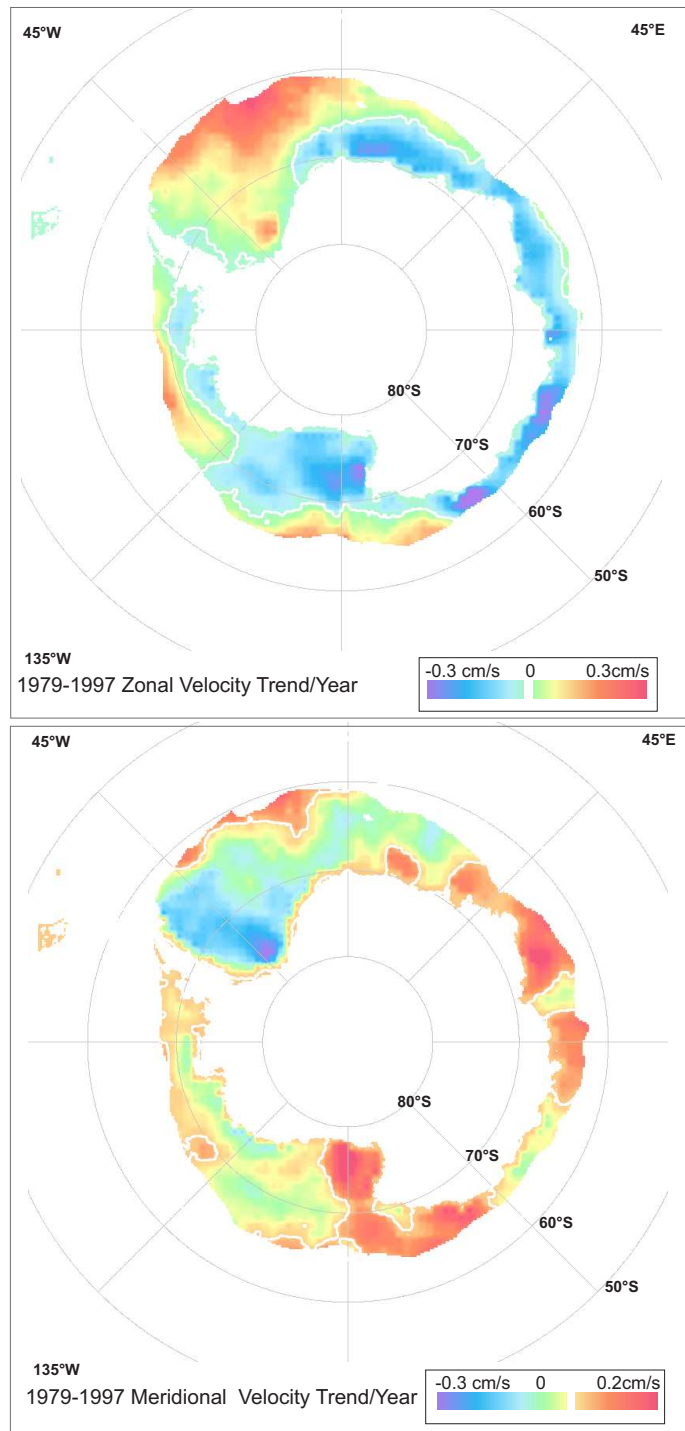


**Figure 6.4:** Regional trends of zonal (top) and meridional (bottom) ice drift velocity in cm/s/year. White isolines mark the separation between positive and negative trends.

The most striking feature is the dipole pattern with opposite trends on each side of the Antarctic peninsula and with the strongest positive trend in the centre of action of SAM. The positive trend in drift variance in the west Antarctic peninsula region implies a greater storminess and a resulting variance of drift speed and direction. This corresponds to the hypothesis of a positive trend in SAM being responsible for storms delivering more heat to this region and causing the observed regional warming trend. Warming is expected to cause thinner and more mobile sea ice conditions which - when coupled with stronger poleward meridional winds- may provide a dynamic explanation of the ice extent anomalies observed, and the lack of sea ice concentration anomalies (Kwok and Comiso, 2002). A contrasting long-term decrease in ice drift variance is observed over large parts of Antarctica and particularly in the Weddell Sea - implying a long-term reduction of storminess or cyclonicity at these locations. This may in turn indicate a corresponding reduction in drift energy that is expanded by the opening and closing of leads and ridging and, thus, of dynamic thickening of the ice pack. There is also the possibility that reduced dynamic thickening may potentially counterbalance any increase in thermodynamic thickening - as indicated by coupled model simulation (Lefebvre et al., 2004).

## 6.3 Interannual Variability

The most important interannual climate variations that occur over periods of several years have already been introduced in chapter 2.2.3. The interaction of alternating pressure patterns of the Southern Oscillations (SO) and anomalies of oceanic parameters that occur during ElNino are described by the ENSO. Although its centre of action is situated in the tropical Pacific, the effects are transmitted to the Antarctic and reflected by various parameters (Turner, 2004).

### 6.3.1 Relationship between Ice Motion and SOI

On sub-decadal timescales, the influences of variations of the SOI over periods of 3-5 years shall be investigated. Since the Western Pacific region turns out to be most sensitive and shows the strongest response to climate anomalies related to SOI, the main focus of the following investigations will lie on sea ice data from the Amundsen/Bellingshausen Seas. The dominant coupled mode exhibited by the sea ice response is the Southern Oscillation Index (SOI) with a variability on interannual timescales (Kwok and Comiso, 2002a). Investigations of power spectra of sea ice concentration and drift by Venegas et al. (2001) also reveal the time-dependent structure of the variability. They found a broad peak for the 3-6 year's period, with all data exceeding the 95% significance level, and a high correlation of this mode with the ENSO.

Within the large interannual fluctuations of the SOI, the main negative values occur during the ElNino years 1983, 1987, 1992, and 1998 (Fig. 2.2.1). These years are also referred to as warm events. They are accompanied by positive 500 hPa height anomalies in the Bellingshausen/Amundsen Seas (Turner, 2004). This pressure pattern which is also visible in Fig. 2.2.1 reinforces meridional wind components at the front and back. According to Yuan (2004), the Antarctic Dipole (AD), in combination with the see-saw pattern of ENSO, leads to fluctuations of the ice edge positions and anomaly structures. The direct influence on atmospheric parameters is shown by Kwok and Comiso (2002b), who gave a general overview of the mean atmospheric pattern by comparing composite images of SLP and zonal wind for the different states of SOI. Furthermore, they calculated trends of SST

for positive and negative values of SOI.

In a follow-up investigation (Kwok and Comiso, 2002b) that was extended to cover sea ice data, negative sea ice edge anomalies were found in the Pacific region for months with negative SOI. On the other side of the peninsula, the opposite effect was observed with positive ice edge anomalies. A comparison of the timeseries of SIE, SIA and SIC anomalies of the Bellingshausen/Amundsen Seas with those of the whole Southern Ocean emphasises the high sensitivity of this region. SIE and SIA show strongly negative anomalies in the ENSO years, while no direct link to SIC could be established. From the previous studies, the results of a negative SOI can be summarised as follows:

- Positive pressure anomalies west of the Antarctic peninsula reaching up to 105°W.
- Stronger positive meridional winds on the eastern coast of the peninsula and poleward winds in the Pacific Sector according to the mean pressure pattern.
- Resulting colder surface temperatures in the Weddell Sea and around it, and negative warmer SST in the Pacific Sector.
- Positive correlation with SIA/SIA, mainly in the Pacific region.
- Enhanced zonal winds in the Bellingshausen/Amundsen Seas, causing eastward ice motion along the coast.
- Enhanced meridional ice motion to both sides of the peninsula.

The average SOI is negative (Fig. 6.1). Thus, the long-term trends of meridional and zonal velocity (Fig. 6.4) are expected to represent to some degree the drift pattern for negative values of SOI. Special sensitivity of the Amundsen/Bellingshausen Seas to the fluctuations of the SOI (Kwok and Comiso, 2002a) makes this area as well as the eastern coast of the Antarctic peninsula suitable for investigating the response of ice motion.

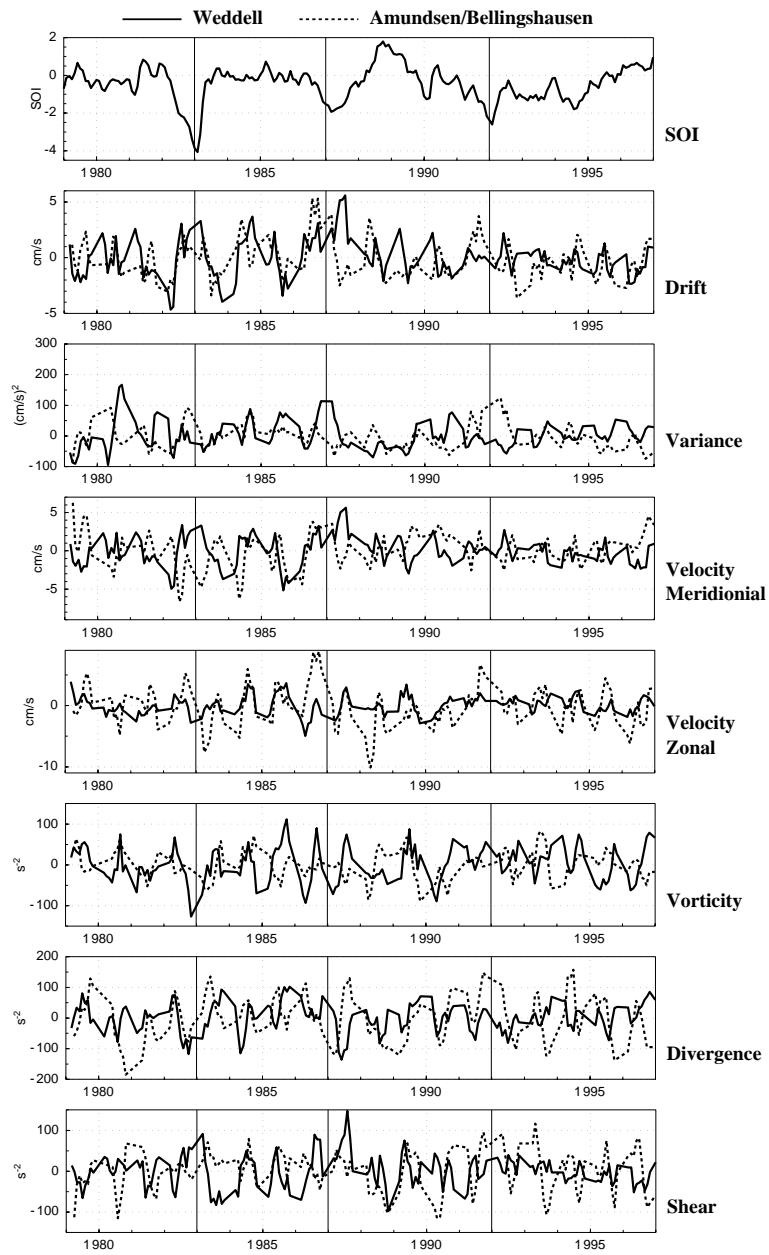


**Figure 6.5:** Time series of kinematics of sea ice properties and SOI. Periods of ENSO events are marked by black lines.

Ice drift statistics from these regions as well as certain differential kinematic parameters (see section 3.6) are obviously related to the SOI. The linear trend of ice motion has been subtracted to compare the fluctuations. This is important mainly for parameters with large decadal trends, such as the drift variance. The timeseries of drift velocity, its meridional and zonal components, the total variance as well as the differential kinematic parameters are compared to the SOI for the years of 1979 to 1997 (Fig. 6.5). The main ENSO events with the corresponding low SOI values are marked by vertical bars. For each parameter, the contributions from both sides of the Antarctic peninsular, e.g. the Bellingshausen/Amundsen Seas to the left and the coastal Weddell Sea on the right, are compared. Main variations of the SOI, e.g. the strongly positive and negative peaks are reproduced by the ice drift and variance data that show stronger positive fluctuations in the months with negative SOI and, vice versa for  $\text{SOI} > 0$ . Generally, the fluctuations on both sides of the Antarctic peninsula are of the same sign, with the peak values in the Pacific region occurring earlier than on the Atlantic side. A striking finding is the opposite behaviour of the meridional velocity component on both sides of the peninsular during the ENSO events. In contrast to this, the zonal drift in the Weddell sea does not seem to be influenced by the SOI fluctuations. In the lower panels of Fig. 6.5, the corresponding time-series of vorticity, divergence, and shear of the drift vector are plotted. The vorticity curves show mainly opposite patterns, indicating different cyclonic and anticyclonic rotation systems that exist on both sides of the peninsula. No direct response to the ENSO years can be detected.

For more details on the interactions in these two different regions, the correlation coefficient  $\rho$  of the kinematic sea ice properties and the SOI are calculated. Three months sliding means of both datasets are calculated to suppress noise as in Simmonds and Jacka (1995), but no further filtering is applied. The correlation coefficients presented here are zero-lag correlations.

The results of correlation calculations are summarised in Tab. 6.1. The drift velocity in both areas is negatively correlated. Thus, negative SOI results in generally higher velocity. The correlation coefficients in the Weddell Sea are higher than in the West, whereas the correlations with ice motion

Parameter	$\rho$ Amundsen	$\rho$ Weddell	Influence of negative SOI
Drift	-0.21	-0.37	Higher velocity on both sides
Variance	-0.26	-0.11	Positive anomalies on both sides
Drift V	0.35	-0.37	Equatorward acceleration Weddell Poleward acceleration Pacific
Drift U	-0.26	0.01	Enhanced zonal flow Pacific
Vorticity	0.08	0.01	No significant influence
Divergence	-0.24	0.28	Divergent motion Weddell Convergence in Pacific sector
Shear	-0.17	-0.35	Higher shear

**Table 6.1:** *Correlation coefficients of ice dynamics and SOI.*

variance are stronger for the Pacific region. The variance of ice motion in the Weddell Sea is not directly linked to the variability of the SOI. Instead, the relation between the decrease of variance and the SAM has been established.

The comparison of drift components reveals the main difference between the two ocean basins. The correlations with the meridional velocity are of opposite sign east and west of the Antarctic peninsula. This means that a negative value of SOI with the corresponding pressure anomalies over the Amundsen/Bellingshausen Seas results in positive equatorward drift anomalies ( $\rho < 0$ ) east of the peninsula and in an enhanced poleward movement ( $\rho > 0$ ) on the other side. Influence on the zonal velocity can only be noticed for the Amundsen/Bellingshausen Seas. There, the negative correlation with the SOI leads to enhanced zonal flow along the Pacific coast during ElNino events.

The ice drift derivatives are also influenced by the interannual fluctuations. Negative correlations of SOI and shear presumably cause higher shear stress in the ice, when SOI is negative. The Weddell region seems to be more sensitive to this, which is also visible by stronger fluctuations of the shear values in Fig. 6.5. Correlations of SOI with the ice motion divergence also varies consistently with the meridional drift components. The prevailing

northward movement of the ice in the Weddell Sea region leads to a stronger divergence, while convergent motion patterns dominate on the Amundsen side.

### 6.3.2 ACW in Ice Motion Data

The Antarctic Circumpolar Wave (ACW) introduced in section 2.2.4, is another mode of interannual variation found in atmospheric and oceanographic parameters of the Southern Ocean. Its anomalies occur as waves of wavenumber 2 that circle around the Antarctic continent. The strong eastward motion of the ACC is responsible for the displacement of the anomalies, and a system of interactions between atmosphere, ocean, and ice is believed to prevent the anomalies from disappearing.

The general mechanisms, that drive the consecutive anomalies are not understood completely, but can be explained by reactions of the ocean to atmospheric anomalies and vice versa. The main aspects may be understood in the following broad sense. Starting, for example, from an existing positive SLP anomaly somewhere in the Southern Ocean, this pressure system is accompanied by wind velocity anomalies. East of the SLP anomalies, equatorward winds are enhanced, while stronger poleward meridional flow prevails on the west side. This advects warmer air from the northerly regions and leads to warmer SAT in these areas. A weaker temperature contrast between the ocean and the air above leads to a reduced heat loss from the ocean to the atmosphere and negative heat flux anomalies take place. Positive anomalies in SST result from that. Thus, the ocean reacts to pressure anomalies after a defined time lag with enhanced SST and this, together with the poleward winds, leads to an ice edge retreat. Gloersen and White (2001) consider the correlation between the warmer water and the reduced sea ice extent an important factor that helps the anomalies to sustain. Although the sea ice disappears during summer, the memory effect is kept in the warmer SST.

The warm SST anomaly is advected with the ACC eastwards and, thus, into the areas of higher pressure. The atmospheric response to underlying warmer SST is a reduction in SLP that leads to a weakening and, finally, to a change of sign of the pressures anomalies.

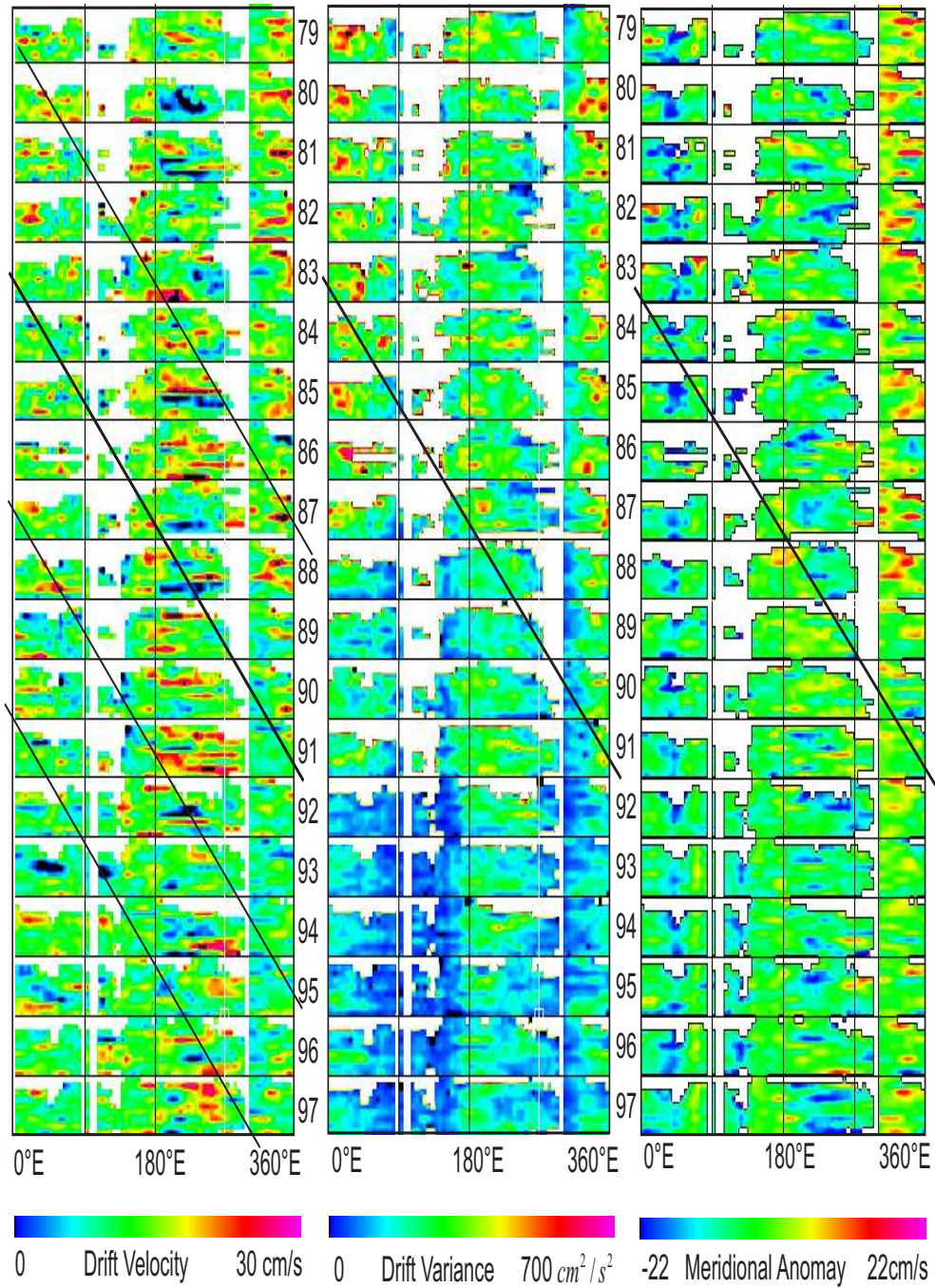


**Figure 6.6:** *Propagating anomalies in ice velocity, variance and zonal drift component around 70-65°S. Black lines indicate mean propagation after White and Peterson (1996). White areas mask land or open ocean, with no drift data. Each years values come from the months of March-November, no summer data are available.*

In this context, it is important to see, whether the patterns of the anomalies described above also have an impact on the ice motion or whether the drift anomaly itself can contribute to the maintenance of the propagating waves. To check this out, Hovmoeller plots of ice motion and anomalies are compared with respect to the already known characteristics of oceanic and atmospheric anomalies. As in the investigation of Venegas (2003), values are taken in  $5^\circ$  longitudinal increments around Antarctica.

In contrast to the results of White and Peterson (1996), whose investigation areas are further to the north at  $56^\circ\text{S}$ , these studies were restricted to areas that are covered by sea ice all around the year. Thus, the ice motion values come from the latitudinal range between  $70^\circ\text{S}$  and  $65^\circ\text{S}$ .

Figure 6.6 shows the averaged temporal and regional characteristics of mean ice motion velocity (left), meridional drift component (middle), and meridional velocity anomaly (right). The temporal resolution are monthly means and regional averaging is done by  $5^\circ \times 5^\circ$  increments. Due to the restricted availability of ice motion data in summer, the months March - November only were included in the calculations. The white areas mask land, e.g. the Antarctic peninsula at  $300^\circ\text{E}$  or areas with no drift data. The thick black lines give the characteristic of the exemplary cycle of anomalies according to White and Peterson (1996). They are included for a better orientation when referring to these anomalies.

The Hovmoeller diagram of ice drift (Fig. 6.6, left) shows a temporally alternating pattern of positive and negative anomalies that are most distinct in the Western Pacific areas. Thin black lines separate positive from negative areas and have a similar slope as the mean annual propagation according to White and Peterson (1996). This indicates that a propagating set of anomalies is present in the ice motion data, too. Following one of these lines from East to West, the origins of the anomalies in the Pacific Ocean can be traced back to anomalies in the sector of the Indian Ocean. To a smaller extent, they are encountered also in the Weddell areas and the Atlantic.

Interestingly, these anomalies seem to reoccur after the summer periods in all ocean basins, although there is no uninterrupted sea ice cover around all longitudes that might connect one with the other. In the data on sea ice motion variance (Fig. 6.6, centre), the propagation of anomalies is not

so obvious, since the main pattern is dominated by the decrease in variance (see 5.5) in the second decade of the data. In contrast to this general reduction of variance, the positive anomalies are concentrated on smaller areas, but consist of larger values. One series of positive anomalies is found to propagate through all three basins along the black lines in the plot. These lines represent the temporal-spatial characteristics of the most obvious pattern of propagating anomalies (White et al., 1998). Along these propagation lines, negative MWS and SIE anomalies and positive SST anomalies take place. The preceding positive pressure anomalies are phase-shifted by  $90^\circ$ , this means to the right side of the lines.

The negative (poleward) anomaly of MWS that prevails on the trailing side of the positive pressure anomalies results in a stronger forcing of southwards sea ice motion. This is evident from the left of Fig. 6.6, where the magnitude of the meridional velocity component is plotted. Positive anomalies of ice motion variance come along with an intensified zonal velocity. Dark blue values that indicate strong poleward velocities can be traced along this line through all three ocean basins. This effect, together with the prevailing positive SST anomalies, can intensify the retreat of the sea ice margin.

The interaction of these processes plays a role for the record decrease in SIE for the Amundsen and Bellingshausen Seas in the years 1988 to 1991, which is discussed by Turner et al. (2003). The anomalies of atmospheric patterns can be traced back up to five years ago, when situated in the Indian Ocean. This feature does not have the form of enhanced poleward meridional ice motion in Fig. 6.6, but the enlarged areas of missing drift data may result from this effect, since the warm moist air that is advected polewards causes a decorrelation in the surface radiometric signatures and prevents robust sea ice tracking during this period.

In the years afterwards, a change towards positive meridional velocity is evident. It matches the opposite pattern of anomalies. On the forefront of approaching negative pressure anomalies, the mean ice motion pattern turns to an equatorward motion. This is also evident from the positive anomalies of the total velocity that show higher values, as they occur in the vicinity of lower pressure. Furthermore, wind forcing results in higher amounts of sea ice export in these areas. As these atmospheric anomalies sustain during the

multi-year cycles, they can influence the sea ice from one year to another, or even in adjacent ocean basins, that have no direct connection.

Summarising the results, it may be stated that propagating anomalies, such as the ACW, can also be found in kinematic sea ice data. This implies that dynamic processes in the atmosphere and in sea ice are coupled. The area investigated is mainly situated in the inner pack and in regions with a higher amount of sea ice cover. Thus, it can be shown that the pattern of the ACW is not restricted to changes at the ice margin. The reaction of sea ice motion can be related to changes and anomalies in the forcing parameters. Furthermore, the ice motion may help intensify these effects and, thus, contributes to maintain the anomaly cycles by interaction with atmospheric and oceanic processes.

## 6.4 Annual and Semiannual Variability

The smallest scale of oscillation modes that covered by this investigation is the variability in annual and semiannual periods. For the areas of the Southern Ocean, the most common mode is the Antarctic Semiannual Oscillation (SAO), the mechanisms of which are explained by van Loon (1967).

The SAO is the half-year pressure oscillation that has two minima in October and March. The amplitude of these pressure waves increases with higher southern latitudes. Generally, the October minimum is more pronounced since the deepest cyclones occur in the ACT in this month (Walland and Simmonds, 1999). The background of these pressure waves comes from different temperature cycles over the Antarctic continent and the Southern Ocean. In autumn, the onset of cooling over the continent is one or two months earlier than over the ocean surface. In addition, the raise of temperature in these regions starts earlier than over the continent. The two annual temperature cycles are out of phase and have different rates of warming and cooling. This results in a meridional temperature gradient with a semiannual structure, forcing baroclinity change and, by this, the half-year wave in surface pressure. The SAO itself has a decadal variability and Walland and Simmonds (1999) suggested that sea ice influence could modulate these oscillations.

### 6.4.1 The Seasonal Cycle of Ice Motion

The purpose of this section is to reveal, whether ice motion also has a significant annual cycle and what its main characteristics look like. A first approach is done by visually comparing monthly mean drift velocities at the investigation points that have been specified in chapter 5.1. For a representative illustration of annual cycles, the 19-year average ice motion is calculated for each single month.

The resulting curves of mean drift velocity at ten different points located clockwise around Antarctica (Fig. 6.7) illustrate the range of possible annual cycles of ice motion. They differ in the magnitude of the amplitude between minimum and maximum velocities as well as in the periods when these values occur. The first three points in the Weddell Sea have similar

annual amplitudes of around 2 cm/s, while further eastwards, the differences between minimum and maximum drift in the coastal regions of the Indian Ocean (points 4 and 5) become quite large, up to 16 cm/s.

As regards the phase, this region as well as the Weddell Sea which is close to the Antarctic peninsular show a similar behaviour with high values at the beginning of the sea ice season in March and April and constant velocity reduction during the year until minimum values are reached in October and November. The velocity in the central Weddell Sea (point 3) is different. Its minimum is reached earlier during the year in mid-winter and there is a subsequent increase in the drift velocity towards the end of the year. In the coastal regions of the Pacific Ocean and the Ross Sea (points 6 through 9), velocity amplitudes are larger than in the Weddell region and the annual cycle of ice motion velocity shows two local maxima. The magnitude of the second peak in the later winter months becomes larger and more dominant when following points 6 through 9 clockwise around Antarctica. This behaviour does not seem to be influenced by the fact that the amplitudes are higher at point 6.

In the adjacent Amundsen Sea (point 10), the velocity pattern is inverted with minimum velocities at the beginning of the season and a maximum towards the end of winter.

This regionally different distribution of phases and amplitudes of the annual cycle of ice motion velocity gives rise to the question whether these first results can be extrapolated to the whole sea ice region and what are the main influences causing this distribution.

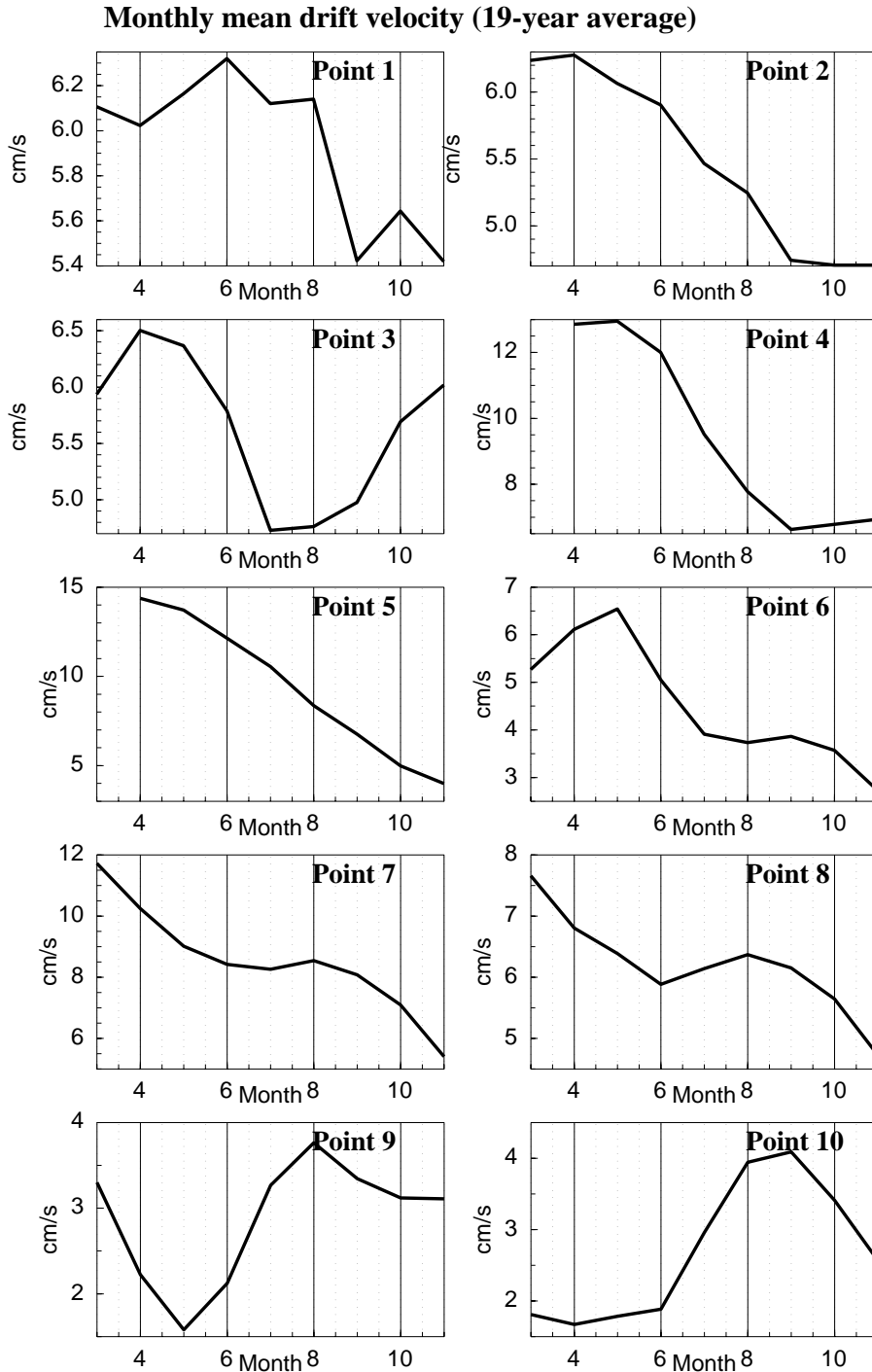


**Figure 6.7:** Annual cycle of drift velocity at selected points. The curves represent the sliding means of the 19-year average drift velocity for each month. The numbers of the points refer to the positions given in Fig. 5.1.

### Discussion of Different Phases/Amplitudes

Seasonal variability of ice motion can be classified into different groups, depending on the positions of and the intervals between minimum and maximum values. Below, three different classes adapted to different velocity curves will be distinguished to obtain a coarse classification of the motion field.

Class	Max	Min	Curve Description
1	Autumn	Spring	Decreasing
2	Autumn + Spring	Winter	Two Peaks
3	Spring	Autumn	Increasing

**Table 6.2:** *Classes of different annual cycles of drift velocity.*

Class 1 relates to drift velocity decreasing constantly during the year which means that the gradient  $\Delta v/\Delta t$  remains negative throughout all months. The minimum velocity is reached at the end of the sea ice season, which means November for most of the gridpoints. For class 3, an opposite behaviour is supposed, with increasing velocities that reach their maximum in the last months of the year. Points with changing sign of the gradient, e.g. several maxima, belong to class 2. Here, examinations reveal that the drift minimum is flanked by two maxima, but not the other way around. This also includes the cases very similar to class 1, where the velocity starts with highest values and decreases constantly, but only in the last month, the second increase takes place. The velocity distribution with maxima in spring and autumn in this class resembles the semiannual pressure variation introduced above and suggests negatively lagged correlations.

The above classification scheme is applied to the complete ice motion database and allows for the calculation of the areawide distribution of different drift patterns. Furthermore, the regional velocity amplitudes for the annual drift cycles are calculated at each point. The classification result and regional distribution of amplitude ranges are illustrated in Fig. 6.8.

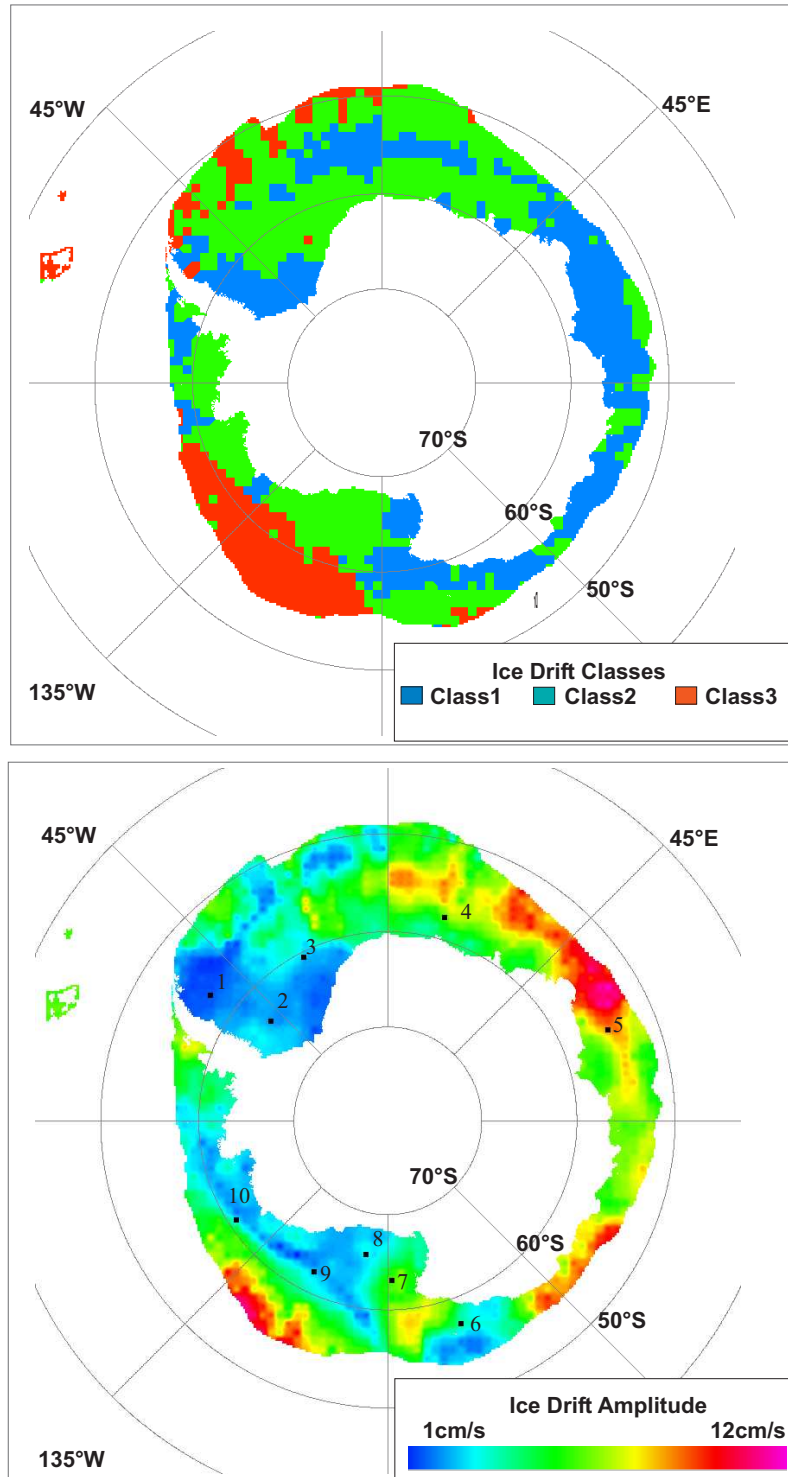


**Figure 6.8:** Classification of ice motion phases into three classes according to Tab. 6.2 (top) and amplitudes of the annual drift cycle (bottom). Black dots give the position of the investigation points as in Fig. 5.1.

Around the coast, the results of the classification (Fig. 6.8, top) present a pattern of alternating occurrence of class 1 and class 2. This means either a constantly decreasing velocity or a second maximum during the year. The coarse division is as follows:

- Class 1: Western Weddell 300 - 340°E
- Class 2: Central Weddell up to 45°E
- Class 1: East Antarctica 45 - 160°E
- Class 2: Ross/Bellingshausen/Amundsen Seas

Class 3 mainly results for areas from the outer sea ice regions that are influenced by the ACC already. These show increasing velocity and maximum ice speed at the end of the sea ice season. Interestingly, this class exists mainly in the western part from 0°W to 180°W, with the main contributions from the Pacific regions north of the Ross and Amundsen Seas. From Fig. 5.1 it is obvious, that most parts of these regions are outside 50% concentration already. This means that these regions are not constantly covered by sea ice and that the sea ice season, from which drift minima and maxima are computed, is reduced to a few months, which limits the possibility of finding changing signs in the temporal gradient.

The corresponding velocity amplitudes (Fig. 6.8, bottom) that represent the difference between annual minimum and maximum velocity vary from 1 cm/s to 15 cm/s. The lowest drift amplitudes can be found in regions of highest annual means of ice concentration or even perennial ice. The ice existing there is thicker and denser already than elsewhere and restricts fast acceleration and the consequential high drift amplitudes. This connection also explains the isolated field of high drift amplitudes north of the Pennell coast (170°E). This area differs from the surrounding ones by lower average ice concentrations and repeated ice-free summer seasons. This pattern of mean sea ice concentration in summer is also shown by the characteristics of the 19-year's mean March concentration isolines in Fig. 6.16.

The general regional distribution of drift amplitudes resembles the one of phase classification to some degree. A closer comparison, however, reveals an

opposite behaviour of the Weddell region compared to other regions. Everywhere else, the areas with two velocity maxima (class 2) are among the areas of lowest drift velocity amplitudes. In contrast to this, the adjacent areas of class 3 in the South Pacific and class 1 in the Western Ross and the Indian Ocean show clearly larger velocity intervals. In the coastal parts of the Weddell Sea, the regions with smallest velocity amplitudes belong to classes 1 and 3, however.

### Relations to Atmospheric Forcing

The details of the above examination suggest that the seasonal changes of the ice motion -according to the classification- result from different impacts. Following this assumption, the influence of meteorological forcing factors shall be considered and corresponding cycles of meteorological parameters investigated. When relating ice motion data to the SAO, it should be kept in mind that the SAO was the dominant signal in the annual cycle at middle and high southern latitudes before 1979. Its intensity has significantly decreased in the last two decades from which the ice data originate. Meehl et al. (1998) found anomalous meridional temperature gradients to be responsible for this change. Weaker amplitudes of the SAO result in increasing annual cycles of mean wind speeds and cloudiness, especially in the Bellingshausen/Amundsen Seas (Broeke, 2000). This leads to negative sea ice anomalies in winter and enhanced warming and, thus, reinforces the anomalies of the meridional temperature gradient.

The annual cycles of SLP, temperature, and wind velocity (Fig. 6.9) are analysed at points that are representative of the three different ice classes given in Tab. 6.2. In contrast to meteorological data that represent the complete annual cycle, ice motion data only exists from March to November.

Annual curves of ice concentration (not shown) have a similar behaviour at all points and consist of annual cycles with minima in February and rapid increase during the following two months. This is in agreement with investigations of Broeke (2000), who documents a half-year wave of sea ice cover with a stable phase. Further comparisons of amplitudes of sea ice cover, temperature, and pressure for the Bellingshausen/Amundsen Seas yielded

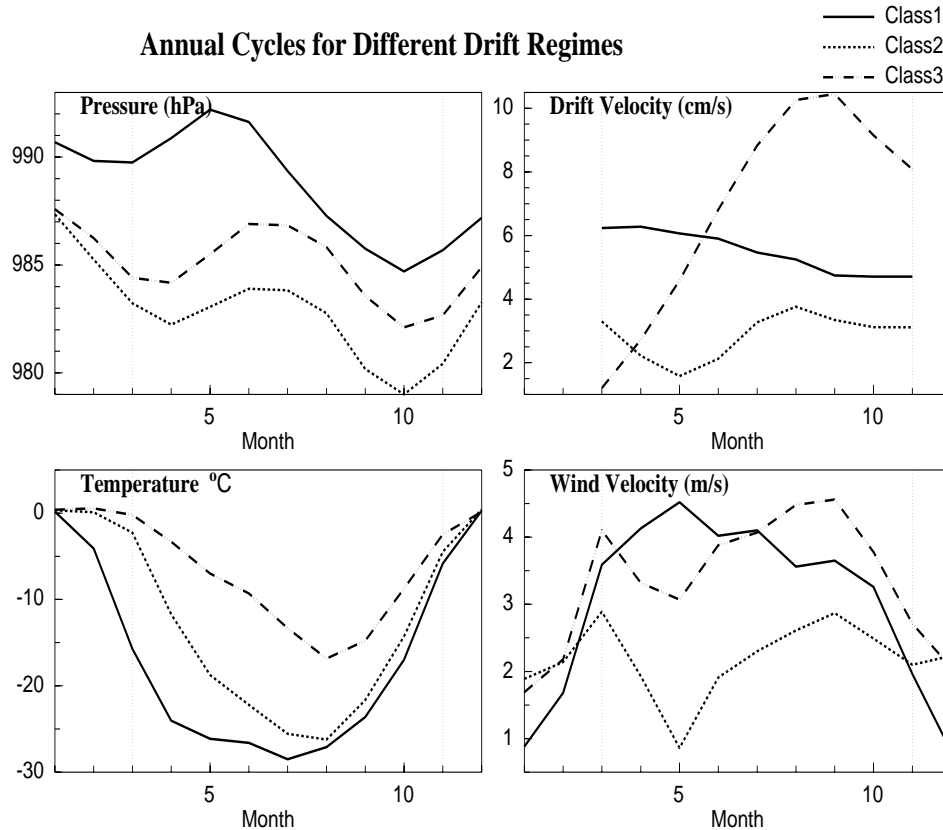


**Figure 6.9:** Annual cycles of pressure, temperature, wind velocity, and ice motion for different drift regimes. Class 1 is represented by values from the central Weddell sea (around point 2), class 2 describes the big area in the Ross seas, and class 3 the region in the Pacific Ocean around  $225^{\circ}$  W.

relations between decreasing annual pressure amplitudes and the decrease of sea ice cover.

Intercomparison for pressure and temperature (Fig. 6.9, left) shows local variations, but no striking differences in annual cycles. The pressure exhibits the typical annual two-phase cycle of the SAO, with a summer maximum in January and another in the winter months May and June. Typically, lower pressure occurs in March/April and October. The varying magnitude of the pressure is due to the geographic positions of the exemplary points and the fact that pressure amplitudes get stronger towards the south. SLP values from class 1 in the Weddell Sea show the largest amplitudes of the pressure

cycle and come from the most southerly positions.

When comparing this to the 19-year's mean pressure pattern (Fig. 2.1), it is obvious that the area selected for class 1 is still influenced by the generally higher pressure fields on the Antarctic peninsula that influence the regions of the western and central Weddell Seas. The locations chosen for classes 2 and 3 are situated in the central Ross Sea and the Pacific Ocean, where generally lower pressure systems prevail.

The magnitude of the temperature is also linked directly to the geographic position. Moreover, temperatures differ in a way that in class 3, negative temperatures, e.g. the onset of freezing, occurs not before March. This means that ice formation there starts later than in the other areas, where earlier built ice may be transported additionally. The temperature gradient in these areas is not so strong, and the minimum temperatures are reached later in the year. Admittedly, temperatures around  $0^{\circ}\text{C}$  are reached for all classes at the same time at the end of the year, which does not indicate any regionally different impacts.

Comparison with the wind velocities (Fig. 6.9, right) reveals the greatest sensitivity of the ice drift behaviour. All three locations show a local minimum for the months December to February, where no ice motion is tracked. Only wind velocity in class 2 shows a second minimum and a following increase that runs parallel to the drift velocity in the ice motion curve above.

The details of the above examination suggest a close relationship between the different annual drift cycles and wind forcing in selected regions. The ice velocity of class 2 reacts strongest to changes in the wind velocity, which results in two velocity peaks during the year. However, the changes in wind velocity magnitude per month are stronger there than in the two other classes. This leads to the assumption that not only strong winds but also large interannual amplitudes are necessary to force a second velocity maximum of sea ice motion later in the year.

In class 3, ice motion is generally faster, which is caused by the average position of gridpoints of this class being at the ice margin. There, the motion is already influenced by the ACC, leading to strong zonal ice flow. As the ice grows during the year, this effect becomes more and more important and

the variations of wind forcing do not influence the ice velocity as strongly as elsewhere.

### Classification of Sea Ice and Atmospheric Parameters

In order to obtain a general classification of the meteorological parameters into the different classes of drift cycles, value discretisation and histogram evaluation are carried out for all meteorological parameters relating to the three ice classes.

The ice drift velocity distribution (Fig. 6.10) reveals that class 1 and class 2 cover the same velocity range up to 12 cm/s and their main contributions come from velocities around 4 to 5 cm/s. Only class 3 is marked to be different from the others by covering higher velocity values beyond 20 cm/s.

An indicator of the difference affecting the division into class 1 and 2 is visible in the histogram of the ice motion variance (Fig. 6.11). Although all three classes represented there cover the whole range of variance values, class 2 clearly differs from class 1 by having a large maximum at variance values around  $250 \text{ cm}^2/\text{s}^2$ . They are in the same range as the values of class 3 that represents areas of higher and constantly increasing drift velocities during the season. Thus, the regional distribution in classes 1 and 2 in Fig. 6.8 differs mainly by the magnitude of variance that is remarkably larger for class 2. This gives rise to the question for reasons of regionally different drift variances.

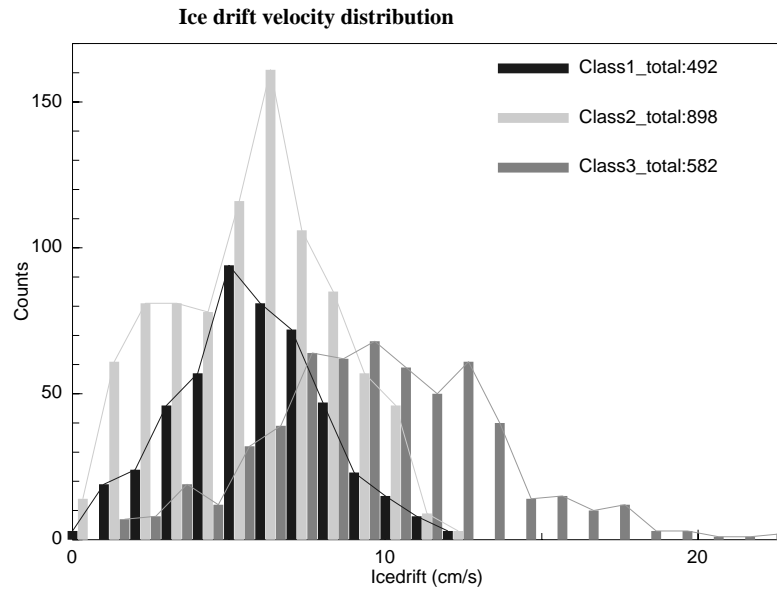


**Figure 6.10:** *Distribution of ice motion velocity to the different classes.*

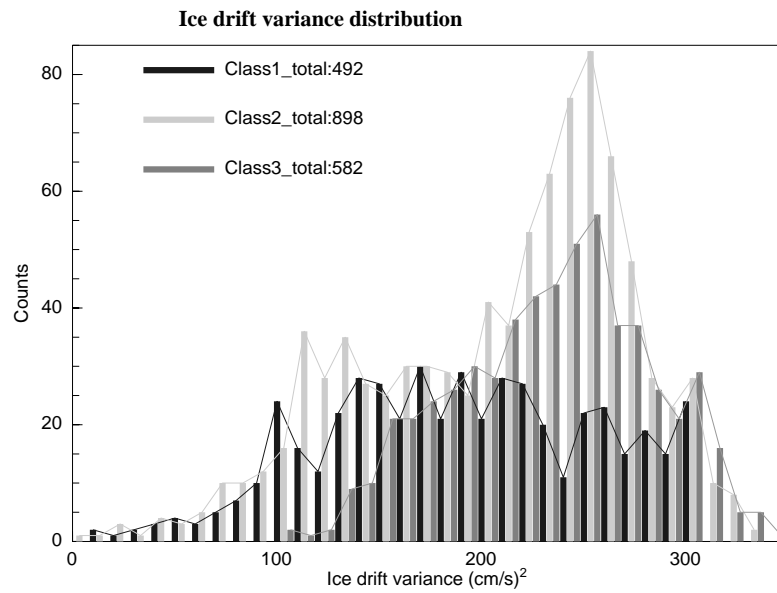


**Figure 6.11:** *Distribution of ice motion variance to the different classes.*

Relation to the SAO is discussed by similar histograms for the distribution of pressure amplitudes, e.g. the difference between minima and maxima for the annual cycle.

They document (Fig. 6.12) that there are amplitudes of up to 25 hPa. The larger part of the values are up to 15 hPa and distributions for all three classes are similar. Class 2 differs from the other ones by a peak shifted towards higher pressure amplitudes. Furthermore, the distribution is broader than the others, including many values in the range from 15 to 23 hPa. This characterisation of pressure values belonging to class 2 points out that mainly in areas with larger values of the SAO, e.g. higher pressures amplitudes, the sea ice motion reacts by building up a two-phase cycle.

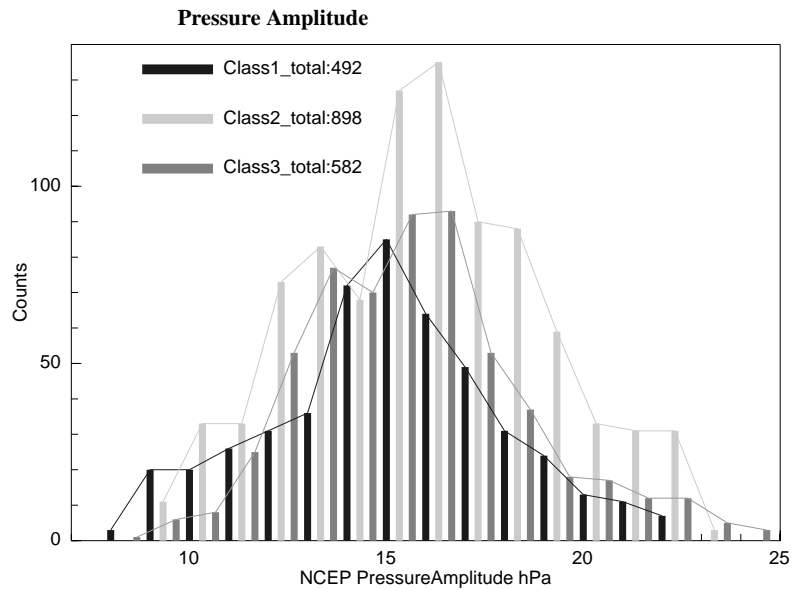


**Figure 6.12:** *Distribution of pressure amplitude ranges for the annual cycle of NCEP SLP.*

The histogram of the wind velocities from NCEP data (Fig. 6.13) related to the annular cycles of ice drift speed has a similar shape as the one of the drift velocities, indicating a generally good agreement of wind forcing and resulting sea ice motion. The remarkable difference, that separates class 2 from the others is that not only the velocity maxima occur in the same range as class 1 at around 4 m/s, but also a second group of high values around 7 m/s. Wind velocities of this magnitude are rarely found in class 1. This confirms the above conclusion that a certain magnitude of wind velocity is necessary for the ice to react quickly to changing accelerations.

Another interesting difference comes from the temperature distribution in Fig. 6.14. Although the areas of class 1 and class 2 are regularly distributed around the Antarctic continent and exist at the same latitudes, class 2 includes large contributions from temperatures higher than  $-10^{\circ}\text{C}$  that are only sparsely represented by class 1. Thus, these areas are those with higher wind velocities and higher temperatures. Both influences make it easier for the ice to react to wind forcing.

Summing up, it may be stated that the ice motion shows a clear annual cycle that differs regionally. The regional differences in wind forcing have a greater impact than ice concentrations on the formation of the different classes. This is documented by the different contributions of wind velocity ranges and temperature values to three groups of ice motion.

The outer areas, mainly those in the western parts of the investigated regions, are characterised by a constantly increasing ice motion velocity during a season. In contrast to this, velocity in the inner ice regions is either decreasing constantly or until midwinter, followed by a second maximum in the later year. Only in these areas with two maxima, can a relation of the annual cycle of ice motion to the SAO be established. These areas reflect that a combination of prevailing stronger wind velocities, higher than usual temperatures, and well pronounced annual pressure amplitudes is necessary for building up conditions that permits the ice to react directly to the changes in wind velocity that come along with the SAO.

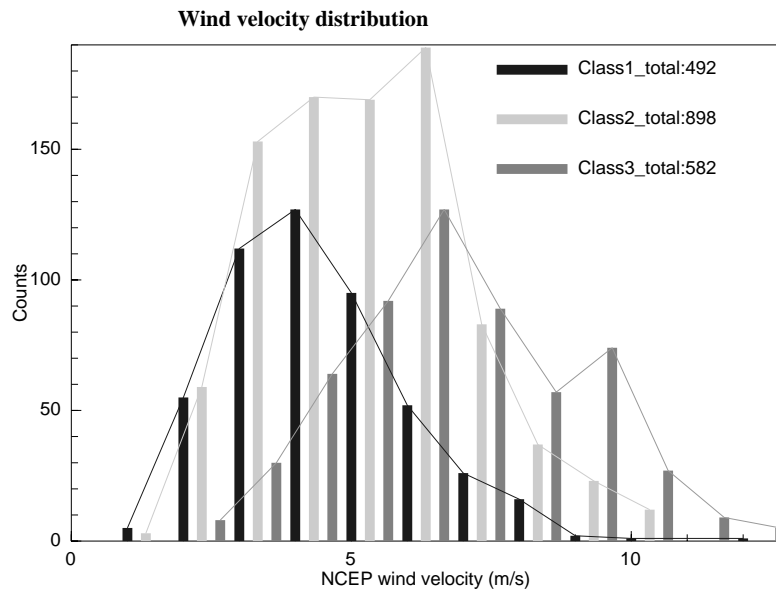


**Figure 6.13:** *Distribution of NCEP wind velocities to the different classes of ice motion cycles.*

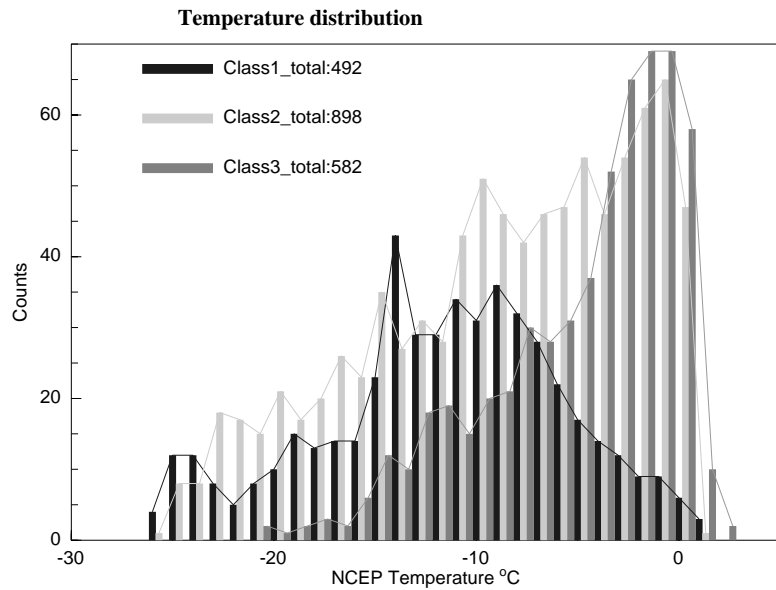


**Figure 6.14:** *Distribution of NCEP temperatures to the different classes of ice motion cycles.*

### 6.4.2 Sea Ice Margin Variations

Satellite-tracked ice drift, in conjunction with ice concentration, allows to resolve ambiguities in the relative contribution of dynamics and thermodynamics to anomalies of sea ice concentration changes, within the pack or at the ice margin. This information is useful in diagnosing the impact on atmosphere-ice-ocean fluxes.

It was pointed out above that the sea ice extent varies considerably from year to year. Similarly, the position and displacement velocity of the ice margin changes for different regions. When investigating these changes, the question for thermodynamic and dynamic causes for ice margin displacement arises.

Ice margin data are used simultaneously with information on the ice motion and air temperature to obtain an improved impression of the different dependences. The position of the ice edge is obtained from sea ice concentration maps by defining a minimum concentration threshold. According to various studies of SSMI-based ice concentrations, small concentrations values tend to be overestimated (Heygster et al., 1996). The 15% and 33% thresholds are proposed as reliable values for the ice margin definition. According to Turner et al. (2003), who use 33% concentration as the limit of the ice and find good agreements with the ice edge derived from AVHRR data, the 33% ice edge data from PELICON (Heygster et al., 1996) are used for further investigation.

In the first step, monthly mean meridional ice margin displacement velocities are calculated from the daily concentration maps. With the 33% isolines being interrupted lines, some spatial smoothing is necessary. This is done by fixing small longitude intervals of  $5^\circ$  clockwise around the ice area and averaging the position over all latitude values within these intervals. This leads to regularly spread ice margin positions for all months. Displacement velocities are computed using the position changes from one month to another.

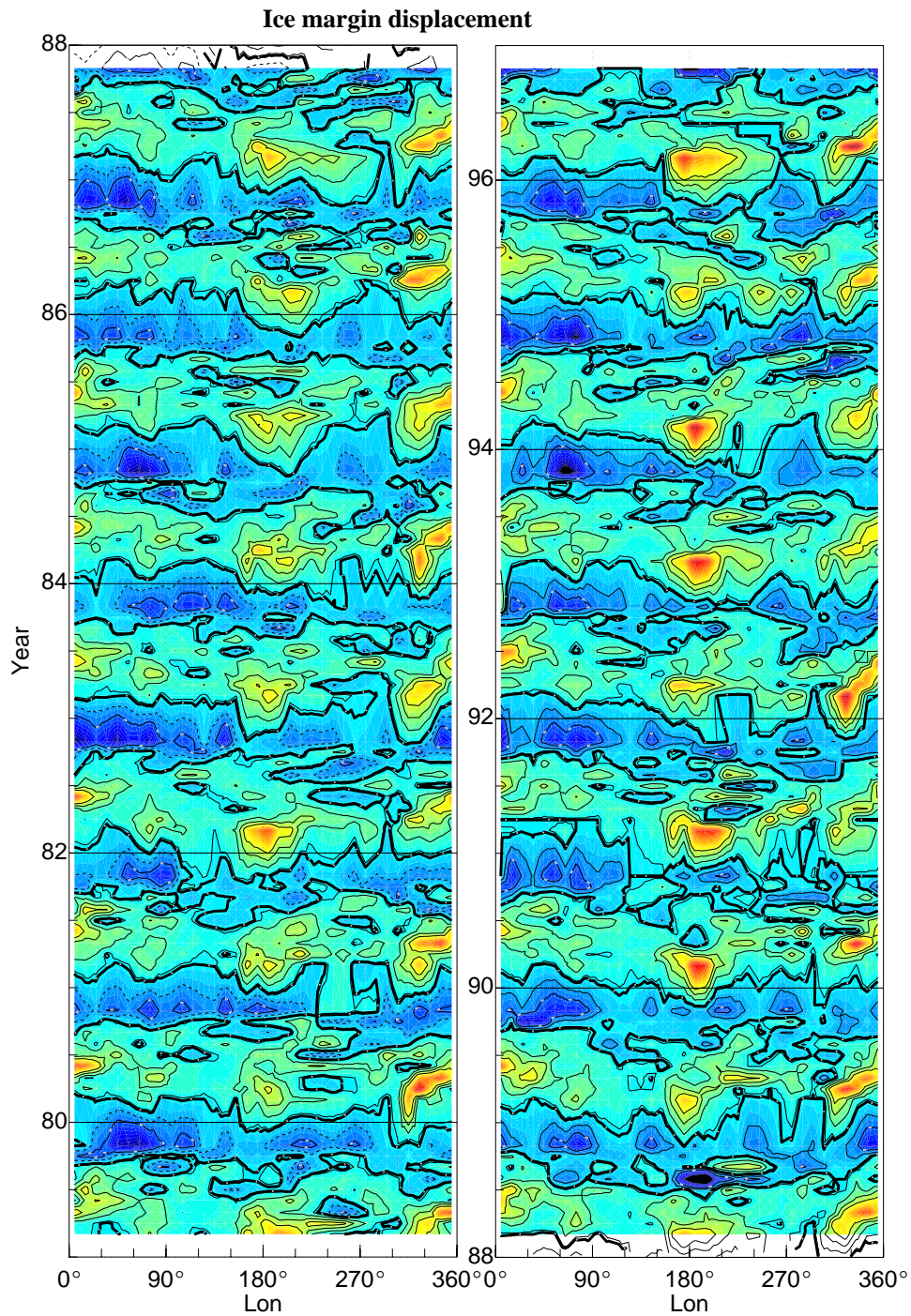


**Figure 6.15:** Monthly mean meridional displacement velocities of the sea ice margin from 0-360° E. Positive (green-red) and negative (blue) values are separated by the solid black isoline.

For the period from 1979 to 1996, monthly mean meridional ice margin displacement velocities show a general spatial structure determined by the seasonal cycle (Fig. 6.15). The positive displacement values in the first half of the year and ice retreat in the second half are in line with the annual cycle of sea ice advance in autumn and winter and edge retreat in the spring months with main ice melting. Similar longitudinal distributions of high and low values are evident in every year. The fastest northward displacement appears as a three-maxima pattern, with the extreme values centred in the regions of the big ice shelves in the Weddell Sea (300-30°E), the Ross Sea (160-230°E), and around the Amery ice shelf (70-80°E). In autumn, the Ross sector shows the earliest onset of the fast northward movement in the whole basin, whereas in the Amundsen/Bellinghousen Seas sea ice retreat prevails in some years. Ice margin advance in the Weddell regions generally starts later, and there is an evident shift of the maximum to the later months of the year for the regions closer to the 0°E meridian. Generally, positive intensities in the Weddell Sea are stronger than the others. Opposite distribution with the highest maxima in the Ross Sea occurs in the years 1979, 1982, 1990, 1991, and 1994.

This general distribution of displacement maxima can may be attributed to the mean sea ice concentration for different areas. The 1979-1996 mean sea ice distribution for March (Fig. 6.16) reveals the above-mentioned areas of ice displacement maxima to be among the regions where most of the sea ice sustains during the summer months. There, sea ice has a larger extent even in summer, but with lower concentrations, as is indicated by the wide distance between the isolines. With the annual extension of the ice margin to the north being caused by the thermodynamic growth of new ice and the wind- and ocean-driven movement of the ice, these areas profit from already existing ice that may intensify the export. In the autumn and winter season, the ice can extend faster northwards in above-mentioned regions, since there is not only the newly built ice, but also ice from the last season that exists in lower concentration already. This also explains the temporally shifted higher velocities in the Weddell Sea itself, since most of the sea ice is concentrated on the coast of the Antarctic peninsula in the summer months.

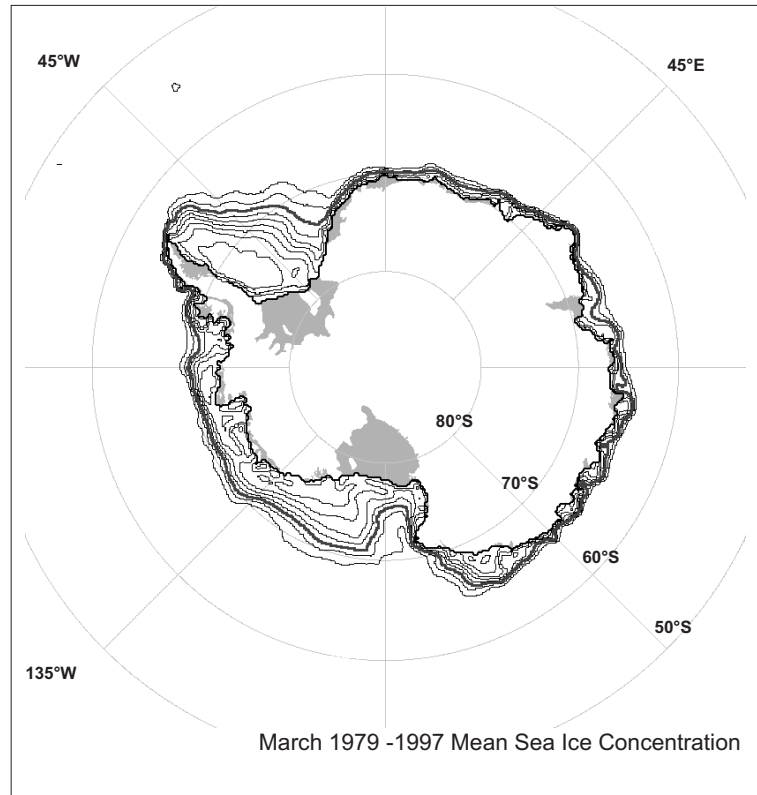


**Figure 6.16:** 1979 -1996 mean sea ice concentrations for March. Isolines have a 10% interval, the 30% line is highlighted black.

The areas of maximum ice margin retreat are shifted eastward from the centres of maximum advance. The two main ice margin retreats take place in the areas around the Amery ice shelf east of the regions of fastest advance in the Weddell Seas and in the Bellingshausen/Amundsen areas around 270° E. The minima occur mainly in the beginning of the ice margin retreat season. Then, sea ice has its maximal extension and the sea ice margin is, in wide regions, strongly influenced by the motion of the ACC (Fig. 2.1).

### **Dynamic and Thermodynamic Influences on Ice Margin Displacement**

Summaries of seasonal climatologies of ice drift generally document a lower mean summer drift velocity in response to relatively light winds. As Aus-

tral winter sets in, the large-scale synoptic pressure patterns establish in the eastern Weddell and Ross Seas. In response, steady northerly components of sea ice drift are observed east of the Antarctic peninsula and in the western Ross Sea.

An example of the dynamic and thermodynamic conditions at the ice edge during the main freezing months (March-June) is given in Fig. 6.17 for the years 1985 and 1996.

For March and April, the curves of ice margin displacement and temperature show nearly opposite pattern in both years, indicating strongly negative correlations. The above-mentioned sectors with the strongest positive displacement also have lowest temperatures. Comparison of April 1985 and 1996 reveals the different influence of ice motion. In 1996, the main component of ice motion is northward, while in 1985, motion vectors show zonal or even southward components, except for the Weddell area. Hence, this is the only place with a very rapid ice margin advance in this year.

In May and June, the displacement and temperature decorrelate and the influence of ice motion becomes stronger. Zonal components as in May 1996 around  $270^{\circ}\text{E}$  cause the ice extension maxima to be displaced not directly to the north, but to the northeast. In June 1996, despite high temperatures, the ice margin displacement around  $230^{\circ}\text{E}$  shows strongly positive values. There, the regions around the  $0^{\circ}\text{E}$  meridian have largest displacement values. Ice motion in these areas is oriented to the west, indicating that the marginal ice zone is strongly influenced by the Antarctic Circumpolar Current.

To distinguish between the temporally and regionally different influences on the sea ice margin displacement, correlations of the edge displacement velocity with the ice motion velocity and air temperature at the ice margin are calculated for all the years.

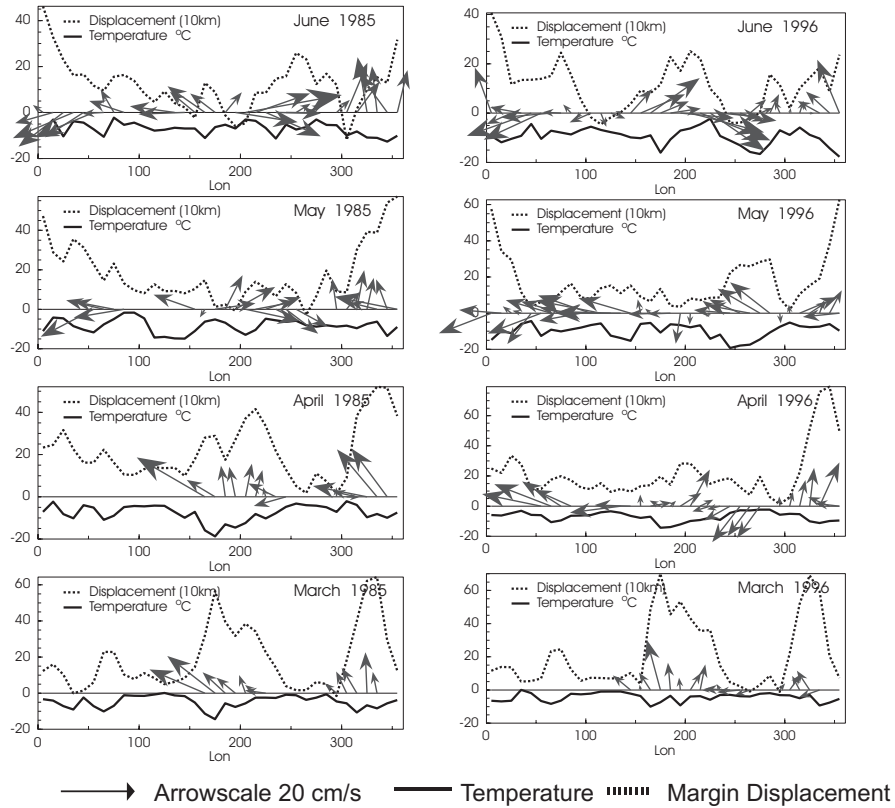


**Figure 6.17:** Monthly mean ice margin displacement (10 km)(dashed line), temperature ( $^{\circ}\text{C}$ ) at the ice margin (solid line), and ice motion vectors. Iso-lines show the average monthly displacement of the ice margin and the mean temperature at these positions. Arrows indicate the mean ice motion vector, if available.

For the whole investigation period and averaged over the whole region (Fig. 6.18), the positive correlation of ice margin position with meridional ice motion velocity is obvious. This means a dynamic displacement of the ice edge to the north and a negative correlation with the temperature at the ice edge that is caused by ice extension due to thermodynamic growth. Strongest correlations occur in the first three months (autumn), when the ice area starts to grow.

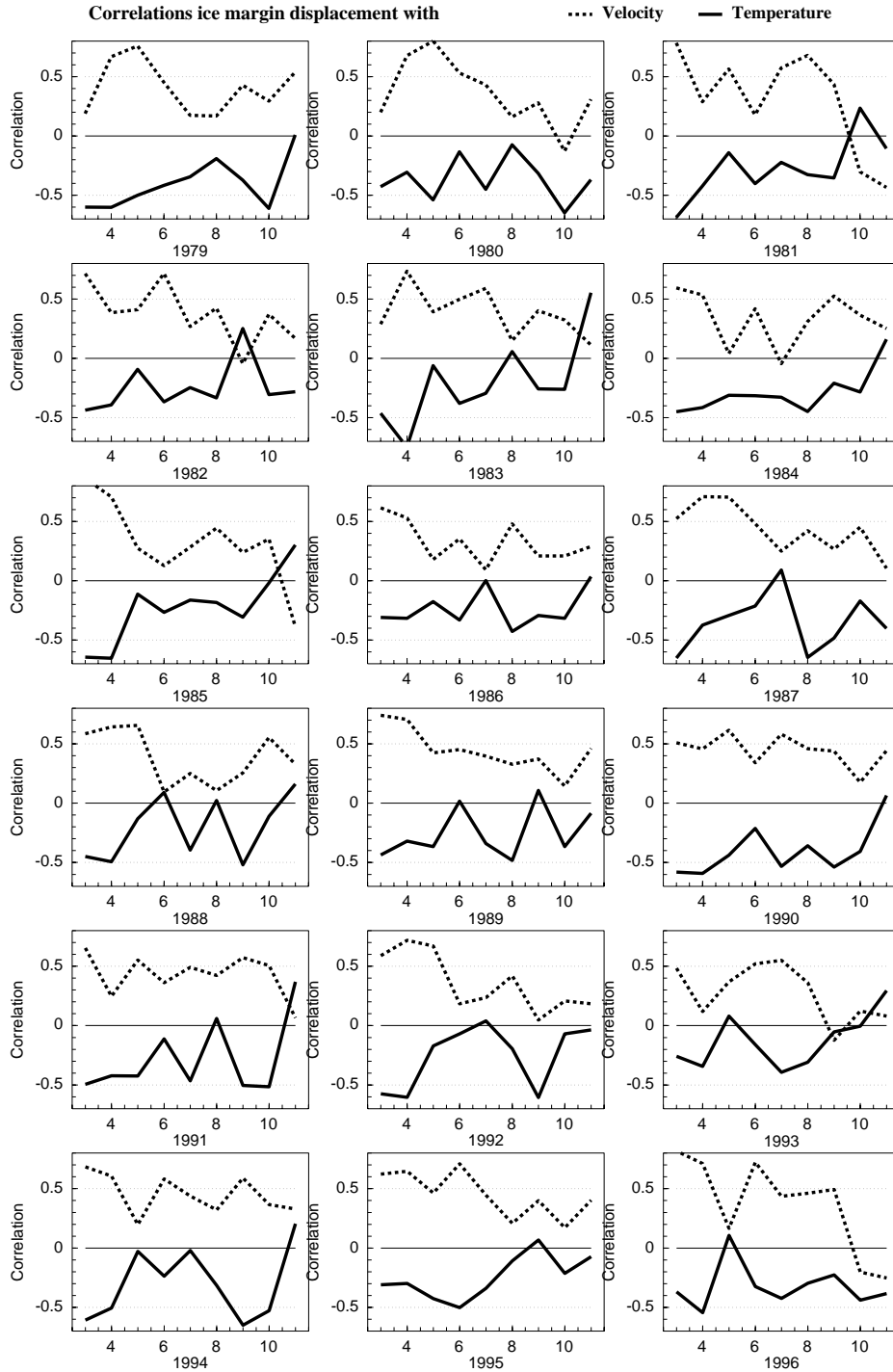


**Figure 6.18:** Correlation coefficients of annual ice motion displacement with temperature (solid line) and the meridional ice motion velocity component (dashed) for the months of March–November.

Here, correlations with ice motion and temperature are of the same magnitude of about 0.5. Since the above curves are monthly mean values and also spatially averaged around the ice margin, the dominating effect cannot be revealed in detail.

In the winter months, correlation coefficients become smaller, especially for the temperature. With generally lower temperatures, direct reaction of the ice margin extension to temperature changes is no longer predominant. The smallest values for both correlations can be found in spring. This is the time of rapid ice margin retreat, and temperature values above zero can be found around the ice edge.

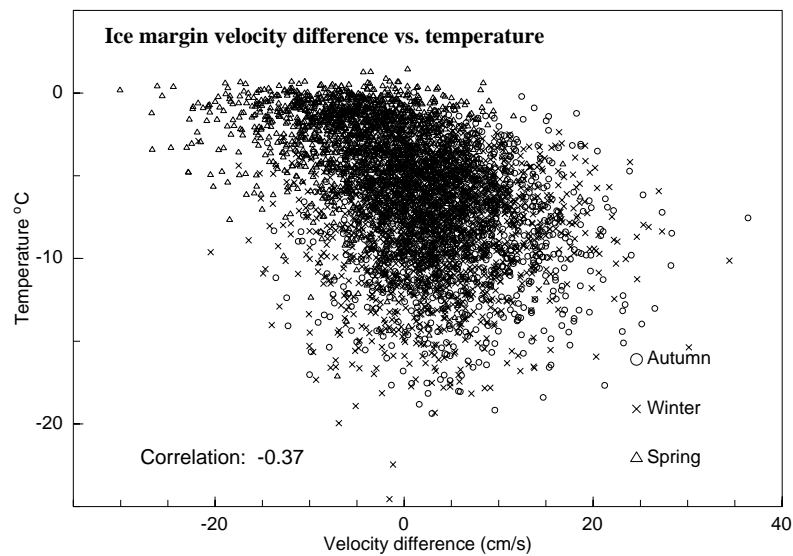


**Figure 6.19:** Correlation of monthly mean velocity difference between the ice margin itself and the SSMI ice motion vectors with temperatures. The three seasons autumn (circle), winter (cross), and spring (triangle) are marked by different symbols.

A direct reaction of the ice margin position to temperature increase cannot be seen in the data, since it is dependent on the amount and thickness of the existing ice. In the case of ice edge retreat, positive velocity correlation would imply a southward displacement of the ice edge with southerly ice motion and wind vectors. With larger amounts of ice at higher concentrations south of the ice edge, this motion is constrained by dynamic reasons.

The direct combination of the dynamic and thermodynamic effects is illustrated in Fig. 6.19. It compares the velocity differences between the ice margin itself and the SSMI ice motion vectors with the temperatures. High difference values mean that the ice edge moves faster northwards than driven by predominant drift patterns. The thermodynamic ice growth which accompanies lower temperatures is then expected to cause the main northward displacement. This is confirmed by a mean correlation of -0.37 in Fig. 6.19 for all seasons.

### Regional Difference of Correlations Coefficients

The regularly distributed regional differences of ice margin advance and retreat (Fig. 6.15) give rise to the question whether differences of the thermodynamic and dynamic influence are responsible for the ice margin displacement in different regions. The temperature distribution at the ice margin (not shown) yields similar temporal and spatial structures that repeat each year, leading to the assumption of generally predominant regional differences independent of the year and season. At each point around the ice margin, correlations of ice margin displacement with air temperature and meridional ice motion are calculated for the monthly values from 1979 to 1996 (Fig. 6.20). The corresponding values of temperature at the ice margin, mean meridional ice drift, meridional wind, and ice margin displacement are added for comparison.

Temperature correlation coefficients are generally negative, with smallest values of  $\rho$  being -0.7 in the Weddell region. Outside this region,  $\rho$  is around -0.5, with two exceptions in the central Ross Sea and close to the Antarctic peninsula. Velocity correlation is positive, with smaller mean values than the temperature correlation. Maximum values are found in the Ross and

Bellingshausen and Amundsen Seas. The negative and zero peaks around  $60^{\circ}\text{E}$  and  $150^{\circ}\text{E}$  are considered to be rather uncertain, since these are the two areas that suffer from coarse satellite velocity data.

The Ross Sea, the Weddell Sea, and, to a minor degree, the areas around the Amery ice shelf are the ones with strongest ice edge advance, which is indicated by the solid black line in the lower representation. The Eastern parts of the Ross Sea show increasing correlation coefficients for velocity and temperature correlation, whereas a reduction of these values is obtained for the central Ross Sea. Comparison with the dynamic and meteorological conditions given below shows almost the same ice margin displacement velocity for the whole Ross Sea.

Ice motion velocity which has the same magnitude as ice margin displacement always is somewhat smaller. The eastern part with the highest temperature correlations shows the lowest temperatures and also a regional maximum of meridional winds and ice motion. In these regions at Victoria Land's coast, cold catabatic winds from the continent bring colder air and mean northward motion of the ice. Compared to the other areas, the lowest temperatures exist at the ice margin. This enhances the thermodynamic formation of new ice and explains the positive difference between ice edge displacement and ice motion velocity.

Different mechanisms take place in the other big basin, the Weddell Sea. In the western part, strikingly low correlation values for temperature and ice motion occur.

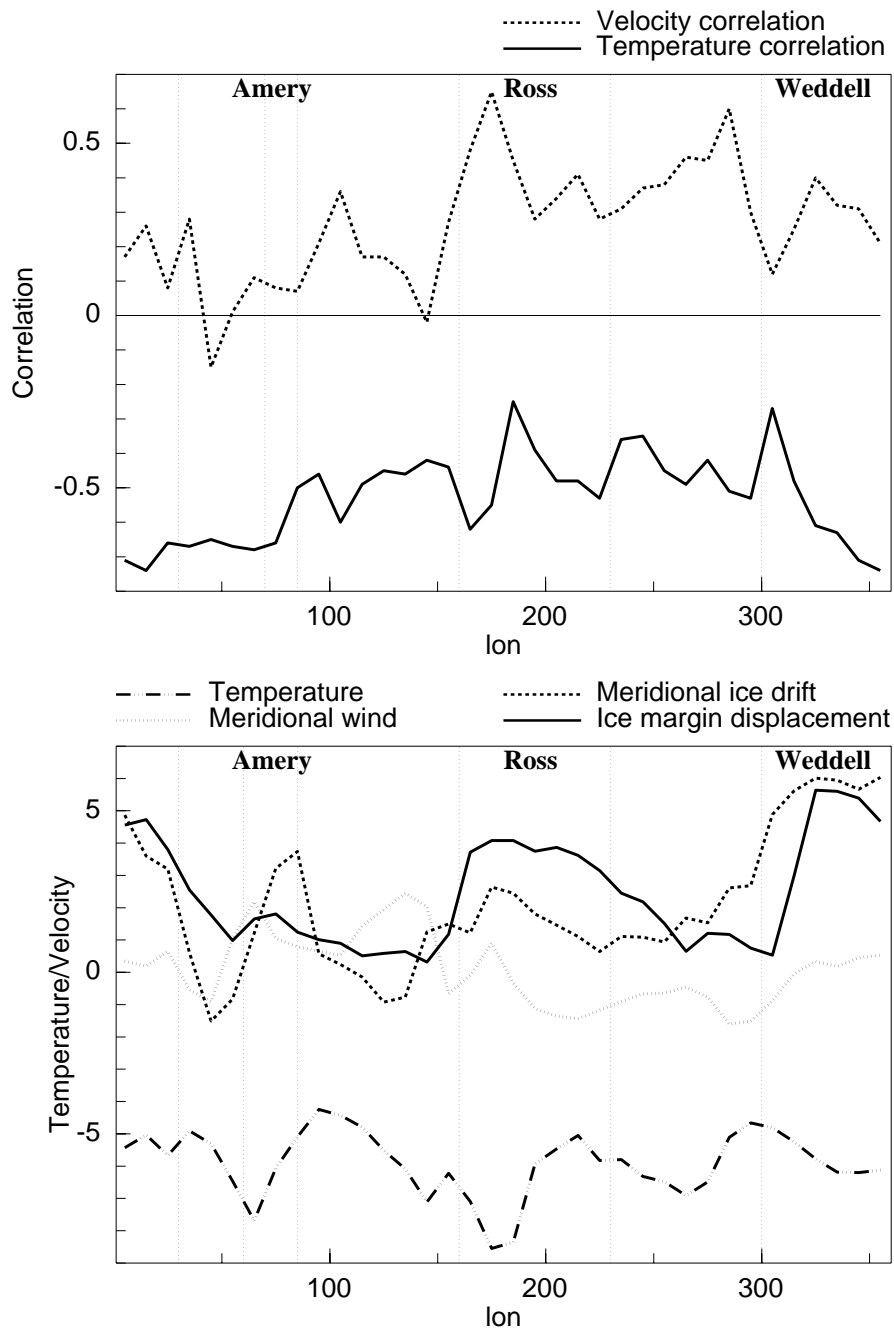


**Figure 6.20:** Correlation of monthly mean ice edge displacement with drift velocity and air temperatures (top). Corresponding values of temperature ( $^{\circ}\text{C}$ ) at the ice margin, mean meridional ice drift ( $\text{cm/s}$ ), meridional wind ( $\text{m/s}$ ), and ice margin displacement ( $\text{cm/s}$ ) are represented at the bottom.

Here, the multi-year ice restricts the quick reaction to wind forcing and temperature changes. This is also reflected by very small ice margin displacement velocities. For the Central and Eastern Weddell Sea, correlations become more evident, with the temperature correlation being largest. Also in the areas around the Amery ice shelf, ice motion is stronger than the ice edge displacement.

Region	Total	Autumn	Winter	Spring
300°-30°E Weddell	-0.47	-0.33	-0.09	-0.11
30°-80°E	-0.42	-0.34	-0.08	-0.21
80°-90°E Amery	-0.40	-0.19	-0.04	-0.05
90°-160°E	-0.33	-0.28	-0.11	-0.07
160°-210°E Ross	-0.26	-0.11	-0.05	0.19
210°-300°E	-0.23	-0.26	-0.08	0.03

**Table 6.3:** *Correlation between relative velocity (ice margin - meridional ice motion, according to Fig. 6.19) and temperature for regions with different ice margin displacement intensities.*

The different mechanisms underlying ice edge displacement in the Weddell, Amery, and Ross regions are also found when comparing relative velocity, e.g. the difference between ice margin displacement velocity and meridional ice motion component and temperature, as in Fig. 6.19. A general correlation of -0.37 describes the combination of dynamic/thermodynamic effects by indicating that larger velocity differences of the ice margin are negatively correlated with the temperature. Table 6.3 gives the same value, split up for the different regions and seasons as well as for the total period. In general, the values in the Weddell and Amery regions are -0.4 and more and obviously larger than in the Ross Sea, where correlation only reaches values around -0.2. The values for seasonal distribution (Fig. 6.18) indicate that reliable relationships between ice margin displacement and temperature and ice motion can only be established in autumn months. Here, as for the values for the whole years, the correlations continuously become smaller for positions further to the east.

## 7 Summary

The sea ice around Antarctica shows large regional, annual, and interannual fluctuations. They make it difficult to detect mean trends and clear relationships between cause and effect. In this context, the present thesis establishes relationships between atmospheric variability modes and fluctuations in the dynamics of the sea ice cover, with particular emphasis on interannual changes. The major feature of sea ice motion is the transport of ice mass between areas of thermodynamic growth and regions of melting, with significant impact on the radiation regime and the energy content of the atmosphere as well as on the thermohaline circulation of the ocean and the related dynamics.

Great improvement in satellite remote sensing of the Antarctic within the last years has provided access to over 20 years of data on sea ice, allowing calculations of ice motion and ice concentration with different resolutions for this period. The investigations are extended by the use of data from Antarctic buoys that cover selected regions of the Southern Ocean and deliver ice drift estimations of higher temporal and spatial resolution. The investigations presented here also profit from an advanced product, the *optimal interpolated* data that include satellite drift estimates as well as information from buoys, if available. In the first step of the investigations, an extensive intercomparison of this dataset with buoy measurements reveals local differences of satellite drift accuracies. Due to the different nature of both measurement principles, comparison was performed on different temporal and spatial scales. The main results reveal a good agreement of buoy and satellite data when compared within an interpolation radius of around 600 km. This is close to correlation lengths in the sea ice that are known for this region from other studies.

Results of seasonal and regional rms differences show a smaller error of OI data compared to uninterpolated drift vectors. Furthermore, they illustrate the large impact of different ice regimes on the accuracy of drift estimations. The mean rms error of OI data compared to buoys is 4.9 cm/s. The bias of -2.6 cm/s indicates that the mean ice motion is underestimated by satellite

measurements. Exceptions occur in the coastal areas with higher amounts of compressed, perennial ice. There, generally smaller rms errors and a positive or close-to-zero bias indicate that satellite drift seems to overestimate the real velocity of the ice. In these regions, the error is less depending on the season than in other regions. In most of the cases, except for the outer areas, there are decreasing errors and a smaller negative bias in the spring seasons.

Studies of the long-term trends of mean ice motion velocity, their zonal and meridional components and the mean variance reveal a significant decrease for most regions. Strongest negative velocity trends of  $-0.15$  cm/s/year occur in the regions of the Weddell Sea and the Indian Ocean, while the effect vanishes in the adjacent regions of the Pacific and the Eastern Ross and Amundsen Seas. A more striking feature is obtained for the trends of ice motion variance that show a strong decrease of up to  $-16$  cm<sup>2</sup>/s<sup>2</sup>/year and a similar regional distribution as the velocity trends. From extensive intercomparisons, artificial influences of the OI algorithm, different satellite sensors, and different satellite periods could be excluded. A similar negative trend of ice motion variance is also found for buoy data. Apart from the influence of superimposed atmospheric trends, changes in cyclone numbers and intensities deemed responsible, since most of the ice motion variance is caused by storm forcing.

The atmospheric trends and modes that may interact with changes of sea ice motion are investigated for different modes of variability. The Southern Annular Mode (SAM), the dominant mode in atmospheric variability, exhibits a positive trend for the last decades. The investigations of the corresponding ice motion fields for SAM  $> 0$  reveal a significant pattern that can be related directly to simultaneous atmospheric anomalies. Positive anomalies of zonal ice motion velocity that come along with the enhanced Westerlies are detected in the northern Weddell and Ross sectors, where the northward extent of the ice cover is largest. In the coastal areas of the Weddell Sea and along East Antarctica, negative anomalies and also a decreasing trend of zonal velocity occur.

On the interannual scale, ice motion also is influenced by the alternating pattern of the Southern Oscillation Index (SOI), the main impacts of

which take place in the Pacific sector. The general state of the SOI shows a slightly negative bias and the periodically occurring ENSO events yield large negative SOI values. The correlation coefficients of -0.3 for ice motion velocity and around -0.2 for variance with the SOI indicate enhanced drift velocities and higher monthly variances in phases with negative SOI. As the SOI is a regionally different parameter with its centre of action appearing as a pressure anomaly in the Amundsen and Bellingshausen Seas, an opposite behaviour of wind and SST anomalies can be found on both sides of this pressure centre. A similar behaviour is also obvious for correlations with the ice motion kinematics. At the forefront of a positive pressure anomaly according to an ENSO event, equatorward ice motion results in a divergent motion field. This assumption is confirmed by negative correlations of -0.37 for the zonal velocity and a positive correlation ( $\rho = 0.28$ ) for ice motion divergence. This, together with negative temperature anomalies, leads to an enhanced ice margin advance. On the back side of the pressure anomaly, the opposite pattern dominates, with ENSO forcing stronger poleward winds ( $\rho = 0.35$ ) and, thus, convergence in the ice motion field ( $\rho = -0.24$ ).

Investigations of the Antarctic Circumpolar Wave (ACW) reveal trans-antarctic coupling of ice motion in different regions. Propagating anomalies of atmospheric and oceanic patterns are also reflected by the fields of ice motion and variance. Apart from positive and negative anomalies of the meridional drift component that can be related to the established anomalies of sea ice extent, alternating anomalies propagating with periods of about 4 years can be found in drift velocity and, to a smaller amount, in variance, even in the inner region of the sea ice. Thus, the pattern of the ACW is also evident from ice motion data from the inner pack and not restricted to processes near the ice margin. Furthermore, the drift anomalies could be traced back to their origins several years ago and in different ocean basins, despite the annual configuration of sea ice and ice-free summer months. This is an indicator of sea ice motion being strongly involved in the coupled mechanisms of atmosphere and ocean that help the anomalies sustain for several years.

---

For the annual and semiannual periods, the variations of ice motion can be related to variations of wind forcing. Although the annual cycles of sea-level pressure generally show the typical 2-wave pattern according to the Antarctic Semiannual Oscillation (SAO), similar changes of ice drift velocity are only found when the same 2-wave pattern occurs in wind velocity. Classification results and frequency distribution of atmospheric patterns and drift velocity generally reveal a good agreement between ice and wind velocity. Furthermore, the results suggest that a combination of higher pressure amplitudes and higher temperatures, together with stronger wind forcing, is necessary for the pattern of SAO, with the accordingly higher variances, being detected in sea ice as well. Otherwise, internal stresses in the ice cover disable the fast reaction of the sea ice in the inner pack, while stronger ocean forcing dominates in the areas that are under the influence of the ACC. Both impacts suppress the formation of the 2-wave pattern in annual drift cycles.

When extending the investigations to the ice margin, significant correlations of changes of the sea ice extent and meridional velocity component are detected, but also great regional variations in the different ocean basins. A detailed comparison of the regional ice margin displacement with the effective ice motion velocity reveals local differences that indicate contributions from thermodynamic ice growth or melting. The annual cycles of correlation coefficients of ice margin displacement with temperature ( $\rho < 0$ ) and meridional drift ( $\rho > 0$ ) mainly show opposite patterns during the year, with a general decrease of the temperature correlation in winter and spring. The interaction of dynamic and thermodynamic influences results in a correlation coefficient of -0.37 when relating the relative velocity difference to the temperature. This means that higher difference velocities, e.g. ice margin displacements that are faster than meridional ice velocity, occur along with lower temperatures. This may be attributed to advection of colder air masses during cold air outbreaks with enhanced freezing.

The drift estimates from SMMR and SSMI provide valuable areawide timeseries that are necessary for long-term statistics on sea ice motion. Data of drifting buoys also are of particular importance in this context, since they

help establish the general relations of sea ice motion and wind forcing for specific regions and also allow for a validation of satellite measurements.

Summing up the results presented here, it may be stated that the sea ice dynamics play an important role in the complex system of interactions between the atmosphere and ocean, which was demonstrated on various timescales. This is a further step towards the understanding of single processes with a view to establish relations that are suitable for modelling the impacts of sea ice motion on the global climate.

## References

- Ackley, S. (1981). Sea-ice atmosphere interaction in the Weddell sea using drifting buoys. In *Sea Level, Ice and Climate Change*, pp. 177–181. Int. Assoc. of Hydrol. Sci., Oxford, England.
- Ackley, S. and E. Holt (1984). Sea ice data buoys in the Weddell Sea. CRRL Rep. 84-11, Cold Regions Res. and Eng. Lab., Hanover, N.H.
- Agnew, T., L. Hao, and T. Hirose (1997). Estimation of large scale sea ice motion from SSMI 85.5 GHz imagery. *Ann. Glaciol.* 24, 305–311.
- Allan, R., J. Lindsay, and D. Parker (1996). *El Nino, Southern Oscillation and climate variability*. CSIRO Publishing, Collingwood, Australia.
- Allison, I. (1989). Pack-ice drift off East Antarctica and some implications. *Ann. Glaciol.* 12, 1–8.
- Broeke, M. (2000). The Semiannual Oscillation and Antarctic climate. Part 4: A note on sea ice cover in the Amundsen and Bellingshausen Seas. *Int. J. Clim.* 20, 455–462.
- Cavalieri, D., P. Gloersen, and W. Campbell (1984). Determination of sea ice parameters with the NIMBUS-7 SMMR. *J. Geophys. Res.* 89, 5355–5369.
- Cavalieri, D., P. Gloersen, C. Parkinson, J. Comiso, and H. Zwally (1997). Observed hemispheric asymmetry in global sea ice changes. *Science* 278, 1104–1106.
- Colony, R. and A. Thorndike (1984). Estimate of the mean field of Arctic sea ice motion. *J. Geophys. Res.* 89(C6), 10.623 – 10.629.
- Comiso, J., D. Cavalieri, C. Parkinson, and P. Gloersen (1997). Passive microwave algorithms for sea ice concentration - A comparison of two techniques. *Rem. Sens. Environm.* 60(12), 357–384.
- Crane, D. and D. Bull (1990). Data report on the Weddell Ice Dynamics Experiment. Sea Ice Group Rep. 90-2, Scott Polar Res. Inst., Cambridge, England.

- Drinkwater, M. (1998). *Antarctic sea ice: physical processes, interactions and variability*, Volume IV of *Antarctic Research Series*, Chapter Active Microwave Remote Sensing Observations of Weddell Sea Ice, pp. 187–212. Washington, D.C.: American Geophysical Union.
- Drinkwater, M. and C. Kottmeier (1994). Satellite microwave radar- and buoy-tracked ice motion in the Weddell Sea during WWGS '92. In *IGARSS'94 Conference Proceedings*, pp. 153–155.
- Drinkwater, M., X. Liu, J. Maslanik, and C. Fowler (1999). Optimal analysis products combining buoy trajectories and satellite-derived ice-drift fields. In *International Programme for Antarctic Buoys IPAB Biennial Meeting Report*, WCRP Report, World Climate Research Program, Geneva, Switzerland, pp. 1–11.
- Drinkwater, M. and S. Venegas (2001). Interannual variations in Antarctic atmosphere-ice-ocean coupling. *Earth Observation Quarterly* 69, 14–17.
- Eisen, O. and C. Kottmeier (2000). On the importance of leads in sea ice to the energy balance and ice formation in the Weddell Sea. *J. Geophys. Res.* 105(C6), 14045–14060.
- Emery, W., C. Fowler, and J. Maslanik (1997). Satellite-derived maps of Arctic and Antarctic sea ice motion: 1988 to 1994. *J. Geophys. Res.* 24, 897–900.
- Fahrmeir, F., A. Hamerle, and G. Tutz (1996). *Multivariate statistische Verfahren*. Berlin, New York: Walter de Gruyter.
- Geiger, C., W. Hibler III, and S. Ackley (1998). Large-scale sea ice drift and deformation: Comparison between models and observations in the western Weddell Sea during 1992. *J. Geophys. Res.* 103(C10), 21893 – 21913.
- Geiger, C., Y. Zhao, A. Liu, and S. Hakkinen (2000). Large-scale comparison between buoys and SSM/I drift and deformation in the Eurasian basin during winter 1992-1993. *J. Geophys. Res.* 105(C2), 3357–3368.
- Gloersen, P. and W. White (2001). Reestablishing the circumpolar wave in sea ice around Antarctica from one winter to the next. *J. Geophys.*

- Res. 106*(15), 4391–4396.
- Heil, P. and I. Allison (1999). The pattern and variability of Antarctic sea ice drift in the Indian and Western Pacific sectors. *J. Geophys. Res. 104*(C7), 15789–15802.
- Heil, P., C. Fowler, J. Maslanik, W. Emery, and I. Allison (2001). A comparison of East Antarctic sea-ice motion derived using drifting buoys and remote sensing. *Ann. Glaciol. 33*, 139–144.
- Hines, K., D. Bromwich, and G. Marshall (2000). Artificial surface pressure trends in the NCEP/NCAR reanalysis over the Southern Ocean and Antarctica. *J. Climate 13*, 3940–3952.
- Hoeber, H. (1991). Sea ice dynamics in the Weddell Sea in winter. *Ann. Glaciol. 15*, 9–16.
- Hollinger, J., R. Lo, and G. Poe (1987). *Special Sensor Microwave/Imager User's Guide*. Naval Research Laboratory, Washington D.C.
- Jacobs, S. and J. Comiso (1997). Climate variability in the Amundsen and Bellingshausen Seas. *J. Climate 10*, 697–709.
- Kalnay, E., M. Kanamitsu, R. Kistler, W. Collins, D. Deaven, L. Gandin, M. Iredell, S. Saha, G. White, J. Woollen, Y. Zhu, M. Chelliah, W. Ebisuzaki, W. Higgins, J. Janowiak, K. Mo, C. Ropelewski, J. Wang, A. Leetmaa, R. Reynolds, R. Jenne, and D. Joseph (1996). The NMC/NCAR 40-year reanalysis project. *Bull. Am. Meteorol. Soc. 77*, 437–471.
- Kanamitsu, M., W. Ebisuzaki, J. Woolen, J. Potter, and M. Fiorino (2002). NCEP/DOE AMIP-II reanalysis (R-2) . *Bull. Am. Meteorol. Soc. 83*, 1631–1643.
- Kistler, R., E. Kalnay, W. Collins, S. Saha, G. White, J. Woollen, W. E. a. M. K. M. Chelliah, V. Kousky, H. Dool, R. Jenne, and M. Fiorino (2001). The NCEP/NCAR 50-year reanalysis. *Bull. Am. Meteorol. Soc. 82*, 247–268.
- Kottmeier, C., S. Ackley, E. Andreas, D. Crane, H. Hoeber, J. Kong, J. Launinien, D. Limbert, D. Martinson, R. Roth, L. Sellmann, P. Wad-

- hams, and T. Vihma (1997). Wind, temperature and ice motion statistics in the Weddell Sea. WMO/TD, WMO/ICSU/IOC, World Climate Research Programme (WCRP), International Programme for Antarctic Buoys (IPAB).
- Kottmeier, C., K. Frey, M. Hasel, and O. Eisen (2003). Sea ice growth in the eastern Weddell Sea in winter. *J. Geophys. Res.* 108(C4), 3125.
- Kottmeier, C. and J. Lüdemann (1996). Meereisbojen 1986 - 1995, Berichte aus dem Fachbereich Physik 69. Technische Dokumentation, Alfred-Wegener-Institut für Polar- und Meeresforschung, Bremerhaven, Germany.
- Kottmeier, C., J. Olf, W. Frieden, and R. Roth (1992). Wind forcing and ice motion in the Weddell Sea. *J. Geophys. Res.* 97(D18), 20373–20383.
- Kottmeier, C. and L. Sellmann (1996). Atmospheric and oceanic forcing of Weddell Sea ice motion. *J. Geophys. Res.* 101(C9), 20809–20824.
- Kwok, R. (2000). Recent changes in Arctic ocean sea ice motion associated with the North Atlantic Oscillation. *Geophys. Res. Lett.* 27, 775–778.
- Kwok, R. and J. Comiso (2002a). Southern Ocean climate and sea ice anomalies associated with the Southern Oscillation. *J. Climate* 15(3), 478–501.
- Kwok, R. and J. Comiso (2002b). Spatial patterns of variability in Antarctic surface temperature: Connections to the Southern Hemisphere Annular Mode and the Southern Oscillations. *Geophys. Res. Lett.* 29(40), 30–34.
- Kwok, R., J. Curlander, R. McConnell, and S. Pang (1990). An ice-motion tracking system at the Alaska SAR Facility. *IEEE J. Oceanic Eng.* 15(1), 44–54.
- Kwok, R., A. Schweiger, D. Rothrock, S. Pang, and C. Kottmeier (1998). Assessment of sea ice motion from sequential passive microwave observations with ERS and buoy ice motions. *J. Geophys. Res.* 103(C4), 8191–8213.

- Lefebvre, W., H. Goosse, R. Timmermann, and T. Fichefet (2004). Influence of the Southern Annular Mode on the sea ice-ocean system. *J. Geophys. Res.* 109(C09006), doi:10.1029/2004JC002403.
- Lemke, P. and T. Martin (2001). SEALION - Sea ice in the Antarctic, linked with ocean-atmosphere forcing. Technical report, Scientific Report EU Contract No: ENV 4-CT97-0415 (DG 12 -ESCY).
- Leppäranta, M. (2005). *The drift of sea ice*. Springer Verlag Berlin Heidelberg New York, Published in association with Praxis Publishing, Chichester UK.
- Liu, A. and D. Cavalieri (1998). On sea ice drift from the wavelet analysis of DMSP SSM/I data. *Int. J. Remote Sens.* 19(7), 1415–1423.
- Martinson, D. and C. Wamser (1990). Ice drift and momentum exchange in winter Antarctic pack ice. *J. Geophys. Res.* 95, 1741–1755.
- Maslanik, J., T. Agnew, M. Drinkwater, W. Emery, C. Fowler, R. Kwok, and A. Liu (1998). Summary of ice-motion mapping using passive microwave data. Report prepared for the Polar Data Advisory Group, NASA Snow and Ice Distributed Active Archive Center Special Pub. 8, National Snow and Ice Data Center, Boulder, Colorado.
- Heygster, G., L. Pedersen, J. Turner, C. Thomas, T. Hunewinkel, H. Schottmueller, and T. Viehoff (1996). PELICON - Project for estimation of long-term variability of ice concentration. Tech. Report Contract EV5V-CT93-0268(DG 12 DTEE), European Community (EC).
- McPhee, M., C. Kottmeier, and J. Morison (1999). Ocean heat flux in the central Weddell Sea during winter. *Journal of Physical Oceanography* 29, 1166–1179.
- Meehl, G., J. Hurrell, and H. van Loon (1998). A modulation of the mechanism of the semiannual oscillation in the Southern Hemisphere. *Tellus* 50A, 442–450.
- Meinardus, W. (1938). *Handbuch der Klimatologie*, Volume IV, Chapter Klimakunde der Antarktis, pp. 1–130. Borntäger, Berlin.
- Nan, S. and J. Li (2003). The relationship between summer precipitation

- in the Yangtze River valley and the previous Southern Hemisphere Annular Mode. *Geophys. Res. Lett.* 30(24), 2266.
- Padman, L. and C. Kottmeier (2000). High-frequency ice motion and divergence in the Weddell Sea. *J. Geophys. Res.* 105, 3379–3400.
- Parkinson, C. (1998). *Antarctic sea ice - physical processes, interactions and variability*, Volume 74 of *Antarctic Research Series*, Chapter Length of the sea ice season in the Southern Ocean, 1988-1994, pp. 173–186. American Geophysical Union, Washington, D.C.
- Peterson, R. and W. White (1998). Slow oceanic teleconnections linking the Antarctic Circumpolar Wave with the tropical El Niño-Southern Oscillation. *J. Geophys. Res.* 103(12), 24573–24584.
- Rasmussen, E. A. and J. Turner (2003). *Polar Lows - Mesoscale weather systems in the polar regions*. Cambridge University Press.
- Schmitt, C., C. Kottmeier, S. Wassermann, and M. Drinkwater (2004). Atlas of antarctic sea ice drift. [www.imk.uni-karlsruhe.de/seaiceatlas](http://www.imk.uni-karlsruhe.de/seaiceatlas).
- Simmonds, I. and T. Jacka (1995). Relationships between the interannual variability of Antarctic sea ice and the Southern Oscillation. *J. Climate* 8, 637–647.
- Simmonds, I., K. Keay, and E. Lim (2003). Synoptic activity in the seas around Antarctica. *Monthly Weather Review* 131(2), 272–288.
- Stammerjohn, S., M. Drinkwater, R. Smith, and X. Liu (2003). Ice-atmosphere interactions during sea-ice advance and retreat in the western Antarctic Peninsula region. *J. Geophys. Res.* 108(C10), 3329–3344.
- Thomas, C. H. (1998). Longtime analysis of Antarctica’s sea ice from passive microwave data. Reports on Polar Research 284, Alfred-Wegener-Institut fuer Polar- und Meeresforschung (AWI).
- Thompson, D. and J. Wallace (2000). Annular modes in the extratropical circulation. Part I: Month-to-month variability. *J. Climate* 13, 1000–1016.
- Thorndike, A. and R. Colony (1982). Sea ice motion in response to geostrophic winds. *J. Geophys. Res.* 87, 5845–5852.

- Timmermann, R., P. Lemke, and C. Kottmeier (1999). Formation and maintenance of a polynya in the Weddell Sea. *Journal of Physical Oceanography* 29, 1251–1264.
- Turner, J. (2004). Review: The ElNino-Southern Oscillation and Antarctica. *Int. J. Clim.* 24, 1–31.
- Turner, J., S. Harangozo, J. King, W. Connolley, T. Lachlan-Cope, and G. Marshall (2003). An exceptional winter sea ice retreat/advance in the Bellingshausen Sea, Antarctica. *Atmos. Ocean.* 41(2), 171–185.
- van Loon, H. (1967). The half-yearly oscillations in middle and high southern latitudes and the coreless winter. *J. Atmos. Sci.* 24, 472–486.
- Venegas, S. (2003). The Antarctic Circumpolar Wave: a combination of two signals? *J. Climate* 16, 2509–2525.
- Venegas, S. and M. Drinkwater (2001). Sea ice, atmosphere and upper ocean variability in the Weddell Sea, Antarctica. *J. Geophys. Res.* 106(15), 16747–16766.
- Venegas, S., M. Drinkwater, and G. Shaffer (2001). Coupled oscillations in Antarctic sea ice and atmosphere in the South Pacific sector. *Geophys. Res. Lett.* 28, 3301–3304.
- Vihma, T. and J. Launiainen (1993). Ice drift in the Weddell Sea in 1990–1991 as tracked by a satellite buoy. *J. Geophys. Res.* 98(C8), 14471–14485.
- Vihma, T., J. Launiainen, and J. Uotila (1996). Weddell Sea ice drift: kinematics and wind forcing. *J. Geophys. Res.* 101(C8), 18279–18296.
- Wadhams, P., C. Sear, D. Crane, M. Rowe, S. Morrison, and D. Limbert (1989). Basin-Scale ice motion and deformation in the Weddell Sea during winter. *Ann. Glaciol.* 12, 178–186.
- Walland, D. and I. Simmonds (1999). Baroclinity, meridional temperature gradients, and the Southern Semiannual Oscillation. *J. Climate* 12, 3376–3382.
- Watkins, A. and I. Simmonds (2000). Current trends in Antarctic sea ice: the 1990s impact on a short climatology. *J. Climate* 13(25), 4441–4451.

- Weeks, W. (1989). *Physics of ice-covered seas*, Volume 1, Chapter Growth conditions and structure and properties of sea ice, pp. 25–204. Helsinki University Press.
- White, W., S. Chen, and R. Peterson (1998). The Antarctic Circumpolar Wave: A beta-effect in ocean-atmosphere coupling over the Southern Ocean. *Journal of Physical Oceanography* 28, 2345–2361.
- White, W., P. Gloersen, and I. Simmonds (2004). Tropospheric response in the Antarctic Circumpolar Wave along the sea ice edge around Antarctica. *J. Climate* 17, 2765–1779.
- White, W. and R. Peterson (1996). An Antarctic Circumpolar Wave in surface pressure, wind, temperature, and sea ice extent. *Nature* 380, 699–702.
- White, W., C. Yi, and T. Chang-Kou (1998). Coupling of biennial oceanic Rossby Waves with the overlying atmosphere in the Pacific basin. *Journal of Physical Oceanography* 28(6), 1236–1251.
- Wilks, D. S. (1995). *Statistical methods in atmospheric sciences*, Volume 59 of *International Geophysics Series*. Academic Press.
- WMO (1970). The WMO sea-ice nomenclature. TP-145, with later supplements 259, World Meteorological Organization, Geneva.
- Yuan, X. (2004). ENSO-related impacts on Antarctic sea ice: a synthesis of phenomenon and mechanisms. *Antarctic Science* 16(4), 415–425.
- Yuan, X. and D. Martinson (2001). Antarctic sea ice extent variability and its global connectivity. *J. Climate* 13, 1697–1717.
- Zwally, H. J., J. C. Comiso, C. L. Parkinson, D. J. Cavalieri, and P. Gloersen (2000). Current trends in Antarctic sea ice: the 1990s impact on a short climatology. *Variability of Antarctic sea ice 1979-1998 C5*(107), doi:10.1029/2000JC000733.

## A Appendix

Coloured version of all figures can be found in the PDF-document under:  
www.imk.uni-karlsruhe.de

### A.1 Calculation of Covariance Ellipses

The probability density function for normally distributed variables (Fahrmeir et al., 1996) is given as :

$$\Phi(\vec{x}) = k \exp\left[-\frac{1}{2}(\vec{x} - \vec{a})^T B(\vec{x} - \vec{a})\right] \quad (\text{A.1})$$

with the vector  $\vec{x} = (x_1, x_2)^T$  and the expected values  $\vec{a} = (a_1, a_2)^T$ . The matrix B is the inverse of the covariance matrix C

$$C = \begin{pmatrix} \sigma_1^2 & \text{cov}(x_1, x_2) \\ \text{cov}(x_1, x_2) & \sigma_2^2 \end{pmatrix}$$

including the standard deviations  $\sigma_1$  and  $\sigma_2$  and the covariance of  $x_1$  and  $x_2$ :

$$B = C^{-1} = \frac{1}{\sigma_1^2 \sigma_2^2 - \text{cov}(x_1, x_2)^2} \begin{pmatrix} \sigma_1^2 & \text{cov}(x_1, x_2) \\ \text{cov}(x_1, x_2) & \sigma_2^2 \end{pmatrix}$$

With the correlation coefficient  $\rho = \frac{\text{cov}(x_1, x_2)}{\sigma_1 \sigma_2}$ , B can be expressed as:

$$B = \frac{1}{1 - \rho^2} \begin{pmatrix} \sigma_1^{-2} & -\frac{\rho}{\sigma_1 \sigma_2} \\ -\frac{\rho}{\sigma_1 \sigma_2} & \sigma_2^{-2} \end{pmatrix} .$$

For lines with the same probability density, the exponent of (A.1) has to be constant, leading to the equation:

$$\frac{1}{1 - \rho^2} \left[ \frac{(x_1 - a_1)^2}{\sigma_1^2} - 2\rho \frac{(x_1 - a_1)(x_2 - a_2)}{\sigma_1 \sigma_2} + \frac{(x_2 - a_2)^2}{\sigma_2^2} \right] = c \quad (\text{A.2})$$

For  $c = 1$ , this is the function of an ellipse with the origin  $(a_1, a_2)$  and an angle  $\alpha$  between the principle axis and the coordinate axis.

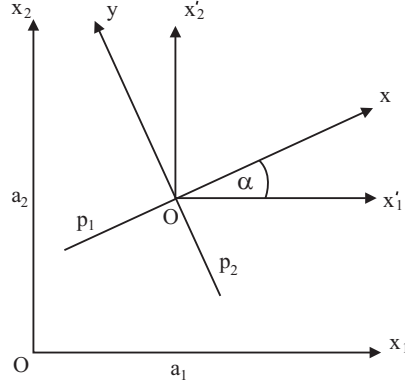


**Figure A.1:** *The different coordinate systems.*

Coordinate transformation to the origin of the ellipse with  $x'_1 = x_1 - a_1$  and  $x'_2 = x_2 - a_2$  leads to

$$\frac{1}{1 - \rho^2} \left[ \frac{x_1'^2}{\sigma_1^2} - 2\rho \frac{x_1' x_2'}{\sigma_1^2 \sigma_2^2} + \frac{x_2'^2}{\sigma_2^2} \right] = 1 \quad . \quad (\text{A.3})$$

Turning around  $\alpha$  transforms the coordinates in the main axis system of the ellipse

$$\begin{pmatrix} x \\ y \end{pmatrix} = \underbrace{\begin{pmatrix} \cos \alpha & \sin \alpha \\ -\sin \alpha & \cos \alpha \end{pmatrix}}_A \begin{pmatrix} x'_1 \\ x'_2 \end{pmatrix} \quad .$$

With the symmetric transformation matrix  $A^{-1} = A^T$ , the inverse transformation is:

$$\begin{pmatrix} x'_1 \\ x'_2 \end{pmatrix} = \begin{pmatrix} \cos \alpha & -\sin \alpha \\ \sin \alpha & \cos \alpha \end{pmatrix} \begin{pmatrix} x \\ y \end{pmatrix} \quad (\text{A.4})$$

With the new coordinates  $x$  and  $y$ , Eq. (A.3) becomes

$$\frac{1}{1 - \rho^2} \left[ \frac{(x \cos \alpha - y \sin \alpha)^2}{\sigma_1^2} + \frac{(x \sin \alpha + y \cos \alpha)^2}{\sigma_2^2} \right] - \frac{2\rho(x \cos \alpha - y \sin \alpha)(x \sin \alpha + y \cos \alpha)}{\sigma_1^2 \sigma_2^2 (1 - \rho^2)} =$$

$$\begin{aligned}
&= \frac{1}{1-\rho^2} \left[ x^2 \left( \frac{\cos^2 \alpha}{\sigma_1^2} - \frac{2\rho \sin \alpha \cos \alpha}{\sigma_1 \sigma_2} + \frac{\sin^2 \alpha}{\sigma_2^2} \right) \right] + \\
&\quad \frac{1}{1-\rho^2} \left[ y^2 \left( \frac{\sin^2 \alpha}{\sigma_1^2} + \frac{2\rho \sin \alpha \cos \alpha}{\sigma_1 \sigma_2} + \frac{\cos^2 \alpha}{\sigma_2^2} \right) \right] + \\
&\quad + \frac{2xy}{1-\rho^2} \underbrace{\left( \frac{\rho \sin^2 \alpha}{\sigma_1 \sigma_2} - \frac{\rho \cos^2 \alpha}{\sigma_1 \sigma_2} - \frac{\sin \alpha \cos \alpha}{\sigma_1^2} + \frac{\sin \alpha \cos \alpha}{\sigma_2^2} \right)}_{\stackrel{!}{=} 0} = 1 \quad .
\end{aligned}$$

This may be compared with the standard equation for an ellipse

$$\frac{x^2}{p_1^2} + \frac{y^2}{p_2^2} = 1. \quad (\text{A.5})$$

With the semi-major axes  $p_1$  and  $p_2$ , the single coefficients become

$$p_1^2 = \frac{1-\rho^2}{\left( \frac{\cos^2 \alpha}{\sigma_1^2} - \frac{2\rho \sin \alpha \cos \alpha}{\sigma_1 \sigma_2} + \frac{\sin^2 \alpha}{\sigma_2^2} \right)} \quad (\text{A.6})$$

$$p_2^2 = \frac{1-\rho^2}{\left( \frac{\sin^2 \alpha}{\sigma_1^2} + \frac{2\rho \sin \alpha \cos \alpha}{\sigma_1 \sigma_2} + \frac{\cos^2 \alpha}{\sigma_2^2} \right)} \quad (\text{A.7})$$

$$\alpha = \frac{1}{2} \arctan \left( \frac{2\rho \sigma_1 \sigma_2}{\sigma_1^2 - \sigma_2^2} \right) \quad . \quad (\text{A.8})$$

This is the equation of the covariance ellipses for two normally distributed variables. To illustrate the meaning, three ellipses with the same standard deviations  $\sigma_1$  and  $\sigma_2$  are compared (Fig. A.2). They are all positioned within the same rectangle that is determined by the length of  $\sigma_1$  and  $\sigma_2$  and the point  $(a_1, a_2)$  and have different main axis systems, rotated by the angle  $\alpha$ . The magnitude of this angle depends on  $\rho$  and varies between  $-90^\circ$  and  $90^\circ$ , with negative values of  $\rho$  causing negative rotation angles and an inclination of the ellipse to the left.

The correlation coefficient  $\rho$  specifies the covariance of the two variables, normalised by the single standard deviations. For  $\rho = 0$ , there is no relation between the two variables, the scatter plot of the probability density distribution becomes a circle and the rotation angle  $\alpha$  is  $0^\circ$ . A maximum correlation

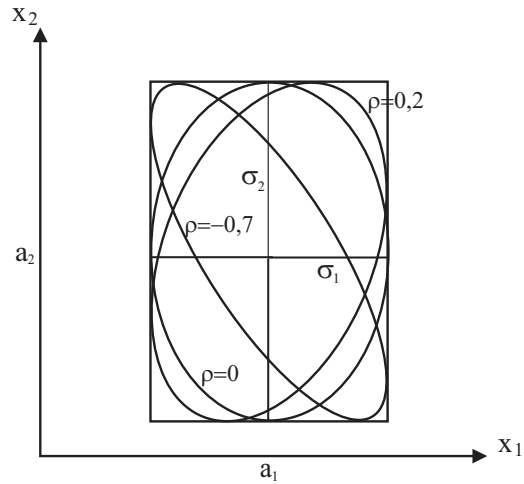


**Figure A.2:** Example of three ellipses with the same standard deviations  $\sigma_i$  and different correlation coefficients.

of both variables leads to a straight line ( $\rho = \pm 1$ ) that lies diagonally in the rectangle. Ellipses with various aspect ratios and slopes result for correlation values within the interval  $[0, 1]$  and different magnitudes of  $\sigma_1$  and  $\sigma_2$ .

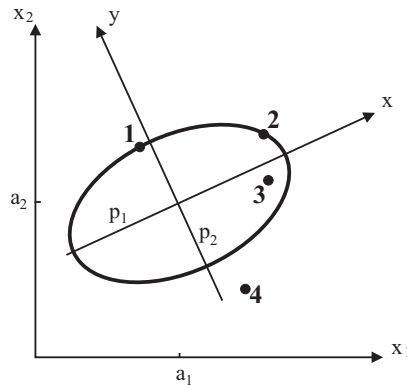


**Figure A.3:** Relative probability for different points.

It follows from Eq. A.3 that the other lines of equal probability density are also ellipses. They are concentric with the covariance ellipse and inside (outside) these for smaller (larger) probability densities. The points 1 and 2, that lie on the ellipse in Fig. A.3 have the same probability ( $P_1 = P_2 = P_e$ ),

although they have different distance to the centre. In contrast to this, point 3 has a larger probability than point 4 ( $P_3 > P_e, P_4 < P_e$ ).

To describe the ellipse in the new  $(x,y)$  coordinate system, the components are expressed as:

$$\begin{aligned}x &= r(\Phi) \cos \Phi \\y &= r(\Phi) \sin \Phi\end{aligned}$$

with  $0 \leq \Phi \leq 2\pi$  and  $r(\Phi) \geq 0$ . With the equation for the ellipse (A.5), this leads to:

$$r^2(\Phi) \left( \frac{\cos^2 \Phi}{p_1^2} + \frac{\sin^2 \Phi}{p_2^2} \right) = 1 \quad (\text{A.9})$$

or

$$r(\Phi) = \left( \frac{\cos^2 \Phi}{p_1^2} + \frac{\sin^2 \Phi}{p_2^2} \right)^{-\frac{1}{2}}. \quad (\text{A.10})$$

The coordinate transformation (A.4) turns the system by the angle  $-\Phi$  into the  $(x'_1, x'_2)$  system. The equation for the ellipse (A.2) may be transformed with  $x_1 = x'_1 + a_1, x_2 = x'_2 + a_2$  into polar coordinates:

$$x_1(\Phi) = r(\Phi)(\cos \alpha \cos \Phi - \sin \alpha \sin \Phi) + a_1 \quad (\text{A.11})$$

$$x_2(\Phi) = r(\Phi)(\sin \alpha \cos \Phi - \cos \alpha \sin \Phi) + a_2 \quad (\text{A.12})$$

## A.2 Details for Comparison in 4.2

Name convention for satellite data:

**1day:** displacement vectors for dd to dd+1, every day

**2day:** displacement vectors for dd to dd+2, every second day

Name convention for buoy data:

**b1:** fixed 1-day mean, containing of all 8 values per day

d1d1d1d1d1d1 d2d2d2d2d2d2 d3d3d3d3d3d3 d4d4d4d4d4d4  
 |---mean d1---|---mean d2---|---mean d3---|---mean d4---|

**b3:** sliding mean over 3 days to filter out high frequencies and to match the time span of the satellite 2day data.

d1d1d1d1d1d1 d2d2d2d2d2d2 d3d3d3d3d3d3 d4d4d4d4d4d4  
 |----- mean d1 -----|  
 |----- mean d2 -----|

Name convention for seasons:

**A** (March, April, May)  $\Rightarrow$  Autumn

**B** (June, July, August )  $\Rightarrow$  Winter

**C** (September, October, November)  $\Rightarrow$  Spring

Name convention for regions:

**Coast** (close to the Antarctic peninsula)  $\Rightarrow$  Group1 (from Fig. 4.1)

**Center** (Central Weddell Sea)  $\Rightarrow$  Group2 (from Fig. 4.1)

**All** (all buoy data of the year)  $\Rightarrow$  Group1 + Group2 + Others

### A.3 Error Values for Comparison in 4.2

Error values from satellite and buoy drift estimates for various regions:

	Total rms	Autumn rms	Winter rms	Spring rms
Coast1	3.63	4.54	3.55	2.60
Coast2	4.37	5.09	3.94	3.88
Ecoast	10.08	9.97	10.20	99.00
Center	6.29	6.36	4.69	5.99
Ross	5.21	5.26	5.02	4.11
East1	8.20	11.38	8.06	6.64
East2	9.84	12.18	8.16	8.95
West	9.01	14.29	1.90	4.11
East1out	10.70	99.00	8.88	10.81
East2out	13.04	99.00	99.00	13.05
Westout	13.22	15.13	9.13	13.02
	Total bias	Autumn bias	Winter bias	Spring bias
Coast1	-0.99	-2.59	-0.14	0.00
Coast2	-0.90	-3.70	-0.81	-0.39
Ecoast	-2.07	-9.72	5.57	99.00
Center	-3.42	-3.57	-2.28	-3.01
Ross	-1.34	-1.15	-1.72	-0.42
East1	-5.59	-11.29	-5.21	-3.61
East2	-8.39	-11.21	-6.53	-7.29
West	-6.01	-12.01	1.42	-0.42
East1out	-9.61	99.00	-7.97	-9.41
East2out	-12.22	99.00	99.00	-12.22
Westout	-12.76	-14.73	9.13	-12.65

**Table A.1:** Summary of satellite-buoy rms and bias for all seasons and regions. Value 99.00 indicates that no data are available for that season.

## A.4 Timeseries of Drift Components for 5.2.2

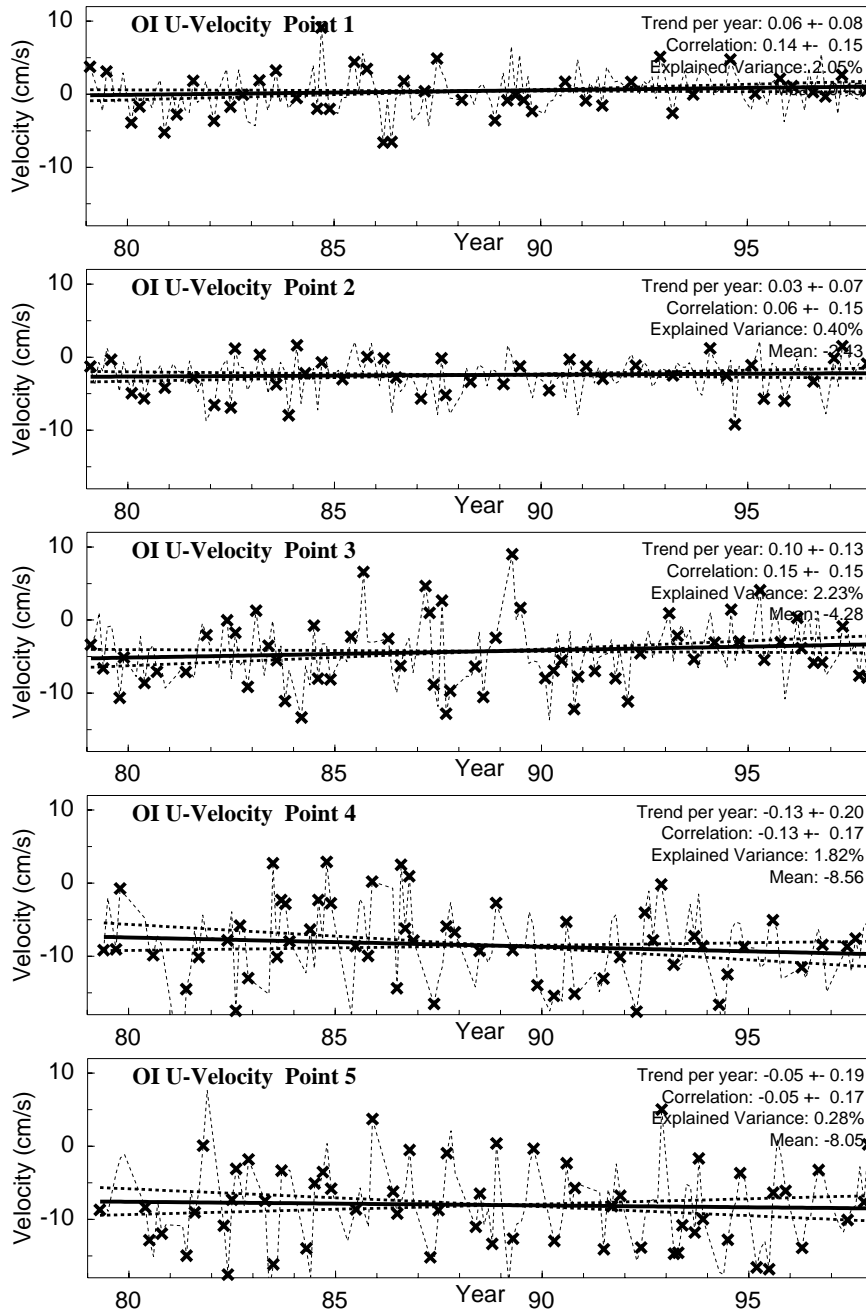


Figure A.4: Monthly mean zonal drift velocity at points 1 - 5. The black line indicates the mean trend with its confidence intervals as dashed lines.

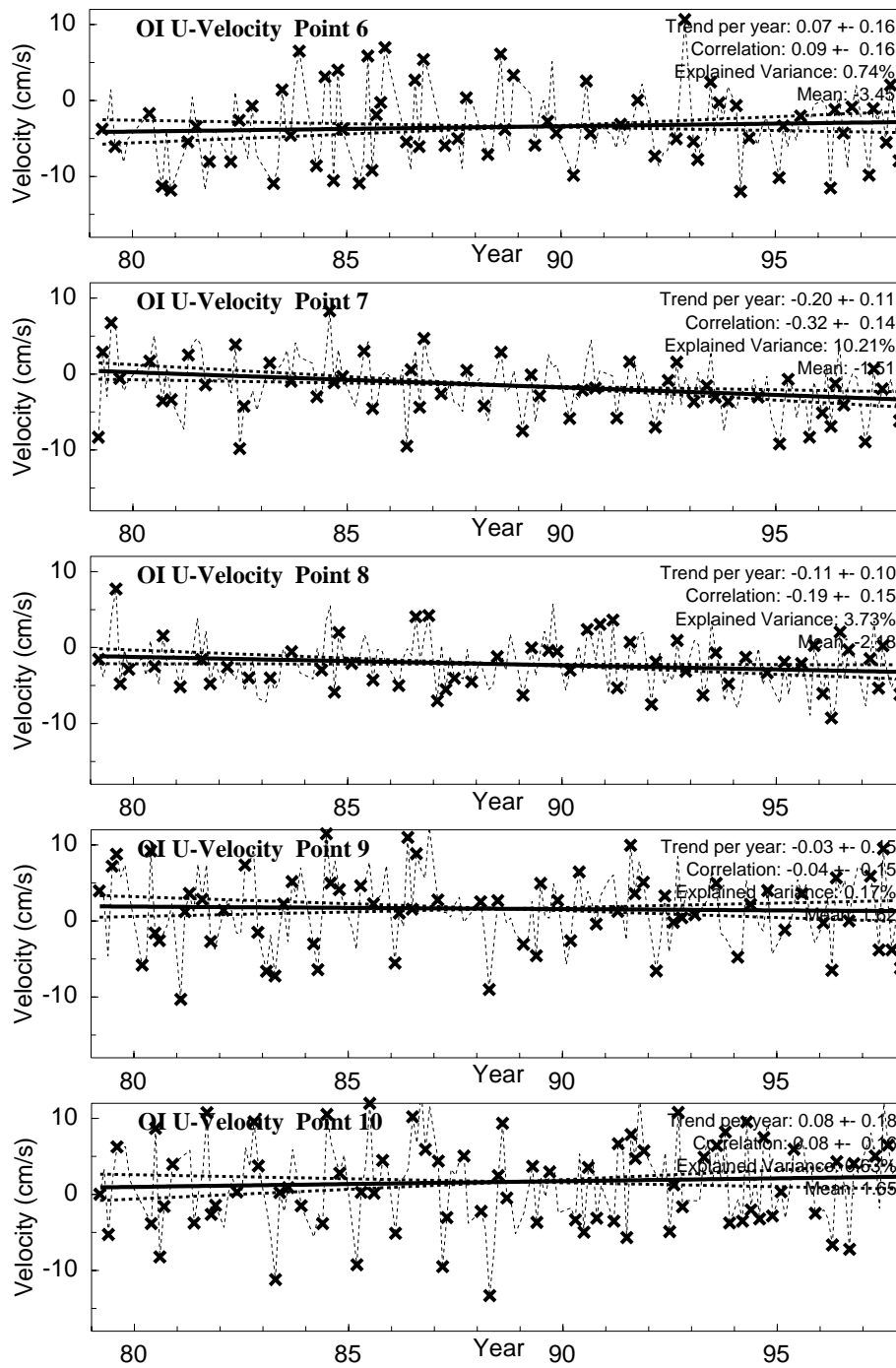


Figure A.5: Monthly mean zonal drift velocity at points 6 - 10. The black line indicates the mean trend with its confidence intervals as dashed lines.

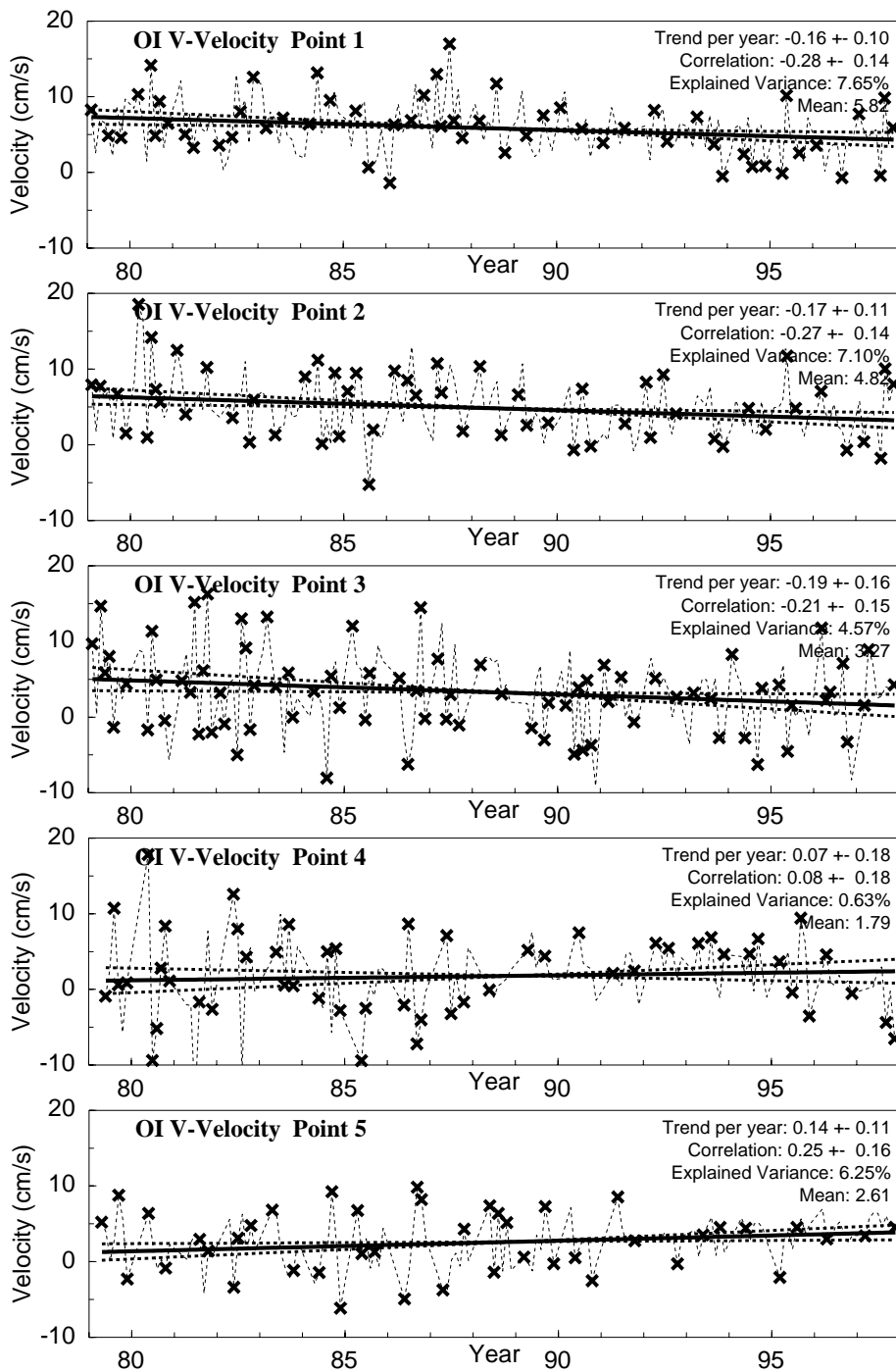
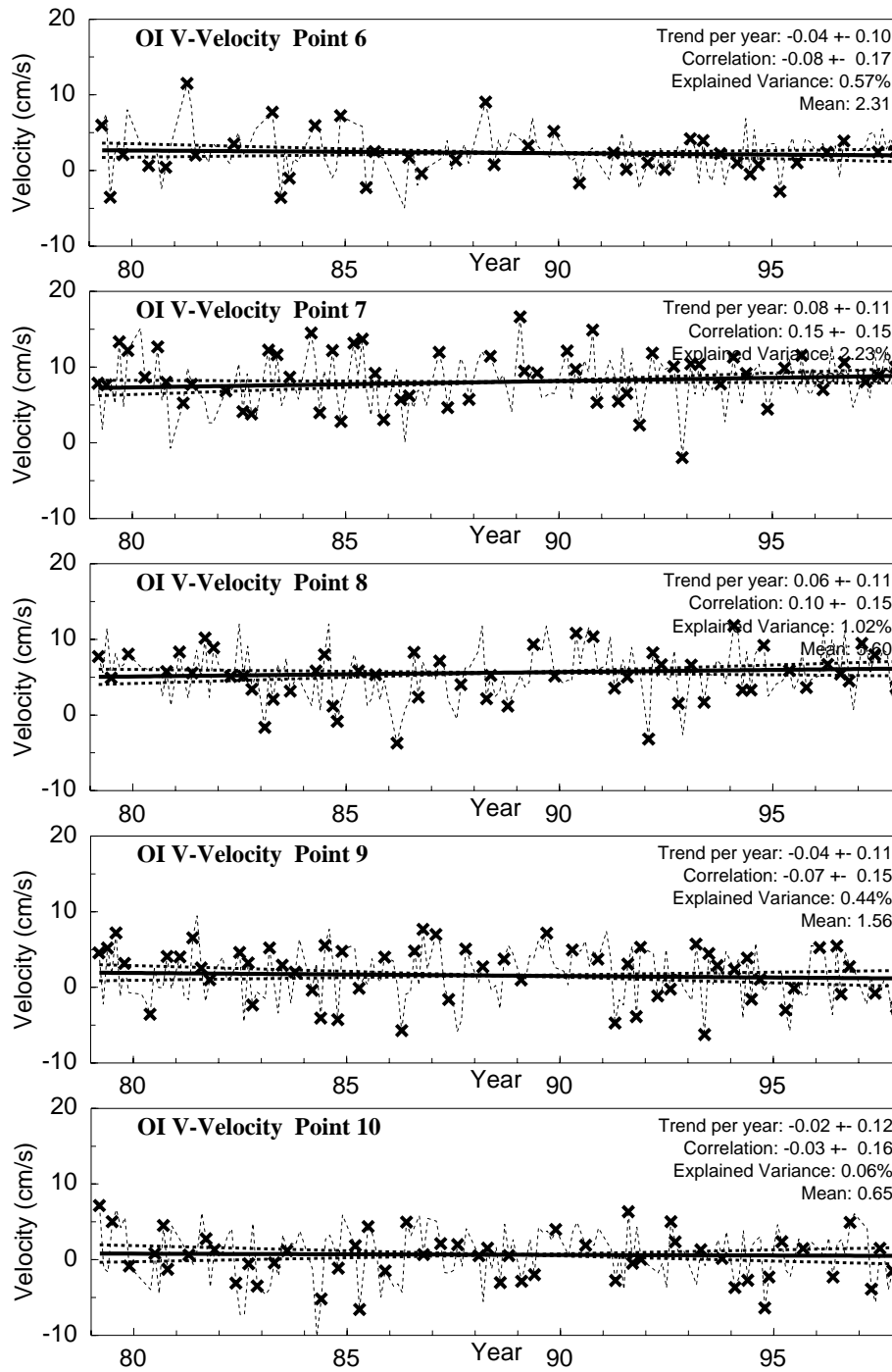


Figure A.6: Monthly mean meridional drift velocity at points 1 - 5. The black line indicates the mean trend with its confidence intervals as dashed lines.



**Figure A.7:** Monthly mean meridional drift velocity at points 6 - 10. The black line indicates the mean trend with its confidence intervals as dashed lines.

## A.5 List of Abbreviations

**AAO** - Antarctic Oscillation  
**ACC** - Antarctic Circumpolar Current  
**ACW** - Antarctic Circumpolar Wave  
**DIV** - Divergence  
**DKP** - Differential Kinematic Parameters  
**DMSP** - Defense Meteorological Satellite Program  
**ENSO** - ElNino-Southern Oscillations  
**EOF** - Empirical Orthogonal Function  
**FY** - First Year Ice  
**GIS** - Geographic Information System  
**GPS** - Global Positioning System  
**IPAB** - International Programme for Antarctic Buoys  
**MIZ** - Marginal Ice Zone  
**MW** - Meridional Wind  
**MWS** - Meridional Wind Stress  
**MY** - Multi Year Ice  
**NCEP** - National Centers for Environmental Prediction  
**OI** - Optimal Interpolation  
**PELICON** - Project for estimation of long-term variability of ice concentration  
**PIXEL** - Picture Element  
**RMS** - Root Mean Square Error  
**SAM** - Southern Annular Mode  
**SAO** - Southern Semiannual Oscillation  
**SAT** - Surface Air Temperature  
**SEALION** - Sea Ice in the Antarctic, linked with Ocean-Atmosphere Forcing  
**SHR** - Shear  
**SIA** - Sea Ice Area  
**SIC** - Sea Ice Concentration  
**SIE** - Sea Ice Extent  
**SIS** - Sea Ice Season  
**SLP** - Sea Level Pressure  
**SMMR** - Scanning Multichannel Microwave Radiometer  
**SOI** - Southern Oscillation Index  
**SSMI** - Special Sensor Microwave/Imager

**SST** - Sea Surface Temperature

**VOR** - Vorticity

**WMO** - World Meteorological Organisation

**ZW** - Zonal Wind

**ZWS** - Zonal Wind Stress



# Lebenslauf

## **Persönliche Daten**

Name: Carolin Schmitt  
Geboren: 25.10.1970 in Malsch/Kreis Karlsruhe

## **Schulbildung und Studium**

1977 - 1981 Grundschule Baden-Oos  
1981 - 1990 Richard-Wagner-Gymnasium Baden-Baden  
1991 - 1993 Grundstudium Feinwerktechnik an der FH Ulm  
1993 - 2000 Studium Meteorologie an der Universität Karlsruhe  
März 2000 Diplom im Fach Meteorologie

## **Berufserfahrung**

Seit 2000 IMK, Institut für Meteorologie und Klimaforschung der  
Universität Karlsruhe/Forschungszentrum Karlsruhe  
2000 - 2001 Orographische Einflüsse auf hochreichende Konvektion  
2001 - 2004 Erstellung eines GIS-basierten Meereis-Drift-Atlas  
2004 - 2005 Anfertigung der Dissertation  
seit April 2006 Wissenschaftliche Angestellte am IMK, Universität  
Karlsruhe

## **Berufsbegleitende Tätigkeiten**

2000 - 2002 Sachbearbeiterin Geodaten, DDS GmbH Karlsruhe  
2004 Wissenschaftliche Mitarbeit am Geodätischen Institut  
der Universität Karlsruhe



# Acknowledgements

This work was performed at the Institut für Meteorologie und Klimaforschung, Universität Karlsruhe. The data preparation was done within the project "Atlas of Antarctic Sea Ice Drift" funded by the Deutsche Forschungsgemeinschaft.

At this place, I would like to thank all the people who supported my work. First of all, I thank my supervisor Prof. Dr. Christoph Kottmeier for his encouragement and support during my whole time at the department. He gave me the opportunity to work on this exciting scientific topic and was sharing his profound knowledge on climate and dynamics in Antarctica and his enthusiasm for the polar regions with me. I thank my co-supervisor Prof. Dr. Sarah Jones for her interest in my work and her helpful suggestions. I also wish to thank Mark Drinkwater from ESA/ESTEC for his encouragement and scientific advice during my stay abroad at ESTEC and the fruitful email discussion on the research conducted, which helped to make it a more complete work. Further, I would like to thank all people of the IMK that are not mentioned by name here for supporting me with scientific, administrative or personal advice. Special thanks goes to my office-mates for the interesting discussions on various topics and the help on programming problems and to Nicole Riemer for the assistance in the translation of this work. This thesis was benefitting from some well-founded datasets, which are gratefully acknowledged here. The optimal interpolated SSMI data have been provided by JPL, Polar Remote Sensing Group, courtesy of Ron Kwok, and Mark Drinkwater respectively. The IPAB buoy archive was received from NSIDC (National Snow and Ice Data Center). Ice concentrations came from the European Project PELICON from G. Heygster and C. Thomas, Institute of Environmental Physics, University of Bremen. NCEP Reanalysis data was provided by the NOAA-CIRES Climate Diagnostics Center, Boulder, Colorado, USA. The use of the Geographic Information System PCI was made possible by MSA Group, Institut für Meteorologie und Klimaforschung, Section Atmospheric Trace Constituents and Remote Sensing, Forschungszentrum Karlsruhe by F. Olesen and H. Fischer.

Eventually, I want to thank my parents, my family and all my friends who contributed to this work by supporting me in their own special ways whenever I needed them.